State-of-Health Estimation of Li-ion Batteries: Cycle Life Test Methods

JENS GROOT

State-of-Health Estimation of Li-ion Batteries: Cycle Life Test Methods

JENS GROOT

State-of-Health Estimation of Li-ion Batteries: Cycle Life Test Methods
JENS GROOT

Division of Electric Power Engineering
Department of Energy and Environment
Chalmers University of Technology
SE-412 96 Göteborg
Sweden
Telephone: +46 (0)31 772 1000

State-of-Health Estimation of Li-ion Batteries: Cycle Life Test Methods
JENS GROOT
Division of Electric Power Engineering
Department of Energy and Environment
CHALMERS UNIVERSITY OF TECHNOLOGY

Abstract

Despite a rapid development, cost, performance and durability of the energy storage system are still a hindrance for a wide commercialisation of heavy-duty hybrid electric vehicles (HEV). The purpose of the work presented in this thesis is to investigate how different load cycle properties affect the cycle life and ageing processes of Li-ion cells developed for use in HEVs.

The cycle life of commercial $LiFePO_4$/graphite Li-ion cells was tested using a range of operating conditions and battery load cycles based on conditions relevant to heavy-duty HEVs. Established methods for cell performance evaluation have been combined with half-cell measurements and analysis methods such as incremental capacity analysis, differential voltage analysis and impedance spectroscopy to characterise the cell ageing in terms of capacity fade, power fade and impedance rise. Furthermore, a simplified cell fade model is used to distinguish between different likely ageing mechanisms.

Loss of cyclable lithium is found to be the main contribution to ageing during the first phase of cycling, followed by an accelerated loss of active anode material towards the end of the battery cycle life. The longest lifetime is observed for cells cycled with low peak currents and a narrow SOC range. In addition, high charge current is found to affect the cycle life profoundly. On the contrary, a moderate temperature increase did not result in a shorter cycle life.

Despite similarities in average current and SOC range, the load cycle properties are found to have a significant effect on the ageing characteristics, indicating that a more detailed evaluation of load cycle properties is needed to enable a cycle life estimation model.

Index Terms: State-of-health, battery model, lithium-ion battery, cycle life test, battery testing, HEV, PHEV, EV, ICA, DVA, impedance spectroscopy

"It is a good morning exercise for a research scientist to discard a pet hypothesis every day before breakfast. It keeps him young."

Konrad Lorenz

Acknowledgements

Preface

In 2008, AB Volvo, Scania CV AB, the Royal Institute of Technology (KTH), Uppsala University (UU) and Chalmers University of Technology started a joint research cluster that aims to understand the ageing mechanisms of a Li-ion battery systems used in heavy-duty HEV powertrains. The cluster is co-funded by the Swedish Energy Agency and the two industrial partners.

The investigation focuses on finding the correlation between operating conditions in a real application and the fundamental ageing processes in the battery cell. Research is made on several levels; from *in situ* measurements on electrode materials and research cells made by KTH and UU to applied tests of commercially available Li-ion cells in laboratory and field applications performed by Volvo and Scania. More specifically Volvo focuses on the development of models for the ageing mechanisms.

This thesis gives insights of how various operating conditions affect the life time of Li-ion batteries used in heavy-duty vehicles. In addition, it presents a number of different characterisation techniques that can be used to evaluate and understand the ageing mechanisms. These results will also be the base for a development of Li-ion battery ageing models for hybrid electric vehicles which is planned for in the continuation of this work.

x

Table of Contents

Glossary

AC	Alternating Current
BOL	Beginning of Life
DC	Direct Current
DVA	Differential Voltage Analysis
EIS	Electrical Impedance Spectroscopy
ESR	Equivalent Series Resistance
EOL	End of Life
EV	Electric Vehicle
HEV	Hybrid Electric Vehicle
ICA	Incremental Capacity Analysis
ICE	Internal Combustion Engine
KTH	The Royal Institute of Technology
PHEV	Plug-in Hybrid Electric Vehicle
RMS	Root-Mean-Square
RPT	Reference Performance Test
SEI	Solid Electrolyte Interface
SOC	State of Charge
SOH	State of Health
UU	Uppsala University

Chapter 1   Introduction

Over the past ten years, hybrid electric vehicles (HEV) have been successfully introduced to the passenger car market. Following numerous demonstrator projects, several manufacturers of heavy-duty vehicles are currently investigating and/or introducing the HEV technology to heavy-duty vehicles. In the mean-time, plug-in HEVs (PHEV) such as the GM Chevrolet Volt™ or the Toyota Prius Plug-in™ are being introduced to the passenger car market. This drivetrain topology might also be suitable for certain heavy-duty applications, at least from a technical point of view. Although the HEV and PHEV topologies still rely on the usage of an internal combustion engine (ICE) the possible reduction of fuel consumption and emissions is significant and may represent a leap in transportation efficiency and sustainability.

There are several possible advantages with the HEV drivetrain compared to a conventional driveline based solely on an internal combustion engine. First and foremost, the HEV drivetrain recuperates brake energy which can be used to enhance vehicle acceleration, powering of auxiliary loads or to optimise the operation point of the ICE. In addition, it may also reduce emissions and, in the case of PHEV, provide limited all-electric drive and silent operation.

Even though incentives and other factors related to municipality and state legislation in many countries and cities actively drives the development towards vehicles with lower emissions and fuel consumptions, the feasibility of heavy-duty HEVs is still strongly dependant on the performance and additional cost of the electric driveline components [1]. Among these comparably new vehicle components, the energy storage, usually a battery, is the single most expensive component. Hence, the performance, cost and durability of the energy storage are critical for the overall feasibility of a heavy-duty HEV/PHEV.

There is an intense and rapid development of batteries for use in HEVs and PHEVs. Not only the electrical performance in terms of energy and power density is improved, but also life, safety and production cost. Despite this rapid development the cost of batteries is still high compared to other drivetrain components. Currently lithium-ion (Li-ion) batteries are the most attractive chemistry, first and foremost due to strict requirements in power and energy [2].

There exist a large number of different types of Li-ion batteries, ranging from low-cost mass-produced cells used in portable consumer electronics to advanced designs tailored to meet specific requirements of aerospace and military applications. As of 2011, there is no high volume production of Li-ion cells for automotive applications. Although several new manufacturers are targeting this market the volumes are still small compared to the production of cells for consumer electronics. Moreover, there are a large number of different electrochemical designs of Li-ion batteries, each with advantages and disadvantages related to cost, performance, cycle life and safety. Considering safety and production cost one of the most capable cell type is the $LiFePO_4$ // graphite cell, introduced to market fairly recently [3], [4]. However, the lifetime of Li-ion batteries for HEVs is still uncertain, leading to a hesitation at both the manufacturer and potential market end. To large extent this is due to the lack of accurate models for prediction of the highly nonlinear battery ageing mechanisms in different vehicle applications. Such models would enable an optimization of battery usage, which in turn would lower the total battery cost and ensure a stable fuel economy throughout the vehicle service life.

Furthermore, the design process and the real-time control of the HEV drivetrain, including the energy storage, rely on accurate estimations on battery wear as a function of operating conditions and usage. With the focus set at vehicle durability, this state-of-health (SOH) estimation has become as important to the HEV as the estimation of state-of-charge (SOC) is for electric vehicles (EV).

Currently, the SOH estimation models for industrial battery systems are often based on field or laboratory measurements. Despite extensive testing under a wide range of conditions these measurements may still lack relevance to an HEV application due to the non-linear nature of battery degradation. In other words, the results obtained after years of cycling a battery cell to a specific drive cycle is unlikely to be directly

applicable to other drive patterns/applications. This is a profound difference between the HEV market and the consumer electronics market, where the battery load cycles (discharge / charge pattern) are similar for the majority of applications (laptops, cellular phones, digital cameras etc.) whereas each automotive application and market segment has different requirements and operating conditions. As an example, batteries in HEV passenger cars and trucks are used in a profoundly different way. Additionally, the use of trucks and buses are diverse; the same type of vehicle might be used for both city traffic and regional traffic and in different climates. Also, requirements on performance and durability differ between different markets. Consequently, battery requirements for heavy-duty HEVs cover a wide range in terms of cycle life, cost, performance and durability. In contrast, commonality between vehicles is highly desirable, especially when introducing new technology associated with high development cost. Hence, a reliable prediction of battery life as a function of vehicle usage reduces the risk when investing in this new technology.

1.1 Purpose

The purpose of the work presented in this thesis is to investigate how different load cycle properties affect the cycle life and ageing processes of Li-ion cells developed for use in HEVs. In particular, Li-ion cells using graphite anodes and $LiFePO_4$ cathodes are to be studied. Furthermore, a target is to perform extensive laboratory testing of commercial Li-ion cells to develop and evaluate test methods for cycle life tests. The cell ageing analysis is combined with results from field testing of cells performed by Scania CV AB and research tests performed by KTH and UU. Finally, an objective is to initiate the modelling of SOH which are to be developed in the continuing phase of this investigation.

1.2 Outline

A limited literature survey concerning background information on Li-ion batteries, ageing mechanisms and test methods is summarised in Chapter 2. This background information is followed by a detailed description of the test procedure, selected load cycles and the experimental set-up in Chapter 3, Chapter 4 and Chapter 5, respectively. An overview of the cycle life test results is presented in Chapter 6, followed by an analysis of the ageing mechanisms in Chapter 7 and concluding remarks in Chapter 8.

Chapter 2   Li-ion Batteries & Cycle Life Testing

Li-ion batteries have been available as commercial products since the early 1990-ies. Today, there exist numerous different types of Li-ion batteries based on different anode materials, cathode materials, electrolytes and separators [3],[4]. A very simplified view of the most commonly used cell materials is presented in Figure 2.1.
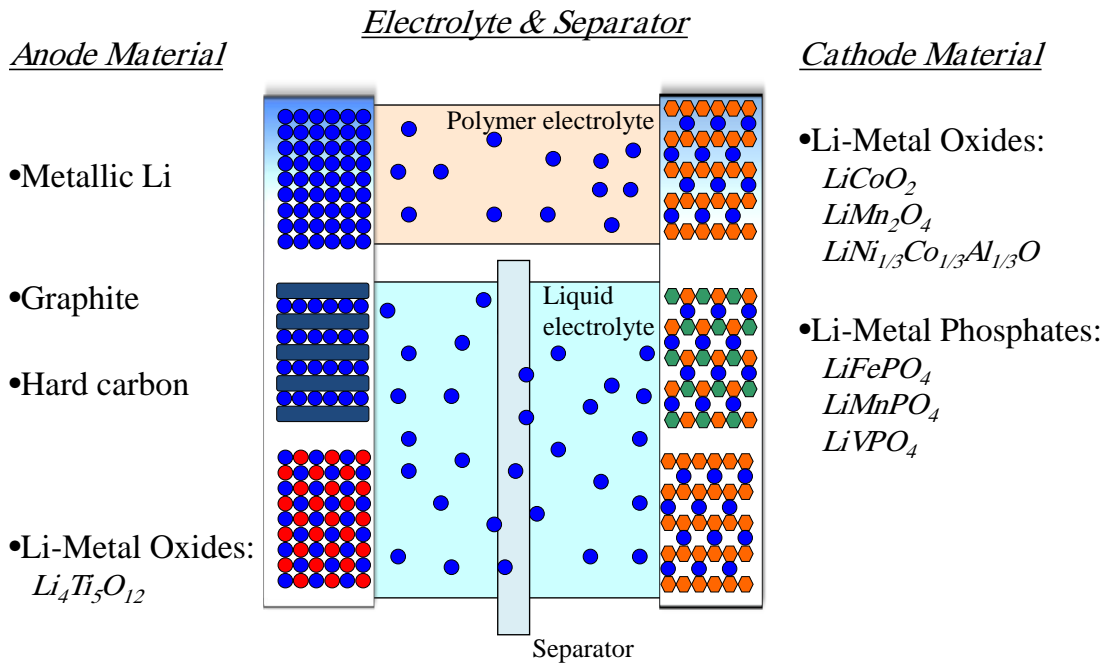
Figure 2.1   Overview of the most commonly commercialised Li-ion battery concepts.

The first commercial cells were based on a metallic lithium anode and a lithium-metal insertion oxide as cathode. Despite superior energy density compared to other commercial rechargeable batteries this cell type faced severe issues with safety and reliability due to un-even lithium plating on the anode if re-charging leading to so called dendrite growth, in turn leading to internal short-circuit and pre-mature failure. The commercialisation of Li-ion cells was enabled by the use of a graphite intercalation electrode as anode, greatly increasing safety, life and reliability. This anode type is still dominating the market although a number of other anode materials such as hard-carbon, lithium-titanate and silicon recently have been introduced. Likewise to the anode development, there has been a rapid development of all the other cell materials; numerous metal oxides, metal phosphates [5], blends and doped materials have successfully been used as cathode. In addition, safety and reliability have been greatly enhanced with new electrolytes (liquid or polymer type), binders, additives and

separators. Nevertheless, as sub-components of the cell are improved overall, each component faces increasing challenges in mitigating the intrinsic disadvantages.

All commercially available cells available today use a similar cell design as schematically presented in Figure 2.2 (drawing not to scale).
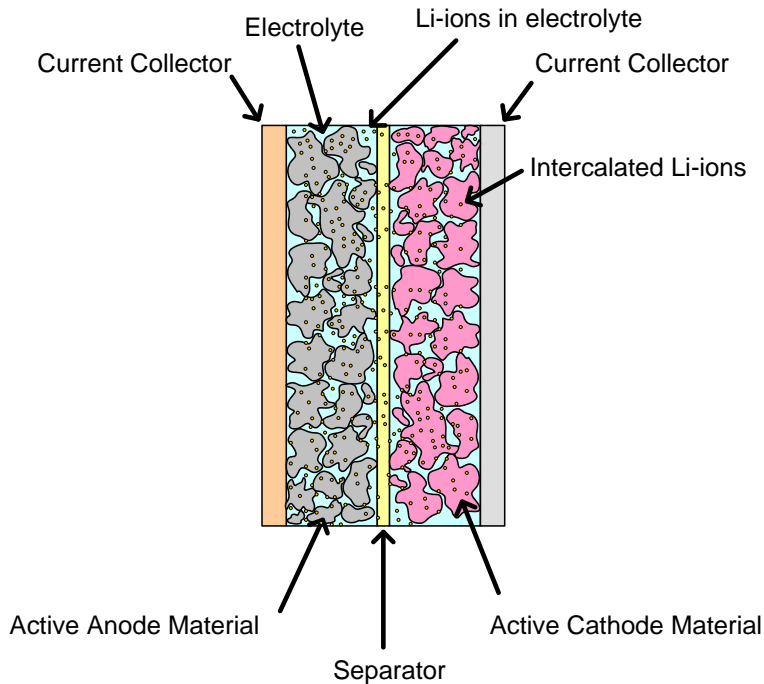
Figure 2.2   Schematic illustration of a Li-ion battery.

The cell design mainly comprises:

- An anode and a cathode electrode consisting of active material in form of a powder mixed with a binders and additives, attached to a metal current collector, soaked with lithium conducting electrolyte
- A thin separator soaked in electrolyte or Li-conduction polymer
- A complex mix of additives to the electrolyte is used to increase conductivity, reduce parasitic reactions and to increase cycle life and safety.

The porosity of the electrodes is vital to achieve a large active surface area, thus providing a high rate and high specific energy. On the other hand, a high porosity may limit the mass transport rate of Li-ions in the electrolyte. Hence, the design is always a compromise between different properties.

In a real cell each particle in the active region of the electrodes is glued together with a binder to the current collector ensuring a good electrical conductivity between active material and cell external terminals. The separator should block direct electron transfer between electrodes but still provide a good path for Li-ions while maintaining mechanical robustness and temperature stability.

The capacity and energy of a Li-ion cell is determined by the choice of active material, and the amount of passive material. On the other hand, a comparably high ratio of passive material such as binder, electrolyte solvent and current collectors is needed to achieve high material transport and low losses that is vital for high-power applications. Moreover, to maintain long cycle life and low price additional compromises with performance is needed. In addition, the power capability of a battery is a function of a number of factors: choice of cell materials, electrolyte, mechanical design, electrolyte and the amount of passive material such as current collectors and terminals. Consequently, the battery design is always a compromise between energy, power, cost and service life.

The investigation covered by this thesis focuses solely on Li-ion cells based on a graphite anode and a $LiFePO_4$ cathode.

The battery capacity is usually measured in Ampere-hours (Ah) and its energy in Watt-hour (Wh). An alternative to measuring current in Ampere is C-rate which is the current normalized with the battery capacity. That is, 1 C-rate (C/1) is the current needed to charge/discharge the battery in one hour, 10 C-rate (C/0.1) will charge/discharge the battery in 0.1 hour and 0.25 C-rate (C/4) will discharge the battery in 4 hours.

2.1 Reference Electrodes & Half-cells

Although all electrochemical cells by definition have at least two electrodes, a third reference electrode may be used as a stable potential reference that is unaffected by the main electrochemical reactions. This is often done during investigations of new battery materials in order to measure individual electrode potentials during tests, or to exclude voltage drop in the electrolyte. However, due to practical reasons it might be difficult to design a battery cell with a reference electrode. Also, the placement of the reference

electrode relative to the electrode surface will determine the outcome; essentially what properties that can be measured with sufficient accuracy.

An alternative to the use of reference electrode may be to test one electrode at a time against a large counter electrode with known properties. For Li-ion batteries this is usually done by combining an anode or cathode material with a foil of metallic lithium as counter electrode as illustrated in Figure 2.3 (drawing not to scale).
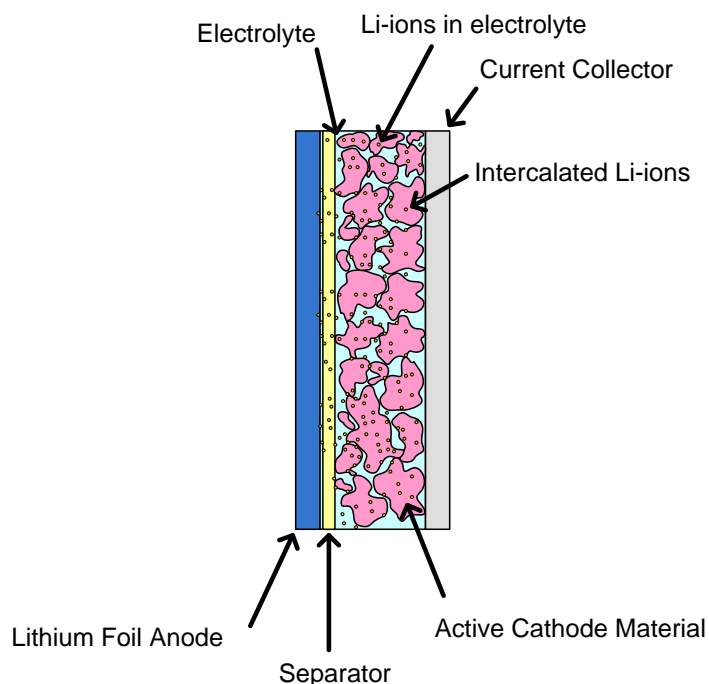
Figure 2.3   Schematic illustration of a half-cell with metallic lithium as anode.

Although this setup is not suitable for long cycle life tests because of the risk for dendrite formation, it represents a comparably easy and reliable method to study the properties of individual electrodes since the kinetics and reaction rate of the Li/Li^+ reaction occurring at the lithium counter electrode is known.

2.2 Characterisation of Li-ion battery lifetime

All rechargeable batteries show a decreasing performance of usage and/or time. That is, the capacity, measured as the ability to repeatedly store and release electric charge, decreases. Likewise, the battery's ability to be charged or recharged at high electric power is reduced over time and the number of charge/discharge cycles. This reduction in battery performance is usually referred to as *battery ageing*. For Li-ion batteries, it has been shown the performance is affected by both storage time and usage, often

categorized as *calendar ageing [years]* and *cycle life [Maximum No. of cycles or maximum operating time for a specific set of operating conditions.]*. The calendar life is often tested by storing cells in controlled temperature and at a fixed charge level. At certain time intervals the cell performance is measured and the battery calendar life expressed as the time the battery can be stored until the performance drops below a pre-defined level.

The ageing of the battery is usually quantified as capacity and/or power or as a function of number of charge/discharge cycles (defined separately), the total capacity throughput (total amount of electric charge being cycled) or time (duration of test and/or total time during charge / discharge). Generally, applications relying on the battery as a primary energy source, such as electric vehicles and portable consumer electronics, are more sensitive to capacity fade than power fade. Thus, the capacity fade is usually used to quantify the aging for these applications. In contrast, HEVs that use the battery as an energy buffer for short high-power charge/discharge and rarely use the full energy storage capability of the battery are more sensitive to power fade than capacity fade. Consequently, the power fade rate might be a better measure of ageing than capacity fade for this type of application.

The battery cycle life can be tested by two main methods:
- Simple and/or standardized cycles, often full discharge-charge profiles, used to evaluate temperature dependency and to compare different cells / cell designs.
- Evaluation of cycle life for specific applications. This includes field tests and laboratory tests with load cycles matching the intended industrial applications.

Although the ageing mechanisms are similar, these two test methods might not provide comparable results since most ageing processes within the cell are highly non-linear. That is, small changes in the load cycle or operating conditions may cause one or a few ageing processes to dominate, effectively limiting the total cycle life. Nevertheless, analysis of the degraded cells serves as a very important input to further cell development and optimization of the target application.

Generally the overall process for characterising battery life time consists of three steps:

1. Measurement of initial performance at beginning-of-life (BOL)
2. Cycle life test or calendar life test with reference performance tests (RPT) carried out on regular basis
3. Measurement of cell performance and cell degradation analysis at end-of-life (EOL).

2.3 Ageing Mechanisms of Li-ion batteries – a Literature Review

The ageing of Li-ion batteries is complex and determined by the operating conditions [6]-[9]. In some cases it is possible to assign the observed capacity and power fade to a certain ageing process [10], [11]. This is typically the case when the battery is used under extreme conditions such as elevated temperatures [6], high rate charging [12], [13], or high SOC levels. However, in most applications where the conditions are controlled to optimize the total life the observed performance fade is the result of several process of which some are coupled and other can be regarded as independent [9], [14].

The development of Li-ion batteries has been rapid since the introduction in the mid-nineties. Hence, this survey is limited to the publications from 1999-2011 to focus at the most recent development and cell designs used today. The following section summarizes the main ageing mechanisms found in published papers / journals until 2011.

Being a complex combination of a large number of different processes, electrochemical, mechanical and related to cell design, it is beyond the scope of this study to give a comprehensive overview of all possible ageing mechanism. This section should be regarded as a brief overview of the processes presented in selected publications particularly useful for the work covered by this thesis.

Generally, the capacity fade of Li-ion cells is due to a combination of three main processes [10]:

*   Loss of Li / loss of balance between electrodes
*   Loss of electrode area
*   Loss of electrode material / conductivity

The loss of cyclable lithium is in turn due to side reactions such as corrosion, Li-plating and solid electrolyte interface (SEI) formation at the graphite anode [15]-[17].

Since the graphite anode is the most widely used in present Li-ion batteries this study has set a particular interest in this electrode material. In contrast the ageing properties of the cathode electrodes must be discussed from case to case depending on the particular cell design.

In addition, ageing mechanisms that reduce capacity may also lead to changes in surface properties such as porosity and tortuosity [11]. In this reasoning it is important to state that the available capacity might be reduced further by an increased voltage drop due to a rise in cell impedance that prevents the battery from being fully discharged (or charged) at a specific current [18], [19]. In most cases the capacity fade and impedance rise are clearly correlated which will be investigated in the following sections. The ageing processes are further complicated by the fact that many of the studied mechanisms are coupled to a rise in cell impedance, leading first and foremost to a notable reduction in maximum cell power.

An overview of the most significant mechanisms for power fade / impedance rise is summarized by the following bullets and Figure 2.4:

- Surface film formation of both electrodes with low conductivity [16], [20]-[22].
- Loss of electrode area and electrode material leading to a higher local current density [23].
- Lower diffusivity of lithium ions into active electrode particles and slower kinetics (increased charge transfer resistance) due to surface films
- Reduced conductivity between particles due to both surface films and degradation of binders, possibly in combination with a binder-Li reaction [23].
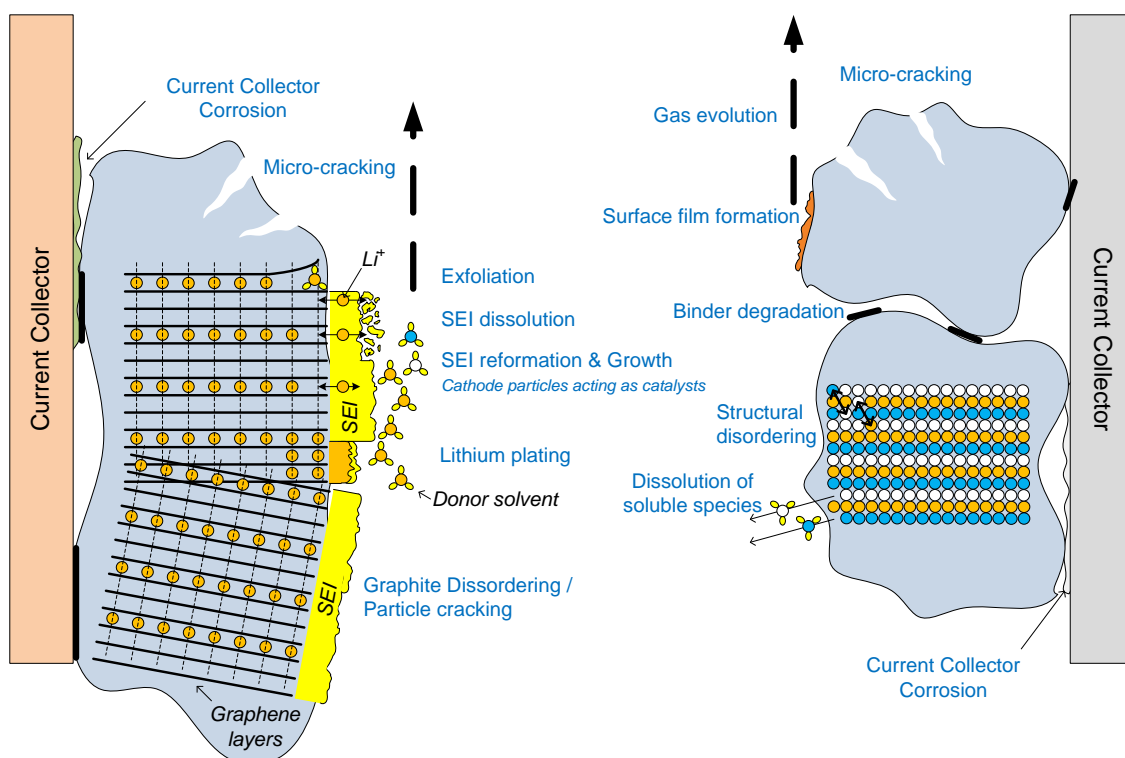
Figure 2.4   Main ageing mechanisms occurring at Li-ion battery electrodes (blue text).

A summary of the main electrode ageing mechanisms, mainly described by Vetter *et al.* [9], is presented in Figure 2.4. Here, ageing mechanisms can be categorized into mechanical changes (particle cracking, gas formation), surface film formation (SEI, lithium plating), bulk material changes (structural disordering [24]-[27]), and parasitic reactions (binder degradation, localized corrosion). These ageing mechanisms are described further in the following sections.

The ageing mechanisms at the electrodes are directly dependant on the choice of the electrode material. However, there are several similarities between different electrode materials.

According to several published papers [8], [9], [14], the bulk material properties of anode and cathode do not change greatly over the service life of a Li-ion battery, but the surface undergoes a significant change in mechanical structure and electrochemical properties.

2.3.1 SEI formation and reformation

Although being a widely used anode material for Li-ion batteries, graphite is not electrochemically stable when used together with most common electrolytes. As the cell is charged for the first time, lithium reacts directly with the graphite to form a thin solid surface film (SEI) mainly consisting of Li_2CO_3 [28], alkyl-carbonates, and polymers. Thereby, this process leads to an initial irreversible capacity loss. However, with a close to completely covering film, further reaction (and consumption of lithium) is prohibited. Since the SEI is very thin its conductivity for lithium ions remains sufficient to enable an efficient intercalation of lithium into the graphite particles. On the other hand, a too thin SEI allows electrons to tunnel through the film, in turn enabling other side reactions and further SEI formation. Consequently, the SEI continues to grow until a steady-state thickness is established which usually is reached after the few first cycles (commonly denoted as the formation of the cell). Further formation of SEI has a significant effect on the impedance of the cell. That is, a thin SEI is needed to limit the graphite direct reaction with the electrolyte, but thick films are detrimental.

It has been shown that the SEI formed at low to medium temperature partly dissolves at high temperatures, exposing the graphite surface to further reaction with electrolyte and subsequent consumption of lithium.

In addition, the volume change occurring in the graphite particles upon intercalation / de-intercalation of lithium might lead to micro cracks in the surface film, which also exposes the graphite to further SEI formation. This is especially the case during deep discharges since the main volume change occurs at SOC up to approximately 20%.

The SEI formation is according to Belt *et al.* [29] directly linked to the lithium corrosion discussed in section 2.3.4 which produces both soluble and insoluble (SEI) products.

A similar surface film growth may in some cases be observed at the cathode as well [30], but as this process is less pronounced and directly dependant on the choice of cathode material this survey includes no overview of this ageing mechanism.

2.3.2 Contaminations

Traces of contaminations in the electrolyte stemming from either the manufacturing process or from dissolved species from the cathode may also lead to SEI dissolving and subsequent reformation at the expense of available lithium. Other possible processes involve either irreversible loss of lithium or surface film formation. Especially traces of water may accelerate ageing [31].

2.3.3 Lithium plating

The intercalation / de-intercalation of lithium into graphite occurs at an electrochemical potential close to that of Li/Li^+ and is one of the main advantages of using graphite as anode material. On the other hand, if the surface potential of the graphite is forced sufficiently low potentials lithium ions may form metallic lithium at the surface instead of the intended intercalation. This process is not fully reversible as dissolution of Li may form other compounds rather than lithium ions. Furthermore, a complete dissolution of Li requires an electronic transfer through the SEI which, as highlighted in section 2.3.1, is ineffective. Typically lithium plating is most pronounced at low temperatures and / or high charge currents. In extreme cases a significant amount of the lithium can be irreversibly consumed in just a few cycles.

2.3.4 Corrosion

Lithium corrosion is a wide definition of side reactions where lithium reacts with electrolyte and / or electrodes to form soluble and insoluble products. Both reaction categories primarily lead to irreversible loss of lithium. The soluble species mainly participates in self-discharge processes and the insoluble species contributes to the SEI formation and other relatively stable products [32].

The current collectors may also be susceptible to corrosion [33], especially if exposed to potential close to or exceeding their electrochemical stability window determined by the overall cell design and choice of materials.

2.3.5 Gassing

Some parasitic reactions in the cell may lead to the formation of gaseous products, mainly CO_2. The gas evolution introduces mechanical stress to the electrodes which in turn increases the rate of SEI reformation and, if severe, leads to a rupture of the cell enclosure. In addition, it may reduce the active area of the porous electrode structure if gas is trapped in pores. Furthermore some investigations [8] indicate that the presence carbonates formed in the SEI increases the CO_2 evolution.

2.3.6 Migration of reaction products

Side reactions occurring at anode and cathode may in some cases result in soluble species that can migrate through the separator [6], [9]. The knowledge of the probable impact of this process is not well established but it is indicated that they can increase the formation rate of surface films at both electrodes.

2.4 Battery Life Test Methods

2.4.1 Accelerated Testing

Accelerated test methods are interesting for use by both cell manufacturers and application developers. The combination of a narrow temperature range and non-linear ageing reduces the possibilities to find an efficient and reliable method for significantly reducing the time to test battery lifetime.

The studied publications mainly suggests the use of elevated temperatures (<+55 C°) [34]-[36] in combination with medium temperatures to create models for the ageing related to temperature within the nominal range of cell temperature. A similar approach may be used for SOC levels [37], [38] and voltage [39], although the general feasibility of this method depends on the choice of application and cell chemistry. To some extent the ageing might be reduced by the use of additives to the electrolyte [40]. Generally, the formation of surface films on electrodes accelerates significantly at elevated temperatures [41].

2.4.2 Calendar Ageing

Some of the ageing mechanisms occur even if the battery is not used, *i.e.* held at a constant charge level or stored. This is usually tested by charging cells to a predefined SOC level, usually 50-100%, and then storing the cell at constant temperature [36], [42]-[44]. The charge level is often maintained by a constant voltage float charging and the test may be accelerated by increasing the temperature [32].

It has been reported that the effect of calendar ageing is cross-dependant on cycling [45]. In other words, the calendar ageing rate may be different if the cell was cycled prior to the calendar test or in between calendar tests.

Heavy-duty HEVs or PHEVs are often in service for the majority of their service life in contrast to passenger cars that are parked during the majority of their service life. Hence, the study covered by this thesis focuses mainly on cycle life testing and cycle life ageing.

2.4.3 Standardised Cycles

Simple and/or standardized cycles, often full discharge-charge profiles, used to evaluate temperature dependency and to compare different cells / cell designs. There exist a number of established test procedures including those from EUCAR [46], FreedomCar [47] and IEC [48]. The most commonly used cycle life test is probably a 1 C-rate charge and discharge profile using the full battery capacity (0-100% SOC) performed at room temperature. Also, some alterations of this combining a higher discharge current with a lower charge current or testing at a few different temperatures are commonly published by cell manufacturers. The main disadvantage with using standardised cycles is that it is very difficult to use the test results to evaluate the cycle life in an application not using constant current or a wide current range. Nevertheless, the test data from these simple cycles may still provide data for screening or comparing the general performance of different cells/suppliers.

During the recent years there has been a trend where it is more common to use more complex cycles as proposed by EUCAR, FreedomCar and IEC for cycle life tests. It is however still not feasible to make an accurate estimate of the cycle life in more complex cycles relying solely on this kind of measurements.

2.4.4 Cycle Life Evaluation

In contrast to the simplified cycles or calendar life tests, cycle life evaluation carried out for a specific application is usually defined in very close cooperation with the design of the target application. That is, to evaluate the durability of a battery for an HEV a logged load profile is used to repeat the exact usage pattern for that application. Naturally, this provides a very reliable estimation of cycle life as long as the application requirements do not change; a minor change in the SOC range, temperature or load profile dynamics may yield a significant reduction in cycle life. Some applications, like portable consumer electronics, satellites or power tools, have a very predictive usage pattern or a short designed life time and can thus rely on cycle life tests using a narrow range of test conditions.

2.5 Ageing Models

2.5.1 State-of-Health Modelling

A majority of the studied publications present empirical models, often based on experimental data [49] from calendar life tests and cycle life tests with relatively simple load cycles. Some models are based on statistical or mathematical methods [50]-[53], other rely on models more closely built on electrochemical relations [54], There are also semi-empirical models that are designed to model specific characteristics of the cell like the impedance [55], [56], and models that uses a detailed empirical cell models as the base [57], [58]. These empirical models may be especially feasible for use in HEV simulations and drivetrain design.

The fundamental challenge in this field is to obtain a model that is both accurate and without significant computational efforts or the absolute dependence on electrochemical parameters that must be supplied by the cell manufacturer. However, several results indicate that the empirical models can be used provided that their range of accuracy is investigated in detail. For example, calendar ageing models developed for a range of temperatures may successfully be used for prediction of SOH between the experimental data range, although the relations between temperature and ageing is highly nonlinear. Specific ageing processes such as the SEI growth under certain conditions can be modelled by relatively simple relations although the complete ageing model still is very complex [54], [59], [60]. Another approach for modelling cells and cell degradation is

based on complex numerical 1D-models taking mass transport and reaction kinetics into account [61]-[63]. Also, simpler models may be improved if fundamental models of the cell surface structure are enhanced [64]. Often the ageing mechanisms on the cathode and anode are dependent and must therefore be modelled as a coupled reaction [65]. Despite the advantages of using a detailed model based on electrochemical reactions and transport processes, this category of ageing model is less suitable for multimodal simulation with complex load cycles due to their requirement on ling computational time.

Chapter 3   Cycle Life Test Procedure

HEVs and PHEVs may be one of the most challenging applications for battery cycle life predictions since they have an extremely wide range usage patterns and strict requirement of long cycle life. This is one of the key motives for the present work. In order to evaluate and quantify battery ageing for this type of applications a customised test procedure (Figure 3.1) was developed to test battery cell cycle life under relevant operating conditions.
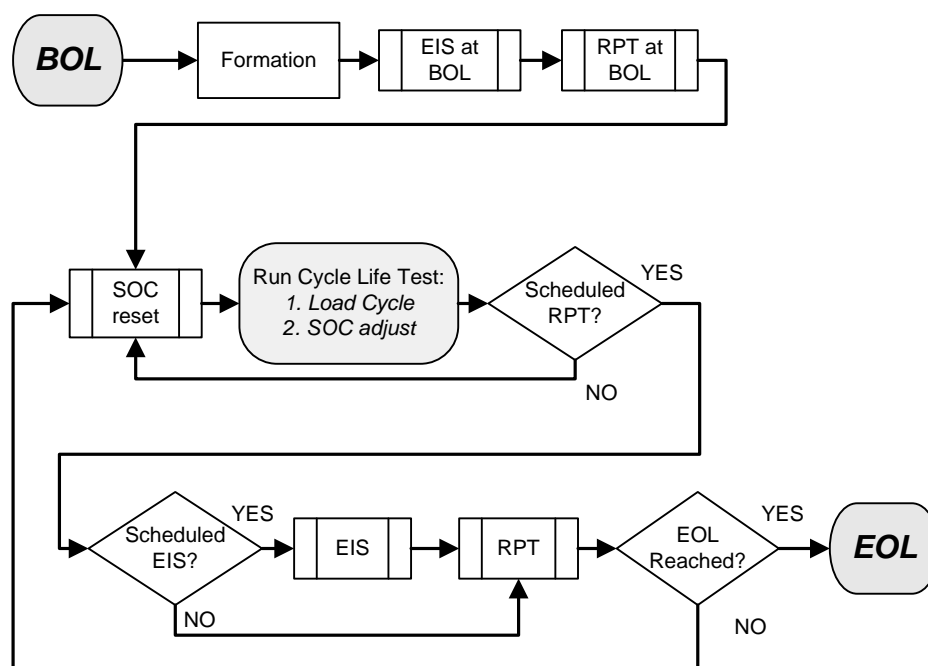
Figure 3.1   Overview of test procedure for cycle life evaluation.

The test procedure illustrated in Figure 3.1 starts at BOL with a formation test consisting of a few complete charge-discharge cycles to ensure that the cells show stable capacity. This short test is then followed by a measurement of the electrochemical impedance spectrum (EIS) and an initial RPT described in section 3.2 and 3.1 respectively. Following this initial characterisation the cell is charged / discharged to its target SOC and cycled with a specific load cycle until a predefined number of cycles have been completed. Then, a new EIS and/or RPT is/are performed before the cycle life test continues.

This process repeats until the cell performance is found to be less than the EOL criteria:

- >20% loss of 1 C-rate capacity
- >30% loss of power

Although EOL is defined by any of these two conditions the cycle life test has continued in some cases to highlight interesting ageing behaviour.

Firstly, this section describes the regular RPTs and EIS measurements. Secondly, the additional sub-procedure for maintaining a specific average SOC range is described. Lastly, the method for controlling the cell temperature during each cycle life test is described.

3.1 Reference Performance Tests

Even though the absolute life time of a cell cycled at different load cycles is of great interest; it can be argued that the evolution of capacity, impedance and other cell properties over the battery life provides profoundly more important information. Generally, a RPT is performed regularly during a life test of a cell. Likewise to the SOC adjustment described in section 3.3, the actual design of such test can have an effect on the ageing it is designed to measure. That is, repeated deep discharge and full charge at different current rates and multiple test pulses to determine the maximum power can degrade the battery when conducted numerous times over a cycle life test. Consequently, the design of a RPT is a compromise between quality of measured parameters and the potential additional ageing it yields. Furthermore, according to previous investigations [66] the design of a RPT may have a profound impact on the measured parameters and their relevance to actual performance in a real HEV application.

A customised RPT was developed within the research cluster between KTH, UU, Scania AB, AB Volvo and Chalmers. This procedure consists of 6 main steps, see Table 1 and Figure 3.2, performed at room temperature (+23 °C).

Table 1   Reference performance test procedure performed at +23 °C.

Step	Description	Extracted parameters
1	Discharge to 0% SOC	Residual capacity control of SOC-adjustment procedure
2	Charge and discharge at 1 C-rate	Voltage profile and standard 1C capacity
3	Charge and discharge at C/4 C-rate	Voltage profile and capacity at low current rate. Used for incremental capacity analysis and anode capacity estimation
4	Charge power at 10C-rate	Dynamic response to high current rate, DC impedance at charge
5	Discharge power at 10C-rate	Dynamic response to high current rate, DC impedance at discharge
6	SOC reset procedure	Readjustment to target SOC, preparation for continued cycle life test

The current used for the charge and discharge power test has been 10 C-rate respectively rather than the maximum specified cell current (see 5.1), and at a limited SOC range in order to reduce possible ageing effects.
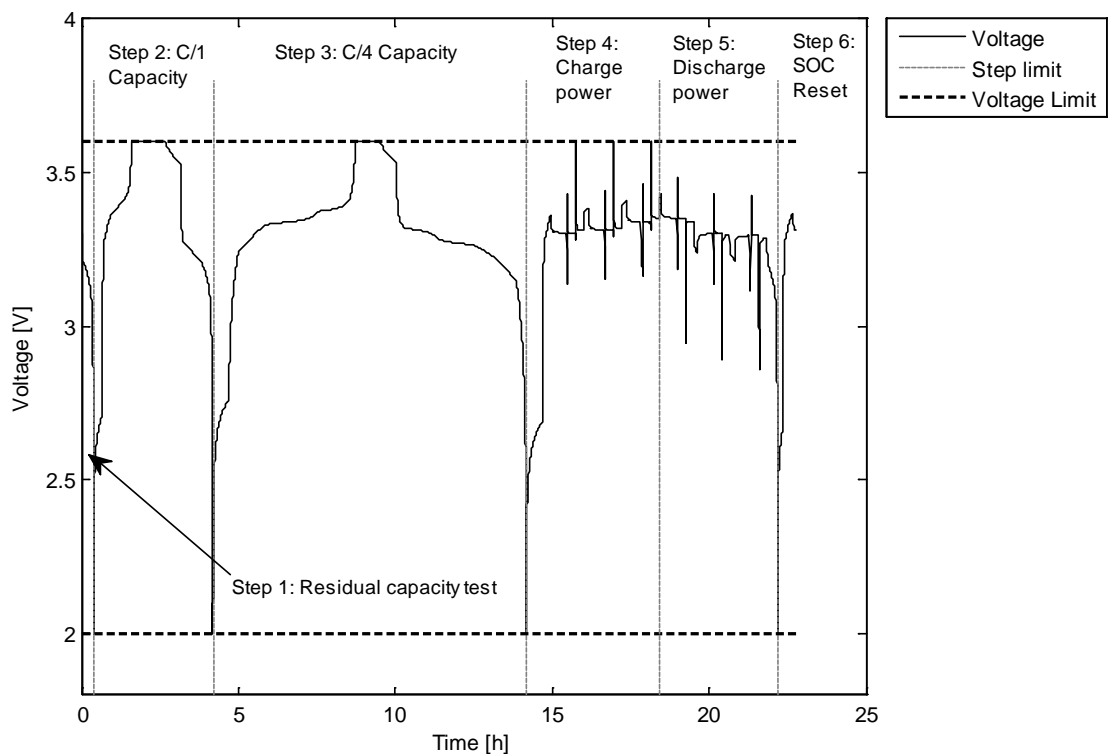

Figure 3.2   Overview of reference performance test procedure.

Each power pulse is 18 s in duration and followed by a 30 min rest period too allow for accurate DC impedance calculations and temperature equalization. Charge power tests

are performed at 30, 50 and 70% SOC and discharge tests at 80, 60 and 40% SOC. Here, the SOC is related to the nominal capacity, not the measured capacity in step 2 or 3. Consequently, the actual SOC relative to available cell capacity will change during the cycle life test. This is, obviously, not the ideal case. However, since the anode and cathode are likely to be cycled at a different SOC range relative to their respective Li-content, it is barely possible to define SOC in a way that will not change with respect to anode, cathode or cell during a long cycle life test. In addition, re-defining the nominal capacity for each test would require significant manual work.

Three values of DC impedance are calculated (see section 0 below): ohmic resistance, 10 s impedance and 600 s impedance.

A combined charge-discharge pulse (section 3.1.2) follows each power pulse and is used to determine the dynamic response of the cell as well as energy efficiency during dynamic pulses at medium power level.

In total, this test requires *ca* 24 h and results in two complete 100% ΔSOC cycles, one partial cycle at *ca* 40% ΔSOC, and one partial cycle at 80% ΔSOC.

3.1.1 Calculation of Power and DC impedance

Each pulse in the power determination consists of a constant current / constant voltage (CC/CV) charge/discharge step of 18s. The test current is set to allow the cell to reach its upper voltage limit during charge pulses. In this way, higher cell impedance will lead to reduced power for both charge and discharge steps. An example is shown in Figure 3.3 where a constant current of 10 C-rate is applied between t_2 and t_3 followed by a constant voltage charge between t_3 and t_4 and a rest period.
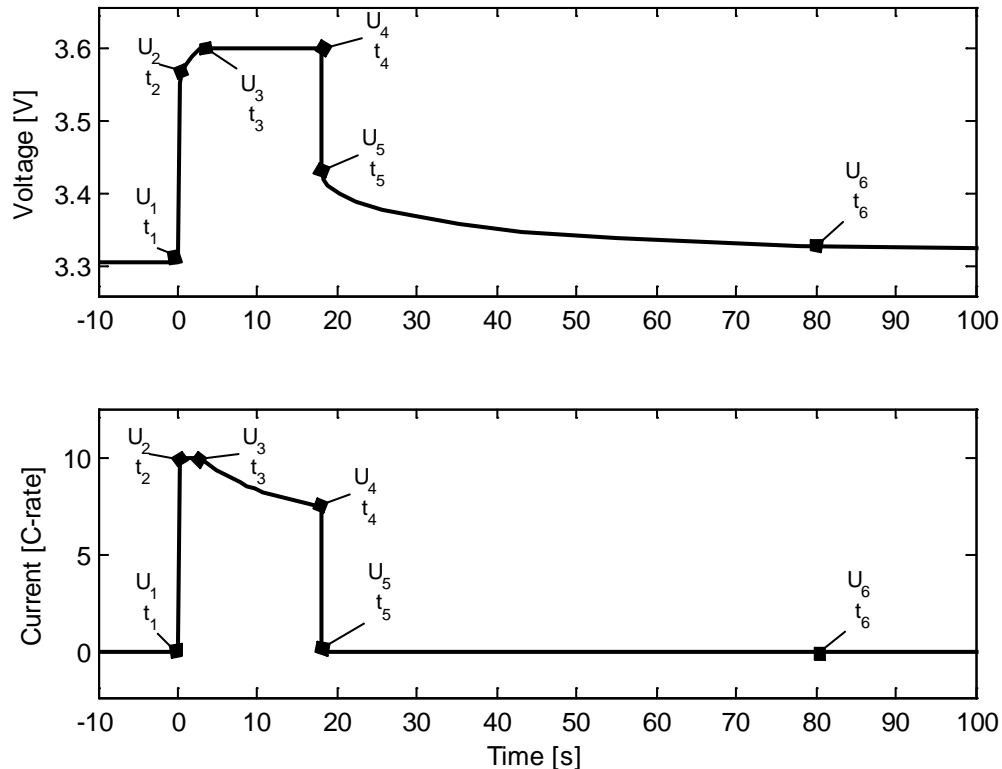
Figure 3.3   Voltage profile for a LiFePO$_4$ battery during a charge power test pulse (shortened rest period t_4 to t_5 in this example).

The maximum discharge and charge power are tested at several SOC levels of the battery. This internal state of the battery is directly related to the reference discharge capacity measured during the formation of the battery and calculated from the C/4 capacity test in step 3 in d at room temperature (+23 °C).
Table 1.

Using the reference capacity, the SOC can be calculated by integrating the current according to (3.1), starting at full SOC after a standard charge procedure.

$$SOC(t) = SOC_{Start} - \frac{C_{Dch}(t)}{C_{Ref}} = SOC_{Start} + \frac{\int_{t_{start}}^{t} I\, dt}{3600 \cdot C_{Ref}} \tag{3.1}$$

Different pulse power definitions can be used to extract power levels relevant for HEVs. This specification recommends using the average pulse power for evaluation of power fade rate.

The average pulse power is calculated using the measured voltage, current and time:

$$P_{average} = \frac{1}{t_{end} - t_{start}} \int_{t_{start}}^{t_{end}} U \cdot I\, dt \tag{3.2}$$

Note that discharge power (and discharge current) is defined to be < 0.

The ohmic resistance R_{ohm} (3.3, 3.4) is calculated at both the start and the end of the test pulse using a method similar to that used for power calculation, where the current I_2 and I_3 are the currents measured at the start and the end of the pulse to obtain the immediate voltage drop mainly associated to the ohmic resistance of the cell (Figure 3.3). Using a short time difference between t_1 ... t_2 and t_4 ... t_5 it is possible to approximate the measured impedance as the ohmic resistance in the cell, excluding the contribution from the voltage drop caused by reaction kinetics and mass transport:

$$R_{ohm,\,start} \approx \frac{U_1 - U_2}{I_2} \tag{3.3}$$

and

$$R_{ohm,\,end} \approx \frac{U_5 - U_4}{I_4} \tag{3.4}$$

Alternatively, a separate impedance spectroscopy or AC resistance measurement at a fixed frequency ≥ 1 kHz may be used to extract ohmic resistance at start as well as at the end.

An approximate value for the total DC impedance R_{DC} (3.5) of the cell is calculated using the total voltage drop associated with each pulse over a set relaxation time t_6-t_5. In this study two time periods were used: 10 s and 600 s.

$$R_{DC} \approx \frac{U_4 - U_6}{I_4} \qquad (3.5)$$

It should be emphasised that these resistance and impedance values are intended to be used for comparisons during the cycle life tests rather than to be used in battery models, performance calculations etc. For each measurement and calculation of R_{ohm} and R_{DC} the approximate SOC level at $t = t_3$ should be calculated and used as the actual SOC point for each measurement rather than the initial SOC at $t = t_1$.

Despite the varying SOC level it is still possible to use power and DC impedance to evaluate ageing; by using the power measured power at the three SOC levels, it is possible to make a linear interpolation to obtain the power at constant SOC level relative to the measured capacity. This method may not be suitable for detailed forecasts of power capability *vs.* SOC in a real application, but it is sufficiently accurate to give an overview of the performance degradation over time.

3.1.2 Dynamic Response Test

In addition to the maximum pulse power measured in step 4 and 5 (d at room temperature (+23 °C).
Table 1), a short sequence of charge/discharge pulses are performed to evaluate the power efficiency at medium to low current rates (Table 2).

Table 2   Dynamic Response Test performed at +23 °C.

Step	Sub-Step	Description	Duration
4, 5	1	Discharge CC/CV at 2 C-rate, minimum voltage $U_{cut\text{-}off}$[1]	10 s
	2	Discharge CC/CV at 4 C-rate, minimum voltage $U_{cut\text{-}off}$[1]	
	3	Discharge CC/CV at 2 C-rate, minimum voltage $U_{cut\text{-}off}$[1]	
	4	Charge CC/CV at 2 C-rate, maximum voltage U_{max}[1]	
	5	Charge CC/CV at 4 C-rate, maximum voltage U_{max}[1]	
	6	Charge CC/CV at 2 C-rate, maximum voltage U_{max}[1]	

  1. According to specifications from cell manufacturer.

This sequence, also shown in Figure 3.4, contains charge and discharge pulses of 2 and 4 C-rate and is charge balanced. Thus, it can be used to give a comparable measure of the average power efficiency at low to medium current rates. Higher impedance will quickly lead to higher voltage drop and lower efficiency.
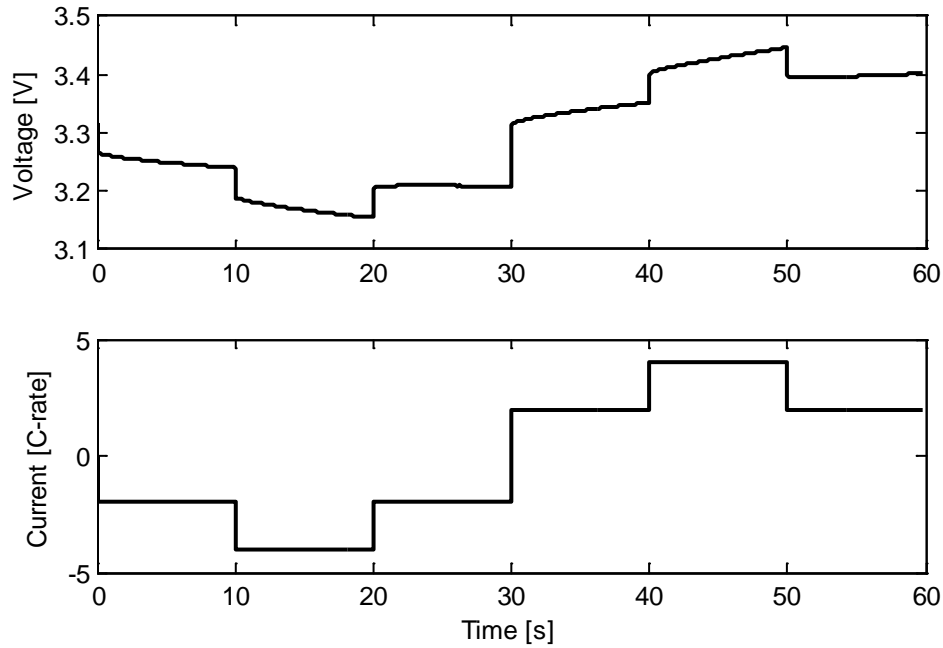
Figure 3.4   Voltage and current during a dynamic response test.

The power efficiency is calculated as the ratio between the discharge energy (0…30 s) and the charge energy (30...60 s) according to (3.6) and presented in Figure 3.5:

$$\eta = \frac{\text{Discharge Energy}}{\text{Charge Energy}} = \frac{\left| \int_0^{30} U \cdot I \, dt \right|}{\left| \int_{30}^{60} U \cdot I \, dt \right|} \tag{3.6}$$

The power efficiency can also be expressed as a function of total impedance and the current:

$$\eta_{\text{charge}} = \frac{\text{Charge Energy - Losses}}{\text{Charge Energy}} = \frac{\int_{30}^{60} U \cdot I \, dt - \int_{30}^{60} R(t) \cdot I(t)^2 \, dt}{\int_{30}^{60} U \cdot I \, dt} \tag{3.7}$$

$$\eta_{\text{discharge}} = \frac{\text{Discharge Energy}}{\text{Discharge Energy + Losses}} = \frac{\int_0^{30} U \cdot I \, dt}{\int_0^{30} U \cdot I \, dt + \int_0^{30} R(t) \cdot I(t)^2 \, dt} \tag{3.8}$$
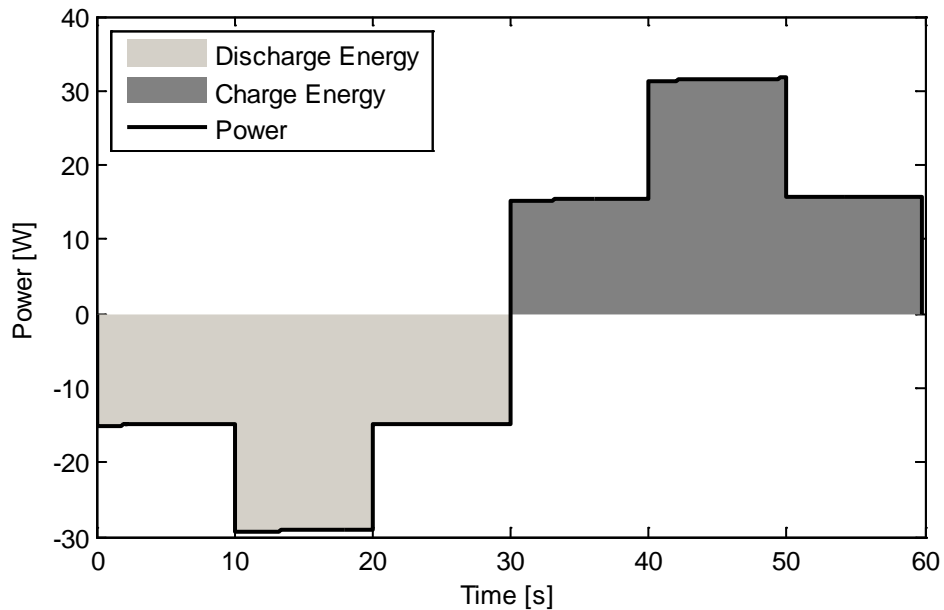
Figure 3.5   Power and energy during a dynamic response test.

3.2 Impedance Spectroscopy

Impedance spectroscopy is an established method for analysis of batteries. It is an especially valuable tool to calculate and observe changes in mass-transport properties, double layer capacitance, ohmic resistance and kinetics of the cell. Nevertheless, an extensive use of this method adds cycling of the cell, in particular if properties at multiple SOC-levels are to be measured. Moreover, test cells often need to be manually disconnected from the battery test equipment and tested at a separate EIS instrument, particularly if higher frequencies are to be used. Hence, this method has not been used as often as the RPT in the test sequence in this study.

Often EIS measurements are presented in a *Nyqvist* graph where the imaginary part of the impedance is plotted *vs.* the real part. An example of such EIS spectrum with included calculated values of ohmic resistance and charge transfer resistance is presented in Figure 3.6.
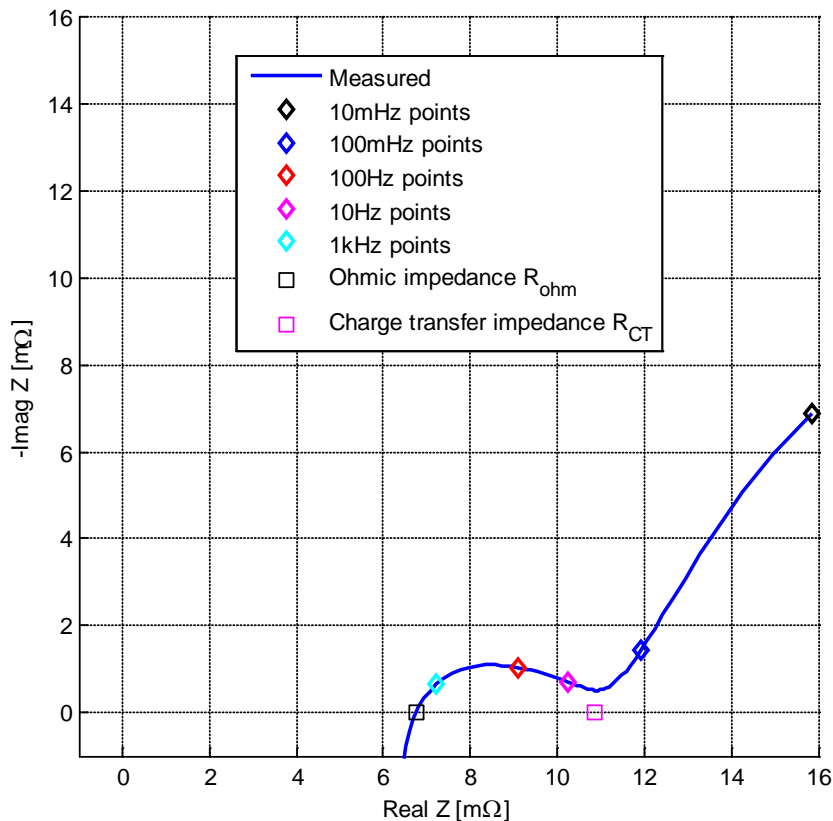
Figure 3.6   Typical Nyqvist graph for one of the LiFePO$_4$ // graphite cells at SOC=50%.

Typically, every other RPT has been followed by an EIS measurement at three SOC-levels: 20, 40 and 60% SOC respectively. At EOL a detailed EIS was measured at SOC-levels [0:10:100]%.

From the measured EIS a number of key parameters (see Figure 3.6) were extracted using least-square fitting to the model [24], [67] in Figure 3.7:

- *Ohmic Impedance R$_{ohm}$*: the intersection with the real axis of the impedance curve in the Nyqvist graph
- Charge Transfer Impedance RCT: the real impedance approximately at the position of the local minima of the impedance curve in the Nyqvist graph, typically between 100 mHz and 10 Hz
- Inductance L: inductance of battery cell and conductors, modelled with a modification to account for measurement artefacts.
- Double Layer Capacitance CDL: modelled as a constant phase element (CPE)
- Warburg Impedance W: modelled as a constant phase element (CPE)
- Selected impedance magnitude (Z, [Ohm]): data at frequencies 1 kHz, 100 Hz, 10 Hz, 100 mHz and 10 mHz
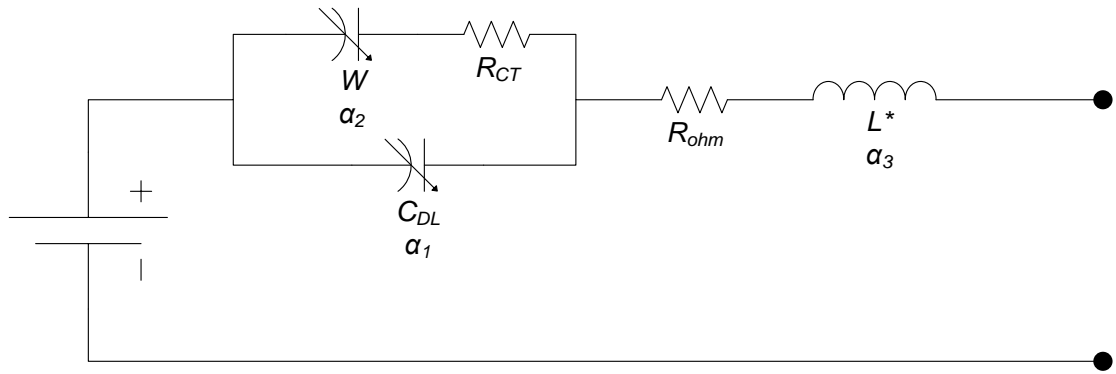
Figure 3.7   Small-signal impedance model for a Li-ion battery cell with parameters extracted *via* least-square fitting method.

The transfer functions of the CPEs and the modified inductance is given by

$$Z_{CPE} = \frac{1}{(j\omega)^\alpha C} \tag{3.9}$$

and

$$Z_{L*} = (j\omega)^\alpha L \tag{3.10}$$

where $0 < \alpha < 1$.

The modification of the inductance with the use of the α-parameter causes the inductive part of the impedance curve to bend slightly towards higher real impedance at higher frequencies. This behaviour, as shown in the inductive part of Figure 3.8, is likely to be due to inaccuracies in the measurements at high frequencies, stray inductance in cell connections and the skin effect in cables
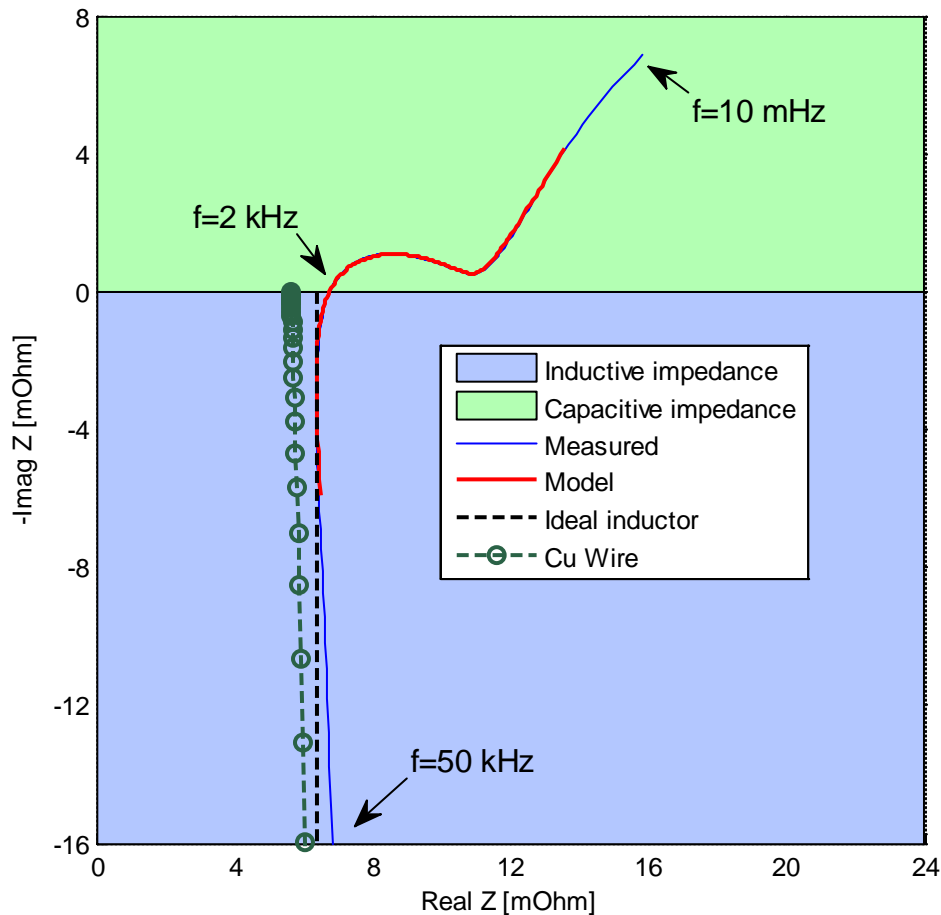
Figure 3.8   EIS curve example with high frequency part compared with ideal inductance and copper
              wire measurement, showing the non-ideal inductance for –Imag(Z)<0.

To verify that the non-ideal inductive behaviour shown in Figure 3.8 is not caused by
the battery cell itself, an additional impedance measurement of a thin copper wire was
made in the frequency range of 1 Hz – 50 kHz. The copper wire was mounted in the
same cell fixture that was used for cell measurement (see Figure 3.9) and consisted of
nine conductors, each approximately 0.19 mm in diameter. The resistance of this wire is
approximately equal to the ohmic resistance of the cell:

$$R_{wire} = \rho \frac{l}{A} = 1.67 \cdot 10^{-8} \frac{0.1}{9 \cdot \pi \left(95 \cdot 10^{-6}\right)^2} = 6.5 \text{ m}\Omega \tag{3.11}$$
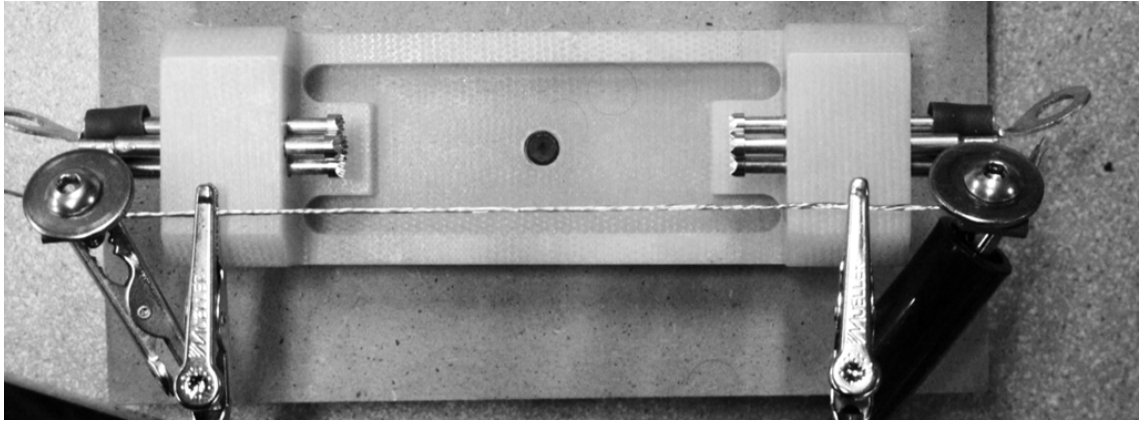
Figure 3.9   Cell fixture for EIS with mounted copper wire. The distance between the voltage sense cables is *ca* 10 cm.

The EIS spectrum of the copper wire shows the same high frequency characteristics as the high frequency part of the cell EIS spectrum (Figure 3.8). Thus, it can be concluded that the non-ideal inductive behaviour is not caused by the cell.

However, no data from this part of the curve is used for further analysis. Hence, the modification of the inductance L^* according to (3.10) can be done solely to increase the performance of the EIS model to gain better stability in the parameter fitting procedure.

3.3 In-cycle SOC adjustment

Testing and using batteries at charge-sustaining mode, partial-charge mode is a challenge in itself. This is particularly true for Li-ion cells based on $LiFePO_4$ and NiMH-batteries, having a flat voltage profile over a wide SOC range. Columbic charge counting (current integration) can only be used for a short time period for tracking of SOC, especially since the dynamic cycle properties consists of pulses in a wide current range and with varying rise time.

Several cycle life test procedures [46]-[48] recommend that cells are fully charged or discharged at regular intervals when tested under laboratory conditions, but this can lead to accelerated ageing as each SOC-adjustment in itself adds significant charge/discharge capacity throughput. Furthermore, such full charge or discharge step is not likely to occur in a real HEV application.

Despite the obvious disadvantages of a flat voltage profile depicted in Figure 3.10, one advantage of this profile is that the phase changes of the graphite is easily detected (see section 7.1. The phase change between stage-4 and stage-3 can be observed just below SOC=30% for this battery type as a comparably rapid change in voltage derivative (dU/dt). Thus, it is possible to adjust SOC to approx. 30% without discharging the cell completely. However, in order to observe the change in voltage derivative it is vital to ensure that the cell is in semi-steady state before start of the discharge.
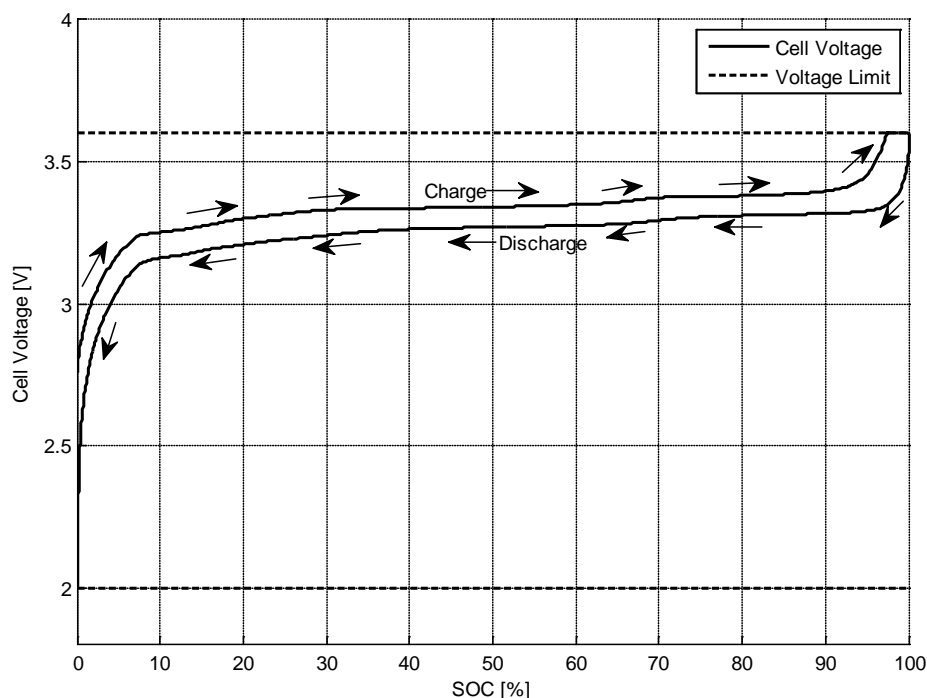

Figure 3.10   Voltage profile at C/4 *vs.* SOC for LiFePO$_4$ // Graphite cell.

A procedure consisting of five steps (see Figure 3.11 and Table 3) was developed and tested.

Table 3   SOC adjustment procedure to find SOC ≈ 30%.

Sub-Step	Description	Limit
1	Charge at 2 C-rate	Reset to start SOC
2	Charge at 1 C-rate	17.4% ΔSOC or U > 3.385 V
3	Discharge at C/4 C-rate	U < 3.290 V
4	Discharge at C/4 C-rate	dU/dt > -0.5 mV/min or U < 3.260
5	Discharge at C/4 C-rate	dU/dt < -1.5 mV/min

The first two steps are performed to ensure that the battery SOC is well above the SOC associated to the change in voltage derivative. After the charge steps, three discharge steps are performed to detect the voltage derivative associated to the target phase change that corresponds to the target SOC value.
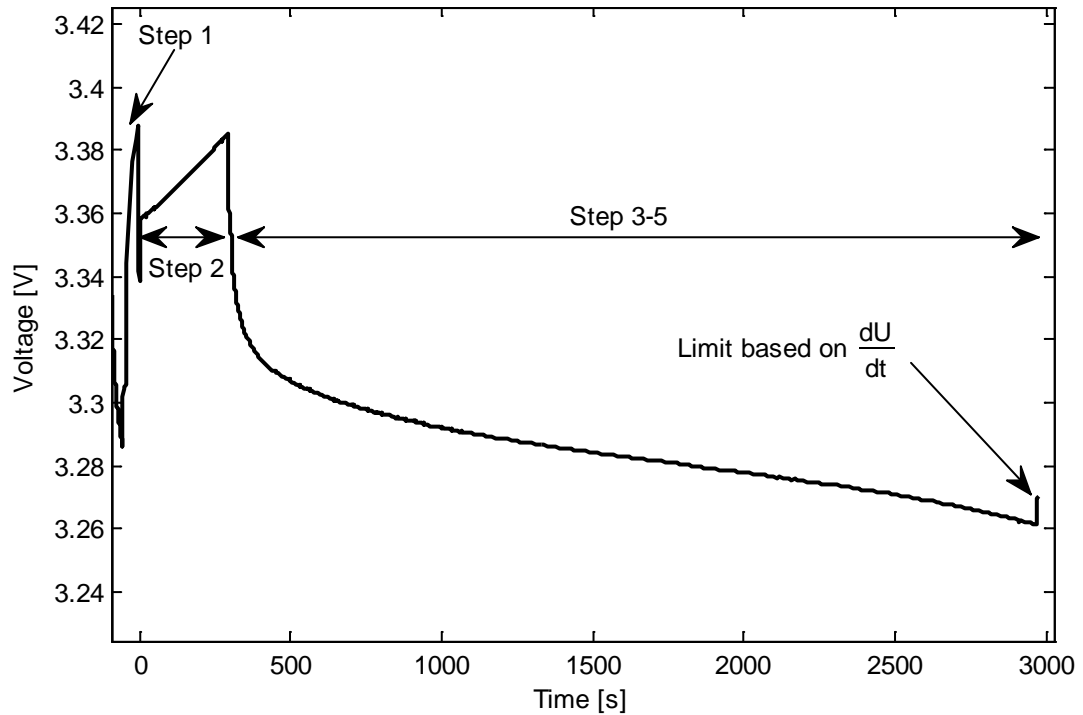
Figure 3.11   Example of SOC adjustment procedure following a load cycle test.

It must be emphasized that the current rates and limits used in this procedure were tailored to a specific cell, thus unlikely to be directly applicable to other cell types / sizes / brands. Another disadvantage with this method is that is time consuming; for the cells tested in this work 45-60 min is needed to complete one SOC adjustment procedure. On the other hand, the low current rates used and the resulting SOC range / voltage range can be regarded as a rest period for the battery in turn resulting in negligible ageing, or even reducing the overall ageing rate. In addition, since this procedure is based on potentiostatic measurements it is independent from capacity degradation. Any procedure based on a full discharge / charge followed by SOC reset by columbic counting must be adjusted for the actual battery capacity over the test, whereas a potentiostatic method will set the battery at the same SOC related to lithium content in the anode.

Depending on the accuracy of the battery test equipment the need for additional SOC-adjustment may vary. For the tests covered by this work it was experimentally proven that one adjustment every third hour was sufficient to keep the SOC within a ±5% range from the desired target SOC.

3.4 Temperature Control

In addition to the SOC range, the average cell temperature has been widely considered as an important ageing factor. Thus, all commercial HEVs and PHEVs are equipped with a separate thermal management system to maintain the battery temperature within a narrow temperature range. Usually, the cell temperature is controlled between +20 °C and +45 °C during normal operation with either cooling or heating systems. In fact, some HEV battery systems are controlled within an even more narrow temperature range. Two cases have been studied; cells at room temperature (+23 °C) in free convection and cells in +35 °C in forced convection in a climate chamber. It is beyond the scope of this investigation to cover a full study of this ageing parameter. However, the temperatures studied are still representative for what may be considered as standard battery environment.

Cells tested with the reference *Cycle A* (see section 4.1) and the wide-SOC constant current *Cycle C* (see section 4.4) were cycled at both room temperature and +35 °C, the other cases were cycled at either the lower or the upper temperature. Due to internal losses all cells under test will experience significant self-heating. Added to this, the air convection conditions also have a significant effect on the actual, average temperature under cycling. For cells cycled at room temperature, most cells showed 10-12 °C increase in temperature above ambient, and the cells in the climate chamber had 5-7 °C increase due to more effective convection and generally lower internal losses at higher temperature. Consequently, the two selected temperature conditions are +33-35 °C for cells outside climate chamber and +40-42 °C inside the chamber. Despite the narrow actual temperature range, previously published results have indicated that comparably small increases in temperature may result in a significant reduction in cycle life [39], [38].

3.5 Half-Cell Tests

In order to get insights in the individual electrode properties of the graphite anode and the LiFePO$_4$ cathode studied in the present work a series of experiments using half-cells (see section 5.1) was performed. First and foremost the voltage profiles as a function of current rate and individual electrode SOC were measured and used to validate analysis methods (see section 7.2). Although the half-cells were manufactured from commercial grade material, their mechanical and electrical design is profoundly different from commercial cells. Hence, their impedance is significantly higher per unit capacity than that of the commercial, power-optimised cells used for cycle life tests. Consequently, the voltage drop due to ohmic resistance and polarisation (mass transport) must be taken into consideration when testing the cells. In contrast to the RPTs, the half-cell tests involved constant current charge and discharge steps only. An overview of these tests is given in Table 4.

Table 4   Test procedure for half-cell tests performed at +23°C.

Sub-Step	Description	Duration [h]
1	Discharge CC at I_{test}[1] C-rate, minimum voltage $U_{cut\text{-}off}$[3]	2-25
2	Pause	1
3	Discharge CC at I_{low}[2] C-rate, minimum voltage $U_{cut\text{-}off}$[3]	1-5
4	Pause	3
5	Charge CC at I_{test}[1] C-rate, maximum voltage U_{max}[4]	2-25
6	Pause	1
7	Charge CC at I_{low}[2] C-rate, maximum voltage U_{max}[4]	1-5
8	Pause	3

1. I_{test} = C/25, C/10, C/5, C/2, C/1 C-rate.
2. I_{low} = C/25.
3. $U_{cut\text{-}off}$ = 0.01 V for graphite/Li cell, 2.7 V for LiFePO$_4$/Li cell.
4. U_{max} = 2.0 V for graphite/Li cell, 4.0 V for LiFePO$_4$/Li cell.

The test procedure starts with a full discharge with constant current (I_{test}) until the cell voltage is equal to $U_{cut\text{-}off}$. This step is followed by a rest period and a second discharge at low current rate (I_{low}) to ensure that the cell is fully discharged regardless of a possible early termination of step 1 due to high voltage drop. Likewise, the cell is re-charged with I_{test} and I_{low} in two steps. This charge/discharge procedure is repeated three times for each tested current rate; C/25, C/10, C/5, C/2 and C/1 C-rate. Test results from these tests are presented in section 7.3.

Chapter 4   Load Cycles

Since the ageing mechanisms of Li-ion battery cells are non-linear and dependant, it is rarely possible to isolate one mechanism at a time and test its' specific dependence on operating conditions. This is especially the case in HEV applications designed for optimum cycle life; controlled temperature range, SOC range and current range. One illustrative example is a hybrid electric city-bus designed to reduce fuel consumption by recuperating brake energy and avoid idling. In 2009, AB Volvo introduced their first series manufactured HEV city bus. Being one of the most likely candidates for hybridisation of heavy-duty vehicles, this application was chosen as the basis for the reference battery load profile, *Cycle A*, for the cycle life test presented in this thesis

Using this reference cycle as the premises for all tests performed, a number of different load cycles was derived and used in cycle life tests, if possible, to find the relation between specific ageing factors and the load cycle properties:

- a synthetic load cycle, *Cycle B*, was designed based on stochastic process model of the reference cycle
- simplified cycles with constant current for charge and discharge; *Cycle C* with a wide SOC range and *Cycle D* with a narrow SOC range
- an adaptation of a PHEV-cycle, *Cycle E*, representing a compromise between complex logged cycles and simplified average cycles.

This section describes the adaptation of a reference load cycle, the method for synthetic load cycle extraction, the set-up of simplified load cycles and a summary of cycle properties for all tested cycles.

4.1 Reference Load Cycle, *Cycle A*

Naturally, the drive cycle and corresponding load cycle for the battery differs between markets, countries, operators, vehicle options / add-on etc. However, since the work presented in this thesis concentrates on the actual ageing, the selection of battery load cycle is not critical as long as it is representative for the target vehicle. A drive cycle from a city-bus route in Gothenburg, Sweden, was selected for use as a realistic case for

a heavy-duty HEV. The speed, altitude and slope angle for this drive cycle are shown in Figure 4.1. Here, the frequent start-stop it is noticeable as well as the low average speed. Despite the low average speed, a high peak power outtake from the powertrain is needed to achieve acceptable acceleration and hill-climbing capability as the bus-route includes significant slope angles.
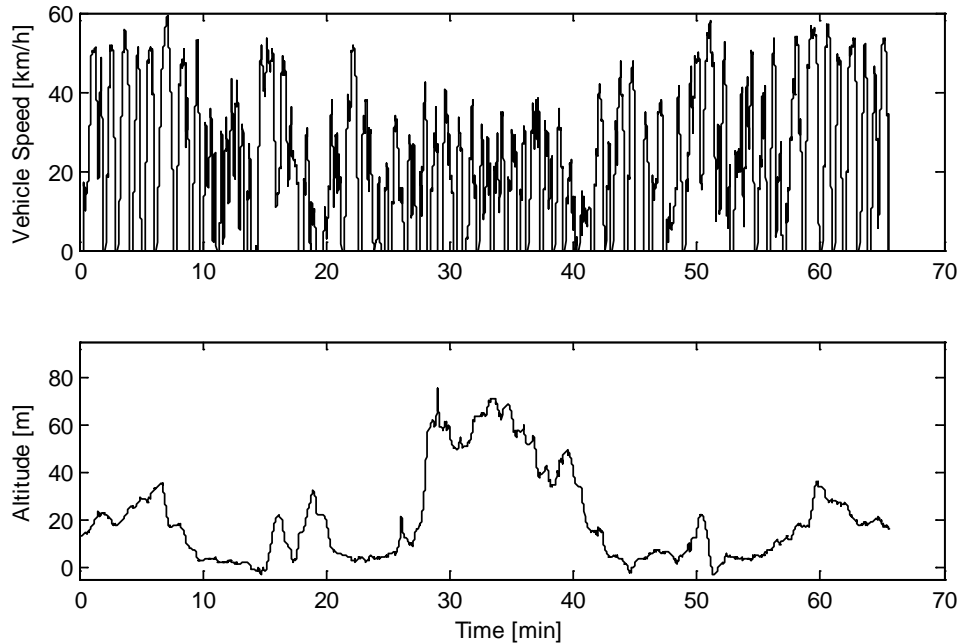

Figure 4.1   HEV City-bus drive cycle used to derive the reference load *Cycle A*.

Several test drives have been performed with a prototype HEV city-bus on this particular drive cycle. The battery current, voltage, SOC and temperature was sampled at 10Hz during a road test and used as the reference battery load cycle for the cycle life tests presented in this work. This load cycle consists of about 40 000 logged values of current *vs.* time. In order to use it for laboratory cycle life tests it was filtered with a 10 point / 1 s moving average filter in combination with a sample-and-hold filter. The resulting load profile has a minimum step duration of 1.0 s, effectively reducing the number of steps to about 2 000 with a minor loss of dynamics; the filtered cycle (Figure 4.2) shows negligible difference in current distribution, peak values and capacity throughput compared to the logged cycle.
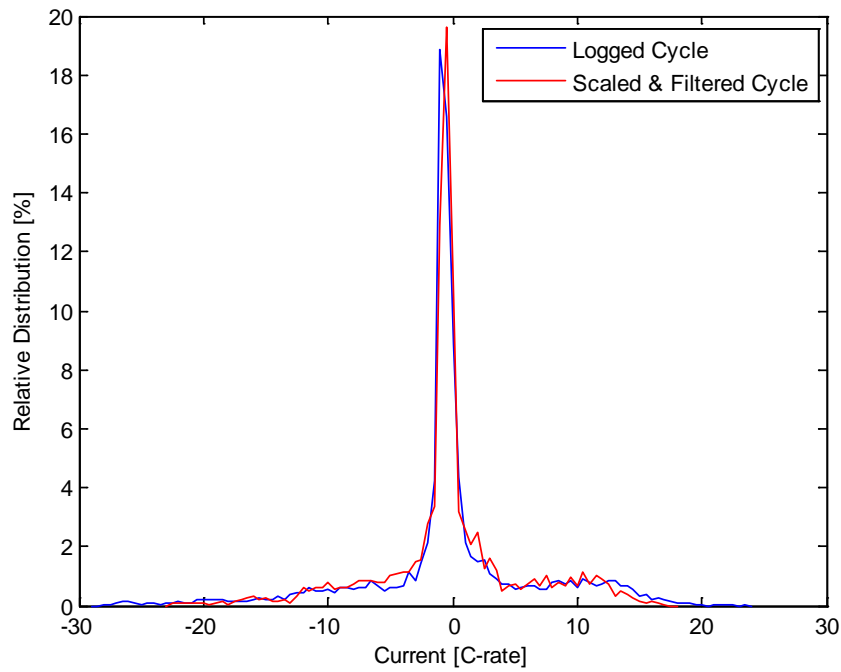
Figure 4.2   Comparison of current distribution between logged and filtered/scaled load cycle.

In addition, the power in the original profile was scaled to 80% and reduced in peak charge current to comply with the maximum current rating of the selected test cells.

A sample of the current for the first two minutes and the SOC for the entire cycle is shown in Figure 4.3 and Figure 4.4, respectively.
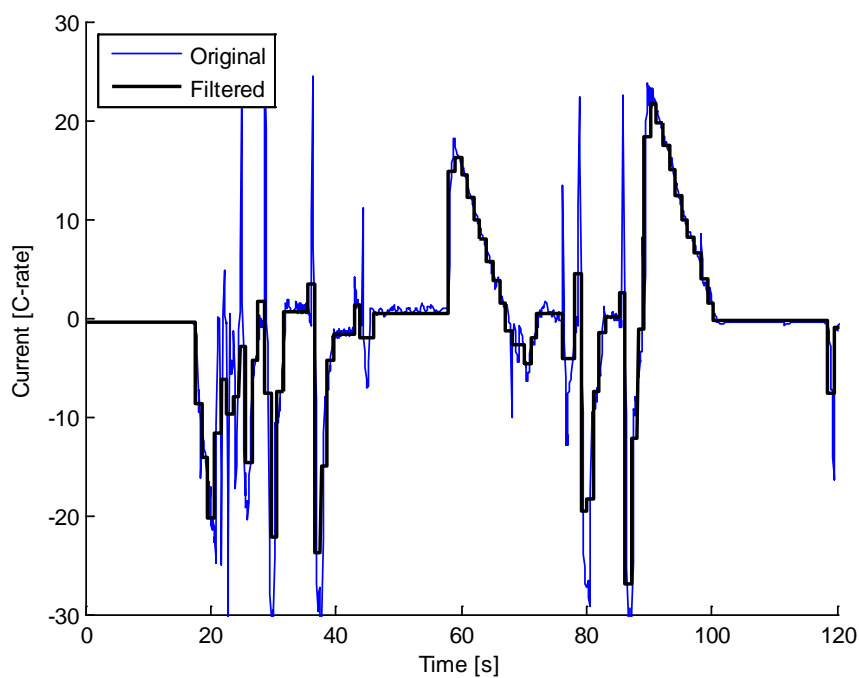

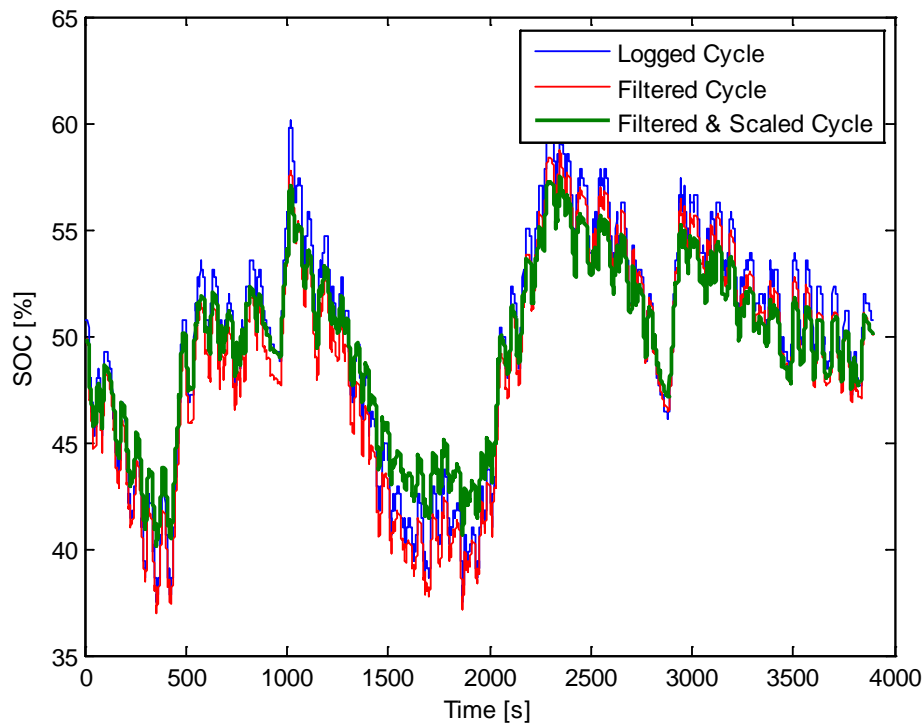Figure 4.3   Comparison of logged and filtered cycle, first 180 s.

Figure 4.4   Comparison of SOC for logged, filtered and scaled cycle.

Despite the scaling, the excluded fast transients in the original cycle are not believed to have a significant impact on cycle life. Also, the use of fast transients (<0.1 s) increases the electrical requirements on the battery test equipment significantly, in turn leading to a risk that results from different battery load cycles cannot be compared. That is, if the transient duration is equal or shorter than the minimum step time of the battery test equipment, the set-values and actual values may differ and the reproducibility may differ between different load cycles.

High average SOC-range is known to lead to an accelerated ageing of Li-ion batteries [6]. Furthermore, SOC below 20% may also accelerate ageing of first and foremost the graphite anode due to mechanical stress associated to lithium intercalation [68] (see section 2.3). Likewise, comparably high cell temperatures may also dominate the ageing processes if tested. The main objective of this work is to investigate most significant ageing factors in real operating conditions. Consequently, the average SOC of the reference load cycle was lowered to yield an approximate SOC-range of 25…55% and the target temperature set to +25...+45 °C.

A comparison of the logged cycle, the scaled and filtered version of the reference load cycle is shown in Table 5. Here, it should be noted that the scaled load cycle is less severe than the logged cycle in all aspects. The definition of RMS current (root-mean-square), average current and capacity throughput are according to (4.1) to (4.3), where T_{cycle} is the total load cycle time and $C_{Nominal}$ is the rated cell capacity.

Table 5   Comparison between measured and filtered battery load cycle.

Parameter	Logged Cycle	Filtered & Scaled Cycle	Reference *Cycle A*
Average SOC [%]	49.7	50.2	38.5
Minimum SOC [%]	37.5	40.9	22.6
Maximum SOC [%]	60.2	58.3	50.0
RMS Current [C-rate]	6.86	5.79	5.01
Average Current [C-rate]	4.17	3.65	2.82
Total Capacity Throughput [C-rate]	4.52	3.95	4.05
Peak Charge Current [C-rate]	23.9	17.3	17.3
Peak Discharge Current [C-rate]	28.2	22.3	22.3
Cell Temperature [°C]	+20...+50	+25…+45	+23..+40

$$I_{\mathrm{RMS}} = \frac{1}{T_{cycle}} \sqrt{\int_0^{T_{cycle}} i^2 dt} \cdot \frac{1}{C_{\mathrm{Nominal}}} \tag{4.1}$$

$$I_{\mathrm{Mean}} = \frac{1}{T_{cycle}} \int_0^{T_{cycle}} i \, dt \cdot \frac{1}{C_{\mathrm{Nominal}}} \tag{4.2}$$

$$C_{\mathrm{Throughput}} = \int_0^{T_{cycle}} |i| dt \, \frac{1}{C_{\mathrm{Nominal}} \cdot 3600 \cdot 2} \tag{4.3}$$

4.2 Synthetic Cycle Extraction

Despite adding filtering and other signal conditioning of logged cycles, a logged cycle is still only representative for a particular target vehicle and the actual operating conditions at the time of measurement. An alternative method of extracting a shorter, simplified load cycle based on one or several measured cycle was developed to investigate the degree of sensitivity to simplification with regard to battery ageing characteristics [69].

The primary target for the work presented in this section is to find an objective, reliable method to simplify dynamic battery load cycles for use in cycle life tests. In addition, the method should be a tool for evaluating how applicable results from different load cycle tests are to a particular application.

First and foremost this method is developed for use in cycle life tests of Li-ion batteries optimized for heavy-duty HEVs. There are however no direct restriction to the usage of the method to the testing of other secondary batteries.

This method uses a statistic approach for analysing measured battery load cycles in terms of a number of key properties such as power distribution and energy throughput. This stochastic cycle model is then used to compare cycles and to generate new synthetic load cycles where key parameters such as average power and current rate can be adjusted while keeping other properties of the cycle constant. In addition, the method can be used to reduce the total load cycle length to a minimum which further simplifies the test setup. Specifically, this work covered an investigation of the suitability of using a *Markov* chain as a model for the battery load cycle in heavy-duty HEV applications.

Firstly, the theoretical background of the method is presented. Secondly, a simplified charge sustaining algorithm is added to the system to control the SOC during longer load cycles. Thirdly, the method is used to generate a new synthetic load cycle based on the reference cycle from an HEV city-bus.

4.2.1 Stochastic Model of Load Cycle

A full background to the technique is given in [70], and several papers present possible examples where load cycles are generated by using *Markov* chains: [71]-[76].

This method can easily be adapted to HEV load cycles by converting the power into discrete power levels in a state-vector S in which each level represents a unique state. A probability matrix Q, called the *Markov* matrix, can then be formed where the probability for transition from state i to state j is equal to element Q_{ij}:

$$Q_{ij} = P(S_{n+1} = i \mid S_n = j) \tag{4.4}$$

$$Q_{ij} = \begin{bmatrix} S_1 \to S_1 & S_2 \to S_1 & \cdots & S_n \to S_1 \\ S_1 \to S_2 & S_2 \to S_2 & \cdots & S_n \to S_2 \\ \vdots & \vdots & \vdots & \vdots \\ S_1 \to S_m & S_2 \to S_m & \cdots & S_n \to S_m \end{bmatrix} \tag{4.5}$$

where S_{n+1} is the next state (power level), S_n is the current state and P is the probability for a transition from S_n to S_{n+1}.

The $m \times m$ matrix Q is typically a sparse matrix with the greatest elements around the diagonal $Q_{1,1}$ to $Q_{m,m}$. Each column sum must be equal to 1, since the cumulative probability for transition to any possible new state must be unity for each current state. This is however only true if all states in the state vector are entered in the real load cycle. If not, numeric problems might occur depending on the implementation. The Q matrix is defined by analysing one or several load cycles so that each element in the matrix is populated with the corresponding probability.

A new, synthetic cycle of any length can then be calculated using a minimum of tools, which will be further described in section 4.2.2:

1. an initial state in the S-vector for which the corresponding column sum $\neq 0$
2. a random number generator

Changes and adaptations to the probabilities in the Q matrix should be avoided to preserve stability. Instead, power levels can either be adjusted according to an independent weight function before the population of the Q matrix or the output state can be adjusted by selecting either a higher or lower power level than the one generated by the random function. Even though such modifications to the cycle are in conflict to the stochastic approach, it will in practice be necessary to include them to first and foremost keep the SOC within the admissible range.

There is a specific issue related to the selection of states to include in the *S* vector. Depending on the choice and the cycle properties the *S* vector and the *Q* matrix may contain empty states / empty column. These states might in turn cause instabilities to the cycle generation. There are two obvious solutions to this issue:

1. The corresponding column in *Q* can be populated as the linear interpolation between adjacent columns. This method will generate a stable output but may cause the output synthetic cycle to consist of power levels never observed in the real cycle.
2. The SOC algorithm can be changed to avoid selecting states (power levels) not observed in the real cycle.

In theory this choice may not be important, but in practice when using standard random number generators in for example MATLAB® it may be relevant as described further in the following section. The second method was selected to ensure that the procedure can work with a large variety of load cycles in combination with a comparably large *Q* matrix.

4.2.2 Implementation

Firstly, the *S* vector of length *m* is selected to correspond to the reference load cycle properties. The *m x m* matrix *Q* is then formed by stepping through the reference load cycle and incrementing the corresponding state $Q_{n,x}$ for each step, followed by the normalization of the columns by the total column sum. The first step in this "learning"-process can be repeated for every measured (or simulated) load cycle that should be included in the synthesis as long as the sample rate is the same for all cycles and the total number of cycle steps for all cycles are used to normalize the columns in the second step.

At this stage it is also possible to introduce limitations, weight functions, or in other ways change the properties of *Q* and any generated synthetic cycles compared to the input cycle(s).

Following the calculation of the *Q* matrix, a synthetic cycle can be generated step-wise using a general random number generator. In MATLAB, this can be done by creating a support matrix, Q_s, consisting of the cumulative column sum of *Q* and the random

generator **rand**; the column in Q_s corresponding to the current state is compared by a random number [0…1] and the element closest to the random number is selected as the next state. That is, the output state is the first row index n of $Q_s(n,x)$ that satisfies the relation $Q_s(n,x) >$ **rand** where x is the current state and n is the next state. Simplified examples of Q and Q_s are shown in (4.11) and (4.12). These examples are however not representative to HEV cycles.

This short algorithm is repeated for each step in the cycle starting the initial state x_0 corresponding to the initial power level. The output state n of each iteration is used as input state I for the next calculation. There is no theoretical limit to the total length of the synthetic cycle. In practice the length will however be limited by a lower limit determined by the requirements on correspondence with the reference cycle (see section 4.2.6).

$$Q = \begin{bmatrix} 0.9 & 0.05 & 0 & 0 & 0 & 0 & 0 & 0 & 0 & 0 \\ 0.05 & 0.8 & 0.2 & 0.1 & 0 & 0 & 0 & 0 & 0 & 0 \\ 0.04 & 0.05 & 0.7 & 0.2 & 0.08 & 0 & 0 & 0 & 0 & 0 \\ 0.01 & 0.05 & 0.1 & 0.6 & 0.02 & 0.06 & 0 & 0 & 0 & 0 \\ 0 & 0.03 & 0 & 0.05 & 0.9 & 0.04 & 0.03 & 0 & 0 & 0 \\ 0 & 0.02 & 0 & 0.05 & 0 & 0.8 & 0.17 & 0.01 & 0.04 & 0 \\ 0 & 0 & 0 & 0 & 0 & 0.1 & 0.5 & 0.03 & 0.06 & 0 \\ 0 & 0 & 0 & 0 & 0 & 0 & 0.2 & 0.95 & 0.1 & 0 \\ 0 & 0 & 0 & 0 & 0 & 0 & 0.1 & 0.01 & 0.7 & 0.2 \\ 0 & 0 & 0 & 0 & 0 & 0 & 0 & 0 & 0.1 & 0.8 \end{bmatrix} \tag{4.6}$$

$$Q_s = \begin{bmatrix} 0.9 & 0.05 & 0 & 0 & 0 & 0 & 0 & 0 & 0 & 0 \\ 0.95 & 0.85 & 0.2 & 0.1 & 0 & 0 & 0 & 0 & 0 & 0 \\ 0.99 & 0.9 & 0.9 & 0.3 & 0.08 & 0 & 0 & 0 & 0 & 0 \\ 1 & 0.95 & 1 & 0.9 & 0.1 & 0.06 & 0 & 0 & 0 & 0 \\ 1 & 0.98 & 1 & 0.95 & 1 & 0.1 & 0.03 & 0 & 0 & 0 \\ 1 & 1 & 1 & 1 & 1 & 0.9 & 0.2 & 0.01 & 0.04 & 0 \\ 1 & 1 & 1 & 1 & 1 & 1 & 0.7 & 0.04 & 0.1 & 0 \\ 1 & 1 & 1 & 1 & 1 & 1 & 0.9 & 0.99 & 0.2 & 0 \\ 1 & 1 & 1 & 1 & 1 & 1 & 1 & 1 & 0.9 & 0.2 \\ 1 & 1 & 1 & 1 & 1 & 1 & 1 & 1 & 1 & 1 \end{bmatrix} \tag{4.7}$$

As mentioned in previously, a problem with SOC exceeding the maximum limits might occur when battery load cycles from charge-sustaining HEVs are studied, especially if the cycles are comparably long and the energy throughput is in the range of the usable energy content of the battery. In such cases the SOC of the target battery must be

calculated for each time step and then, via a predefined SOC control strategy, be used to adjust the output power for the next step to limit the required SOC range. Thus, the battery load cycle cannot be treated as a purely stochastic process from a strictly fundamental standpoint unless the battery capacity is infinitely large or the load cycles are very short in duration. Nevertheless, this limitation of the proposed method is still viable since it replicates the situation in a real HEV where the drive pattern and road profile may be considered as stochastic whereas the actual battery current is limited and controlled by a control unit based on a non-stochastic strategy. If, in addition, the *S* vector is composed by representative levels with a high number of levels, the SOC strategy will only have a minor impact on cycle properties in terms of power and energy. This issue and a proposed solution are presented in detail in the following sections, where the first part presents the definition of SOC and the associated battery model, followed by an example of a simple SOC preserving control strategy for use in the synthetic cycle generation.

4.2.3 Battery model used for SOC-estimation

The SOC of a battery is typically defined as the ratio between the available discharge capacity and the maximum discharge capacity at a specific temperature and SOH:

$$
SOC(t) = \frac{C_{reference}[\text{As}] - C_{\text{discharged}}(t)[\text{As}]}{C_{reference}[\text{As}]} =
$$

$$
= \frac{C_{reference}[\text{As}] - \int_0^t I\,dt}{C_{reference}[\text{As}]}
$$

(4.8)

While the SOC in an HEV is carefully controlled to ensure the performance and durability of the battery throughout the design lifetime, this is not the case for the generated stochastic cycle according to the *Markov* process. However, the average SOC for any truly stochastic cycle will be equal to the initial SOC for an infinitely long cycle if the total probability for charge is equal to the probability for discharge, capacity wise. This is naturally not the case for real cycles of finite length, especially not for HEV batteries with a comparably high energy throughput. Consequently, the resulting SOC of the synthetic cycle must be controlled according to a predefined strategy using a similar method as is implemented in a real HEV.

Firstly, a method for a step-wise calculating SOC during the extraction of the synthetic cycle is selected. Using a simple *Thevénin* equivalent circuit model and a fixed value for the reference capacity $C_{reference}$, the *SOC(t)* is numerically calculated as the *Euler* approximation of the integrated current in each step. If the load cycle is characterised by constant power levels rather than current levels, a separate algorithm for estimation of current must be added. Any battery model able to calculate current from a power input is possible to use at this stage. For simplicity, a rudimental model is used here:

$$U(t) = U_{OCV}(t) + R(t)I(t) \tag{4.9}$$

Assuming the typically narrow SOC range of most Li-ion batteries designed for HEVs, the average open circuit voltage U_{OCV} may be regarded as a constant. Similarly, the internal resistance can be simplified using a single value or a limited set of values to further simplify the equation. Due to limited current measurement accuracy any real cycle life test must include a separate SOC adjustment procedure which is described further in section 3.3 in this thesis.

Starting from the input power to the battery, the power /current relation in (4.10) must be satisfied for all time steps.

$$P(t) = U(t) \cdot I(t) = U_{OCV}(t) \cdot I(t) + R(t) \cdot (I(t))^2 \tag{4.10}$$

Solving this equation for each time instant yields a time-varying current vector to be used in SOC-estimation.

Secondly, an appropriate SOC strategy is added to keep the SOC of the battery within the acceptable range throughout the duration of the synthetic cycle. This approach, or any other SOC preserving method, is absolutely essential when extracting synthetic cycles in which the energy throughput is comparable to the maximum usable energy of the battery.

4.2.4 SOC Control Strategy

Naturally, there are numerous ways to control the SOC in an HEV. That is especially challenging for cycles with an energy throughput that is comparable to or exceeding the usable battery energy. A synthetic load cycle could either be designed to replicate the SOC trends of the target load cycle as accurately as possible, or to reflect the statistical properties of the load cycle using an additional weight function that will control the SOC to stay within the acceptable range. One approach to control SOC is to limit the charge power close to the upper SOC limit and the discharge power close to the lower limit. Rutquist *et al.* [77] suggested the tangent function as the optimal control function *u=f(SOC)* for a simplified system with a supercapacitor energy storage. This strategy may be expanded to batteries, at least within a narrow SOC range, and was therefore used in this method.

Regardless of which strategy that is chosen, a stable weight function that limits the maximum SOC range of the synthetic load cycle is needed. The reference for this function could either be a static target (SOC_{target}), a dynamic SOC signal according to measured properties or a simulated signal assuming a constant average efficiency of the battery cell.

Since the generated cycle is stochastic, no change made to the *Q* matrix will be efficient to keep SOC within the admissible range. Even small changes in the *Q* matrix defining the *Markov* process might cause severe stability problems in the cycle generation. Hence, the *Q* matrix must be left unchanged and the output power levels must be used to control SOC instead.

The inverse tangent function according to [77] was used to generate a limit function for SOC. This function can be configured with different steepness at the edges (see Figure 4.5).
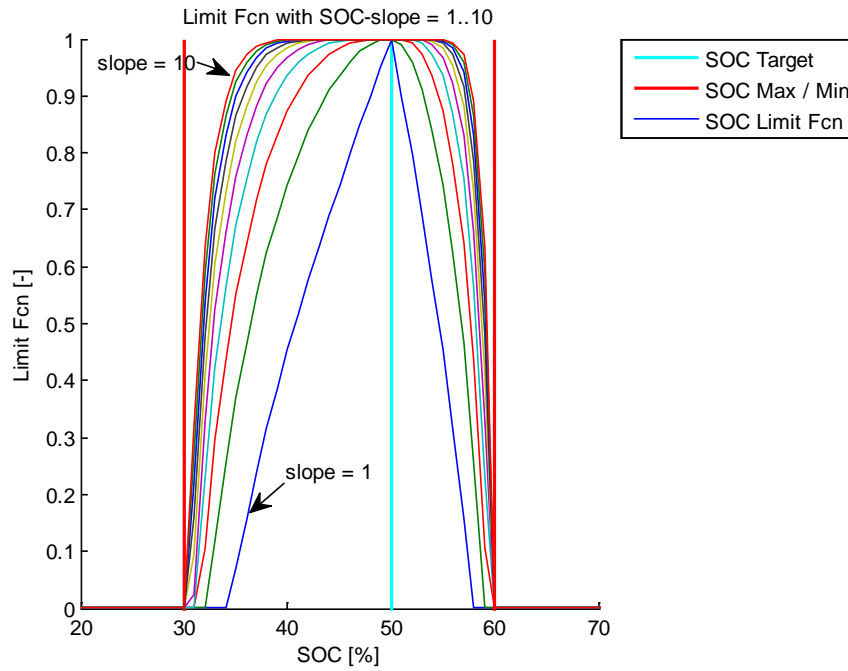
Figure 4.5   Limit function using tangent function and SOC slope between 1 and 10.

For each step generated according to the method described in the previous section, the output power level is weighed with this limit function. If the SOC is close to the target SOC no change is made to the output power. In contrast, when the SOC is close to the limits the target function gradually limits the charge power (at high SOC) and the discharge power (at low SOC). The calculated new power level is then adjusted to fit the pre-defined power levels (states) in the *S* vector. The adjustment factor 0...1 is based on the MATLAB tangent function **tan** according to (4.11) and (4.12).

$$SOC_{\text{Limit Fcn}} = 1 - \left| \tan\left(\left(\frac{SOC - SOC_{\text{target}}}{SOC_{\text{max}} - SOC_{\text{target}}} \right)^{SOC_{\text{slope}}} \right) \right| \tag{4.11}$$

where

SOC_{target} is the centre point of the admissible SOC-range,

SOC_{max} is the maximum admissible SOC,

SOC_{min} is the minimum admissible SOC, and

SOC_{slope} is a control parameter typically between 1 and 10 that determines the steepness of the limit function close to the boundaries.

The limit function $SOC_{Limit\ Fcn}$ varies between 0...1 for SOC between $SOC_{min}...SOC_{max}$ and can be used directly as a multiplication factor for the output power level in each step of the cycle generation:

$$P_{output} = SOC_{Limit\ Fcn} S_{n+1} \tag{4.12}$$

The corrected output state corresponding to P_{output} in (4.12) must then be selected as the power level that best corresponds to the discrete levels in the state vector S for which the probability is larger than zero.

4.2.5 Optimisation

Any cycle generated according to the proposed method will reflect the fundamental properties of the reference cycle. However, the actual SOC characteristics as well as other cycle properties will differ significantly between different synthetic cycles. To find and evaluate solutions / versions of the synthetic cycle with good, objective correspondence to the reference cycle, an optimisation process was run where key aspects such as RMS power, SOC range, and power/energy distribution of the cycle were compared to the reference cycle by means of five weighted error functions

The weighted error functions (4.13) to (4.17) are aimed to provide a continuous feedback to the optimisation process, in turn enabling a stable optimisation process. Difference in SOC over the complete cycle:

$$ERR_{SOC} = K_{SOC} \cdot \frac{1}{n_2 - n_1} \cdot \sum_{n_1}^{n_2} \left| SOC_{synthetic} - SOC_{reference} \right| \tag{4.13}$$

Difference in RMS power and maximum energy window:

$$ERR_{P_{RMS}} = K_P \cdot \left| P_{RMS,synthetic}[kW] - P_{RMS,reference}[kW] \right| \tag{4.14}$$

$$ERR_{W_{window}} = K_W \cdot \left| W_{window,synthetic}[Wh] - W_{window,reference}[Wh] \right| \tag{4.15}$$

Difference in power and energy distribution:

$$ERR_{P_{dist}} = K_{P,dist} \cdot \sum_{S} \left| \frac{hist(P_{synthetic},S)}{N} - \frac{hist(P_{reference},S)}{N} \right| \tag{4.16}$$

$$ERR_{W_{dist}} = K_{W,dist} \cdot \sum_{S} \left| \frac{hist(W_{synthetic}, S)}{N} - \frac{hist(W_{reference}, S)}{N} \right| \qquad (4.17)$$

where

N = number of elements

S = discrete power vector

hist(Y,X) = the histogram (distribution) of Y over X.

The weight factors K_{SOC}, K_P and K_W are set for the specific application to set internal priority between the evaluation measures.

A large number of cycles were generated, each according to the same *Markov* process and with the same settings, as presented in Table 6.

Table 6   Battery properties and SOC-strategy settings.

Parameter	Abbr.	Value	Unit
SOC strategy			
Reference SOC	$SOCtarget$	50	%
Upper SOC limit	$SOCmax$	60	%
Lower SOC limit	$SOCmin$	30	%
Initial SOC	$SOCinitial$	50	%
SOC Limit Function factor	$SOCslope$	10	-
Sampling time	t_{step}	0.1	s
Weight factor, SOC	K_{SOC}	1/10	-
Weight factor, RMS-power	K_P	1/500	-
Weight factor, Energy window	K_W	1/40	-
Battery			
Total energy	$W_{Battery}$	3000	Wh
Total capacity	$C_{Battery}$	5	Ah
Total internal resistance	$ESR_{Battery}$	0.45	Ω
Open circuit voltage at 50% SOC	U_{OCV}	630	V

For sufficiently long synthetic cycles the power distribution and energy distribution over the discrete power vector are expected to be similar to that of the reference cycle. However, this is only the case if the reference cycle can be modelled as a truly stochastic *Markov* process.

Consequently, the shape of the power and energy distribution can be compared to the reference cycle to determine

a)   the validity of the *Markov* process to model the load cycle

b)   the minimum length of the synthetic output cycle to cover the full spectrum   of the reference cycle

Previous sections described the SOC strategy as a necessary perturbation to the true *Markov* cycle since it affects the power levels in the synthetic cycle when the estimated SOC-level is close to the limits.

The method in this study uses the five presented error functions above, with weight factors according to Table 6 set to address specific properties. If the synthetic cycle should be similar to the reference cycle in SOC variations, a larger value should be assigned to the factor K_{SOC}, and similar for the other properties. Naturally it is also viable to use a combination of the K factors to generate cycles that in average corresponds well to the reference cycle. Nevertheless, the fourth and fifth error functions (4.16 and 4.17) should be used to determine the minimum cycle time or minimum cycle length which has the fundamental properties of the reference cycle in terms of distribution of power and energy.

4.2.6 Evaluation

The feasibility of the proposed method has been evaluated based on an investigation of a large number of synthetic load cycles extracted and compared to reference *Cycle A* described in section 4.1. The *Q* matrix was calculated using the measured voltage and current together with the logged SOC level based on this single reference load cycle. In addition, the logged battery data from *Cycle A* was used to extract parameters for the simple battery model needed for SOC estimation.

Using the proposed SOC strategy and general settings for SOC average and SOC limits as well as battery data from a relevant Li-ion battery (see Table 6) a number of synthetic cycles were generated and evaluated according to the error functions (4.13) to (4.17).

Firstly, the minimum cycle length was evaluated using error functions (4.16) and (4.17). The outcome of this part indicated that, for this particular reference cycle and set of

conditions, the cycle must be at least 30% of the original length to capture the fundamental properties. In Figure 4.6 the cumulative error between the power distribution and energy distribution is presented as function of the fraction of the reference cycle length.
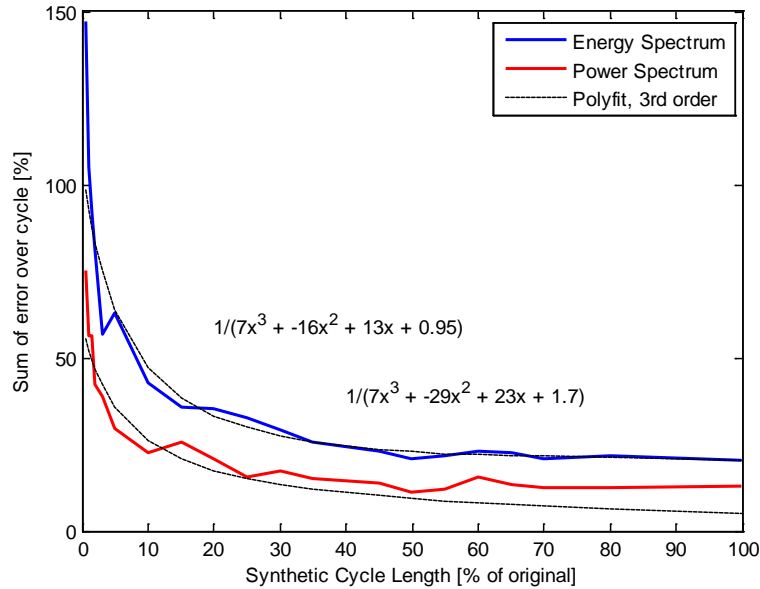

Figure 4.6   Cumulative error between power and energy distribution and the reference cycle for different synthetic cycle length.

The ability of the method to capture the distribution of power and energy is also illustrated in Figure 4.7 where these distributions are shown for 80% cycle length.
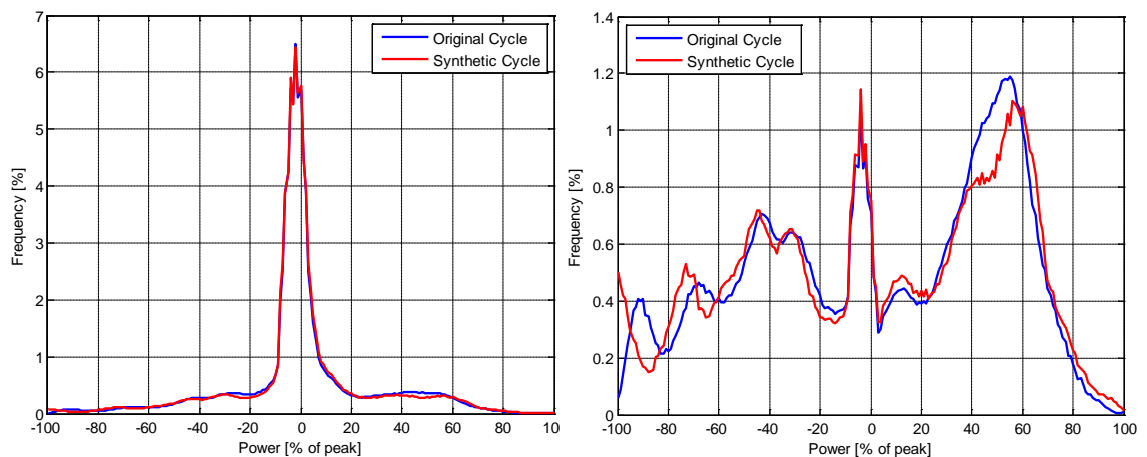
Figure 4.7   Power (left figure) & energy (right figure) distribution at 80% cycle length.

Whereas the power distribution is almost identical to that of the original cycle, the energy distribution shows minor differences. These are probably due to the modifications made to the algorithm to include the SOC strategy.

Other reference cycles, or the usage of a combination of cycles to calculate the Q matrix, would most likely yield other results. In addition, the choice of the discrete power vector S is of fundamental importance in the evaluation; if a low number of power levels (states) are included in S, all states with high probability in the reference cycle are likely to occur in the synthetic cycles after a comparably low number of steps. The example in this paper used an S vector of [-100:1:100]% of rated peak power, resulting in a 201x201 sized Q matrix. This fact will in turn require the cycle length to be in the same range as the number of elements in Q ($\approx$10000) to allow the cycle to span over the complete range of states.

In addition to optimising the cycle generation process for good correspondence to the reference cycle in terms of power distribution and energy distribution, the SOC changes must be taken into considerations. Nevertheless, the presented method has shown promising results and may be used for simplifying the set-up of battery tests, the evaluation of load cycles and to combine several reference cycles into one test cycle.

4.3 Synthetic Cycle used in Cycle life Tests, *Cycle B*

A new synthetic cycle, *Cycle B*, with similar capacity throughput, current distribution, length and RMS-current as the reference load cycle was extracted and tested in parallel with the reference profile *Cycle A*. The selected cycle is presented and compared to the original cycle in Figure 4.9 and Figure 4.8.
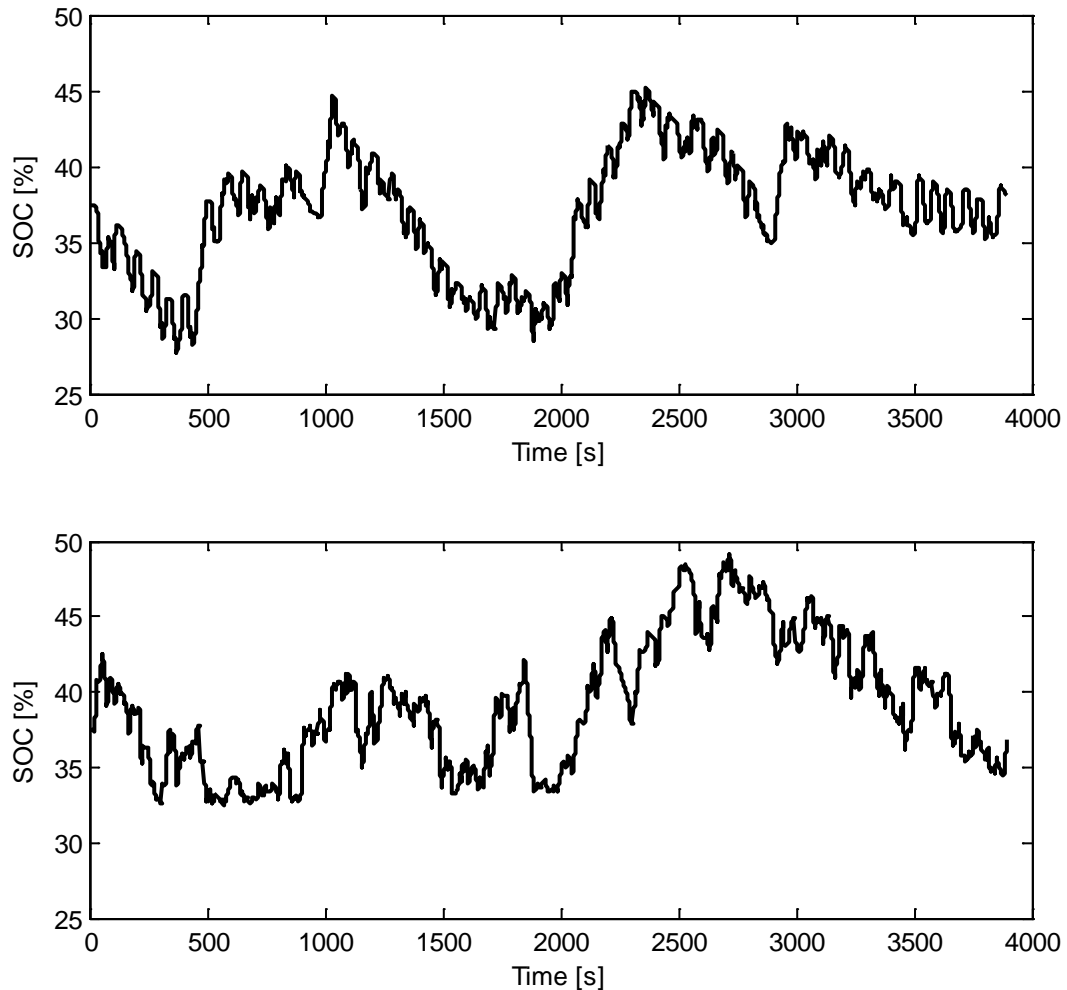
Figure 4.8   Comparison of SOC range for *Cycle A* and *Cycle B*, excluding SOC adjustment.

The SOC range presented in Figure 4.8 is similar between the two cycles, confirming that the SOC strategy is sufficiently accurate, but the since *Cycle B* is based on the stochastic model, the actual SOC variation is significantly different.
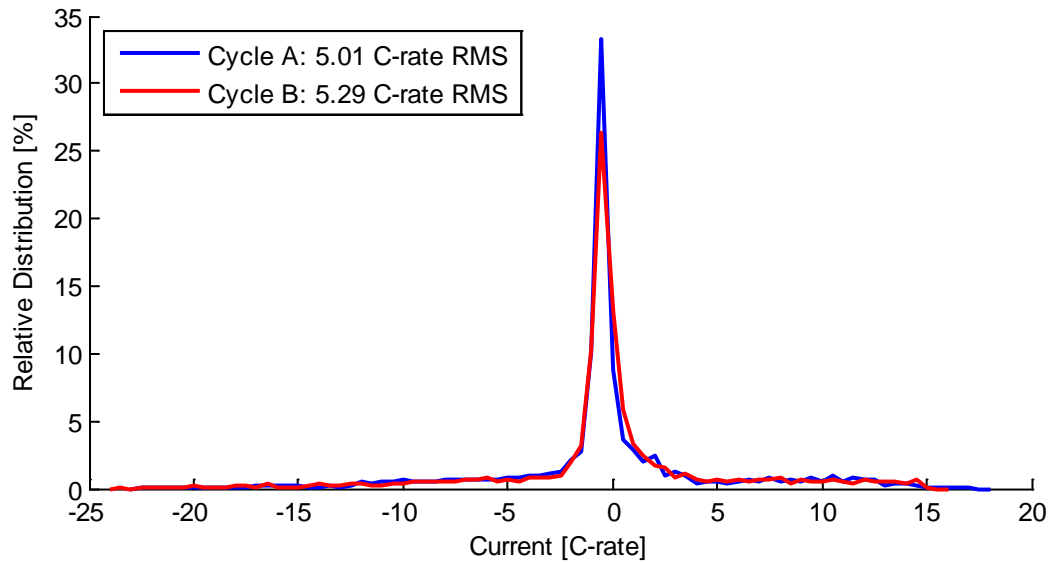
Figure 4.9   Current distribution comparison between reference *Cycle A* and synthetic *Cycle B*.

As can be seen Figure 4.9, the current distribution is similar for the two cycles, although there is a difference in RMS current. A summary of the cycle properties is given in Table 7 below.

Table 7   Comparison between reference *Cycle A* and synthetic *Cycle B*.

	Logged Cycle	Reference *Cycle A*	Synthetic *Cycle B*
Average SOC [%]	49.7	38.5	41.9
Minimum SOC [%]	37.5	22.6	32.5
Maximum SOC [%]	60.2	50.0	54.0
RMS Current [C-rate]	6.86	5.01	5.29
Average Current [C-rate]	4.17	2.82	3.00
Total Capacity Throughput [C-rate]	4.52	4.05	4.10
Peak Charge Current [C-rate]	23.9	17.3	15.1
Peak Discharge Current [C-rate]	28.2	22.3	23.2

Note that the resulting cycle is a compromise between similarities in SOC range, capacity throughput and RMS current. One consequence of this compromise is that the synthetic *Cycle B* is slightly more aggressive in terms of RMS current than the reference profile *Cycle A* although the peak current is lower and the capacity throughput is similar.

4.4 Constant Current Cycle – wide SOC-range, *Cycle C*

Often, a simple charge-discharge cycle with constant current rate is used to characterize ageing of batteries. The SOC range in this kind of test is usually wide, 80-100%, which has a profound effect on ageing. To compare such cycle with the ageing of HEV cycles, a simple charge/discharge cycle between 5% and 95% SOC, *Cycle C*, was set-up and tested at two different temperatures. The current rate was selected to give approximately the same capacity throughput per time unit as the reference profile. However, since the battery will be cycled over a wide SOC range no specific SOC adjustment at low current is needed. Consequently, the mean current over a complete cycle will be slightly larger than for the reference case or the synthetic cycle. The SOC profile for Cycle C is presented in Figure 4.10, displaying the simple cycle consisting of a constant current discharge step immediately followed by a constant current / constant voltage charge step.
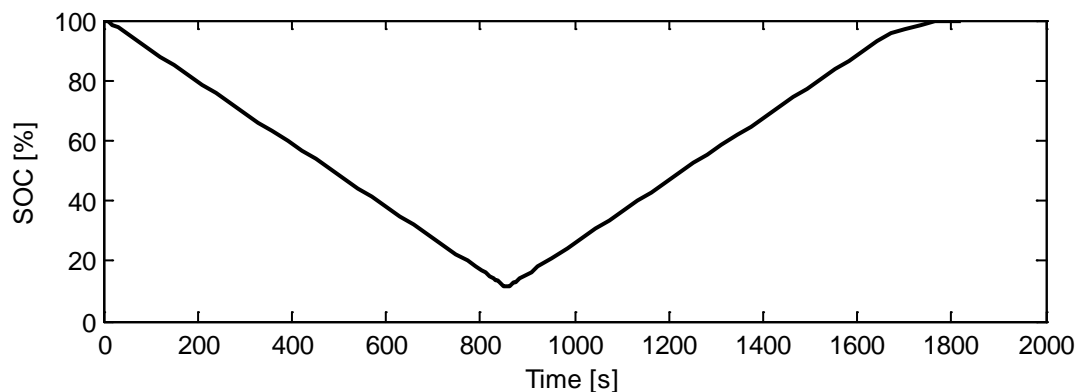
Figure 4.10   SOC profile for constant current *Cycle C* with a wide SOC range.

4.5 Constant Current Cycle – narrow SOC-range, *Cycle D*

Based on the assumption that the ageing effect of the wide SOC range would dominate using *Cycle C*, another test cycle, *Cycle D*, was set-up with a narrow SOC range matching that of the reference *Cycle A* (approximately 30-47%). Such cycle, with average current and SOC range close to that of the reference HEV cycle was set-up and tested. First and foremost test result from this cycle life test is believed to highlight the effect of cycle dynamics. *Cycle D* (see Figure 4.11) consists of a series of constant current charge and discharge steps, each resulting in a 17% change in SOC. This sequence is followed by a SOC adjustment procedure (see section 3.3) after approximately three hours to maintain the average SOC level constant despite

inaccuracies in current measurement. The constant current rate is selected to match the capacity throughput of the reference profile.
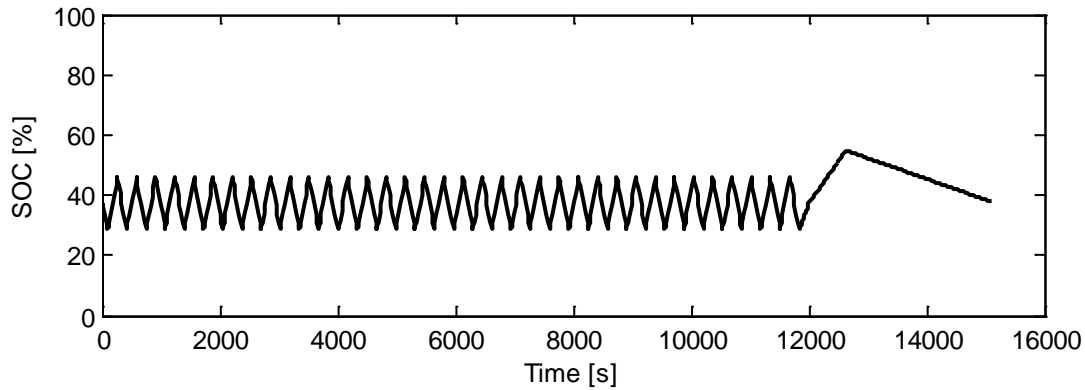

Figure 4.11   SOC profile for constant current *Cycle D*, 29-46% SOC, including SOC adjustment.

4.6 PHEV Cycle, *Cycle E*

Batteries used in PHEVs are cycled in a considerably different way than batteries used in HEVs. In addition to recuperation of kinetic energy, the battery is usually discharged over a couple of hours and then used in charge-sustaining mode, or re-charged under pre-defined charging conditions. Moreover, the average current is lower to allow for a longer period charge-depleting mode. Although this study focuses at battery load cycles for HEVs, a limited test of ageing during a PHEV cycle, *Cycle E*, was included. This load cycle is based directly on a vehicle simulation of a medium-sized city-bus. Starting with a fully charged battery the bus is running in charge-depleting mode for approximately one hour and then re-charged at standstill with constant current rate resulting in the SOC profile shown in Figure 4.12.
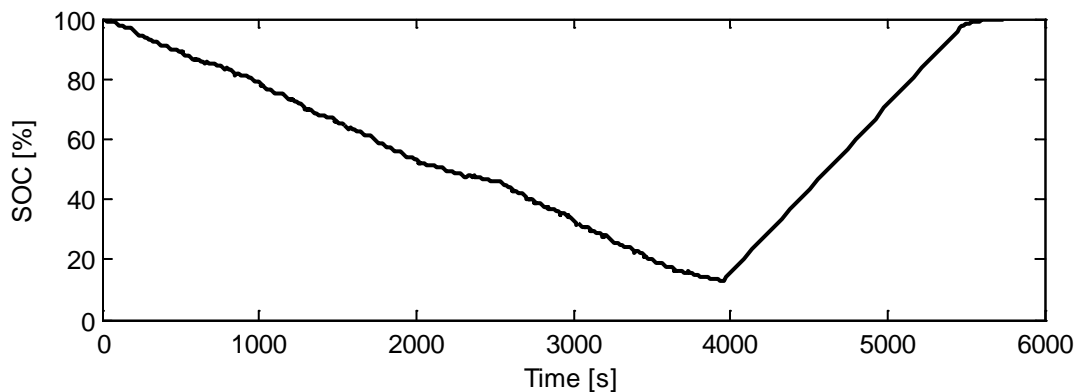
Figure 4.12   SOC profile for the PHEV cycle, *Cycle E*.

During the charge-depleting mode the battery acts as the main energy source in the vehicle but also an energy storage for recuperated brake energy. The cycle is scaled to limit the SOC region to approximately 10-100% in order to provide sufficient power efficiency and discharge power capability throughout the cycle.

4.7 Load Cycle Comparison

The key properties of the load cycles described in section 4.1 are given in
. Here, the HEV *Cycle A*, *Cycle B* and *Cycle D* all have the same characteristics in terms of SOC and capacity throughput while the RMS and the peak currents differ. In comparison, *Cycle C* has a comparable RMS and average power to the HEV-cycles but a significantly wider SOC-range. Lastly, the PHEV *Cycle E* and the constant current *Cycle C* have the same SOC-range but differences in RMS and average current. Consequently, these five cycles represents a wide variation of SOC, current range and load cycle complexity. The overall intention with this wide variation is to provide relevant cycle life test data for both HEVs and PHEVs, in turn to be used to quantify the most important ageing characteristics. A comparison between *Cycle A-E* is given in Table 8.

Table 8   Comparison between load cycles used in cycle life tests.

Cycle Property	Reference *Cycle A*	Synthetic *Cycle B*	Constant current *Cycle C*	Constant current *Cycle D*	PHEV *Cycle E*
Average SOC [%]	38.5	41.9	53.4	54.9	58.8
Minimum SOC [%]	22.6	32.5	11.4	28.8	13.0
Maximum SOC [%]	50.0	54.0	100	39.1	100
RMS Current [C-rate]	5.01	5.29	3.59	3.33	1.68
Average Current [C-rate]	2.82	3.00	3.49	3.04	1.22
Total Capacity throughput [C-rate]	4.05	4.1	1.77	4.24	2.00
Peak Charge Current [C-rate]	17.3	15.1	3.76	3.76	3.81
Peak Discharge Current [C-rate]	22.3	23.2	3.76	3.76	4.78

During the cycle life tests these cycles are controlled in a stepwise constant current mode with secondary limits set on voltage, temperature and SOC. Consequently, the load cycle properties in terms of voltage range are expected to vary as the cell impedance changes. Likewise, the average temperature distribution may change. Section 4.7.1 to 4.7.4 contain brief overviews of the measured load cycle properties after approximately half the total cycled time and observations of possible reasons to their different ageing factors.

4.7.1 Temperature Distribution

Although some of the cells were cycled at slightly elevated temperature, the temperature distribution is narrow for the complete test matrix as can be seen in Figure 4.13.
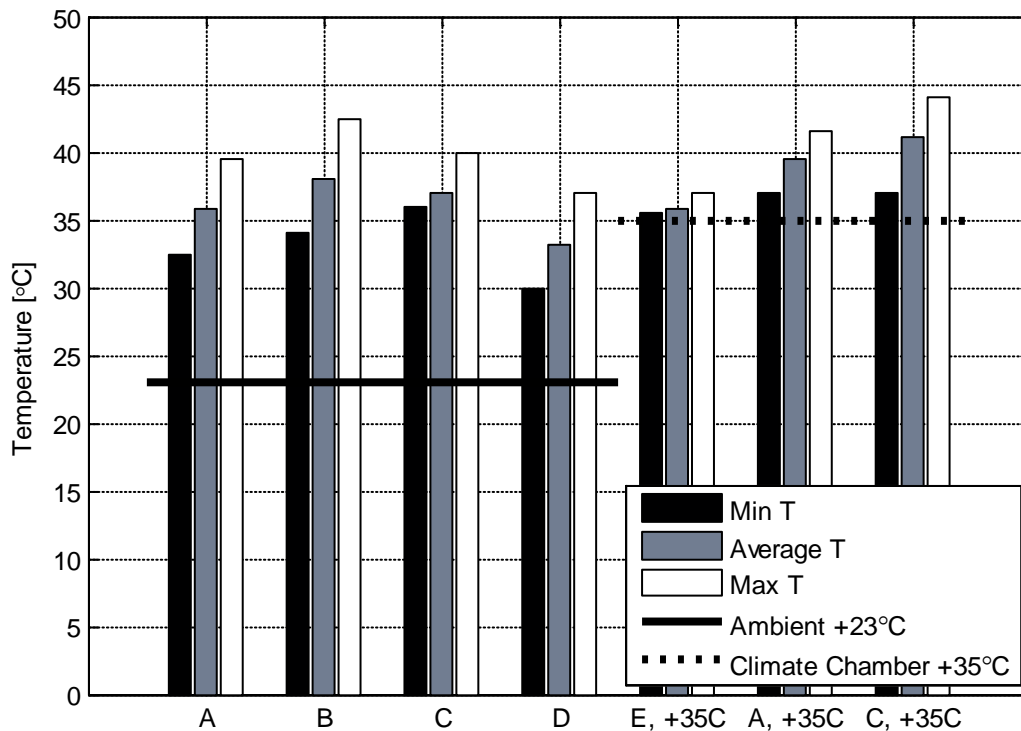

Figure 4.13   Temperature distribution for cells cycled with *Cycle A-E.*

This is partly due to the fact that the forced air convection inside the climate chamber is more effective in terms of cooling than the natural convection used for the cells in room temperature. Cells tested at *Cycle A* and *Cycle C* were cycled at both room temperature (+23 °C) and in a climate chamber kept at +35 °C (see Chapter 5 for details).

4.7.2 SOC Range

The SOC range during cycling is known to be a profoundly important factor when Li-ion batteries are cycled [6]. This is especially significant for graphite anodes, which upon intercalation and de-intercalation undergo a volume change that leads to mechanical stress, in turn leading to surface changes, degradation of particle inter-conductivity and in some cases loss of accessible anode material. Further background to this ageing mechanism is given in section 2.3.
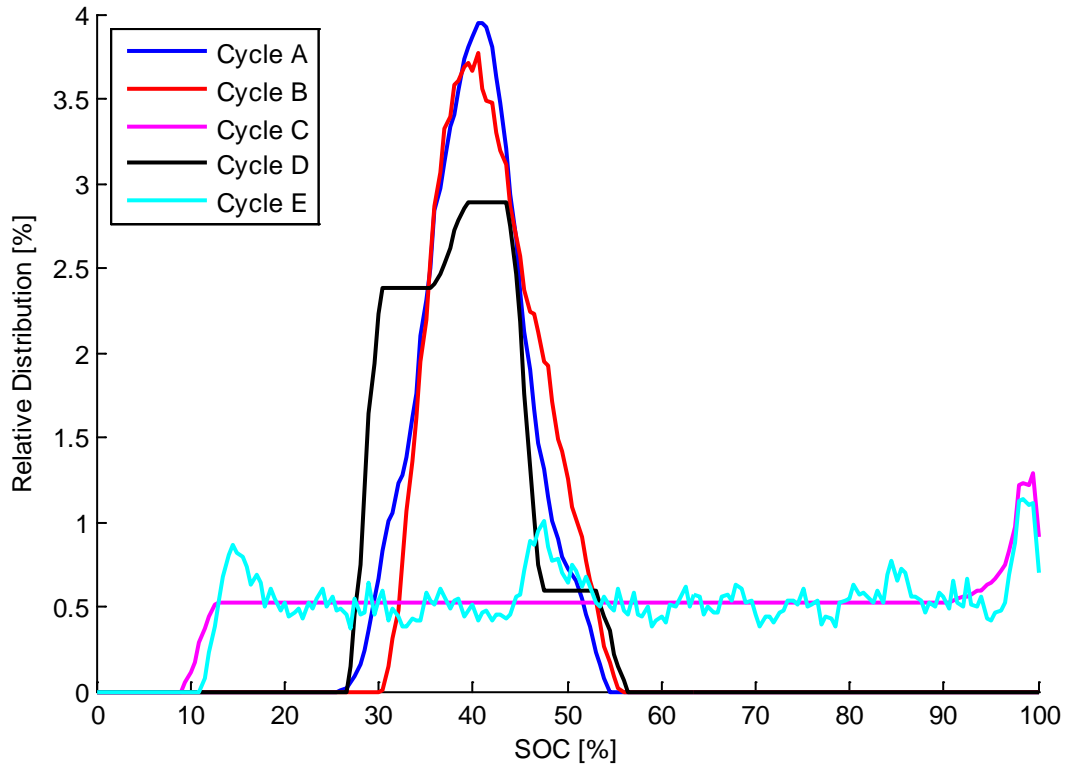
Figure 4.14   SOC distribution for cells cycled with *Cycle A-E.*

All tested cells are cycled in a narrow SOC range except those cycled with constant current *Cycle C* and PHEV *Cycle E* (see section 4.4, 4.6 and Table 8). A comparison between the SOC distributions of all tested load cycles is graphically presented in Figure 4.14. The three HEV cycles (*Cycle A*, *Cycle B* and *Cycle D*) are all kept approximately within the range 25-58% and the constant current cycles (*Cycle C* and *Cycle E*) has wide distribution of SOC between approximately 10-100%. Despite the similarities in SOC range between these two categories of load profiles they do undergo different ageing mechanisms according to the results presented in Chapter 6 and Chapter 7.

4.7.3 Current Distribution

The current distribution is notably different between the tested cycles; whereas the *Cycle A* and *Cycle B* have a wide distribution ranging between approximately -20…+20 C-rates, *Cycle C*, *Cycle D* and *Cycle E* are all between -4 and +4 C-rate as shown in Figure 4.15. In addition, there is a significant difference in RMS current, in turn leading to higher heat losses inside the cells and higher average temperature.
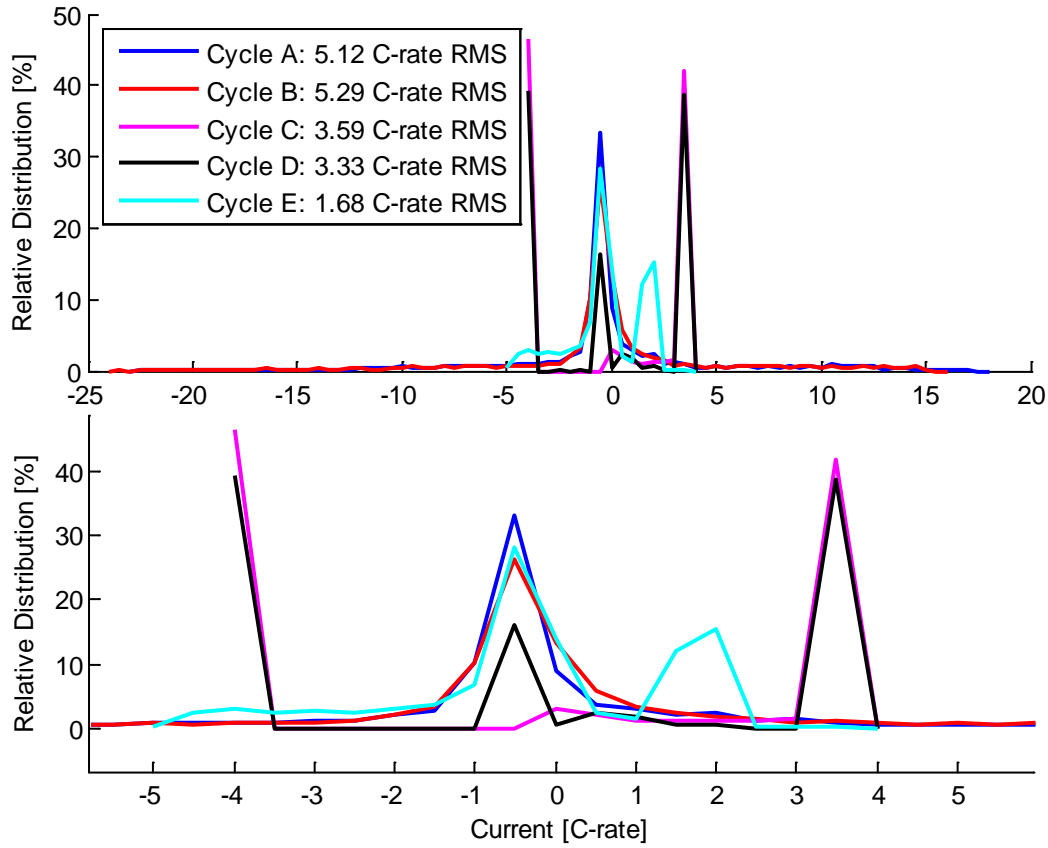
Figure 4.15   Current distribution for cells cycled with *Cycle A-E.*

The lower part of the brief comparison in Figure 4.15 between the distributions and the RMS currents highlights the difference in the low current area. Notably, the dynamic HEV cycles (*Cycle A* and *Cycle B*) all show a large relative distribution around low currents, including zero representing the rest periods.

4.7.4 Voltage Distribution

Two voltage distributions have been calculated for each cycle: the distribution of measured cell voltage and the voltage compensated for the voltage drop over the ohmic resistance and the charge transfer resistance according to (4.18) to (4.20) derived from the model presented in section 3.2.

$$U_{compensated} = U_{measured} - I_{measured}\left(R_{CT} + R_{Ohm}\right) \tag{4.18}$$

$$R_{CT} = f(T) \tag{4.19}$$

$$R_{Ohm} = f(T) \tag{4.20}$$

The ohmic and charge transfer resistance are calculated for the model presented in section 3.2. In order to include the temperature dependency, an impedance spectroscopy measurement was made at three cell temperatures: +23 °C, +32 °C and +41 °C, respectively.
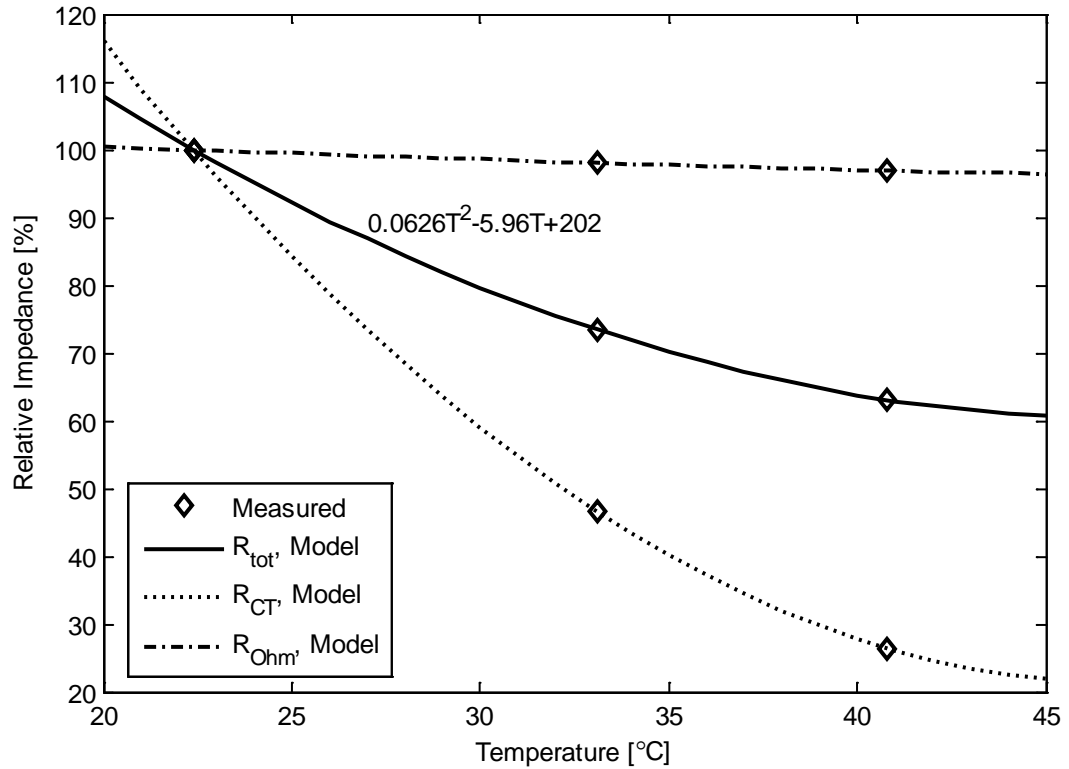
Figure 4.16   Impedance model temperature dependence.

Subsequently, the calculated values for charge transfer resistance and ohmic resistance were fitted to a second-order polynomial. Measured values and the calculated function of temperature are shown in Figure 4.16, where first and foremost the charge transfer resistance shows a strong temperature dependency.
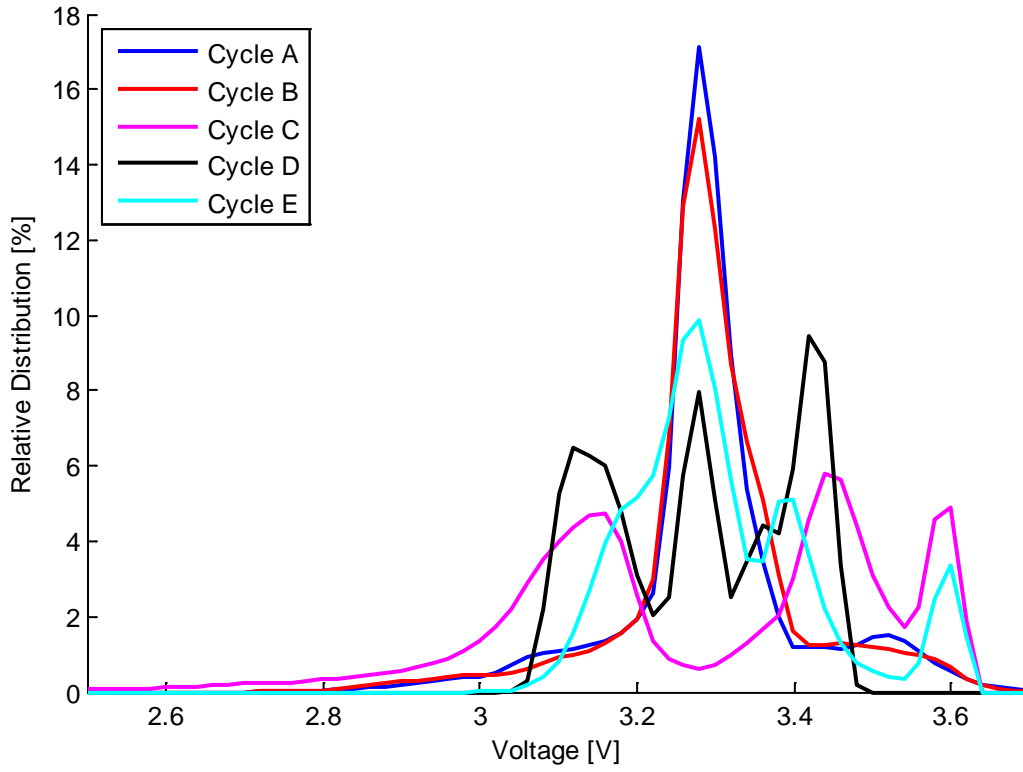
Figure 4.17   Voltage distribution for cells cycled with *Cycle A-E* not compensated for R_{CT} and R_{ohmic}.
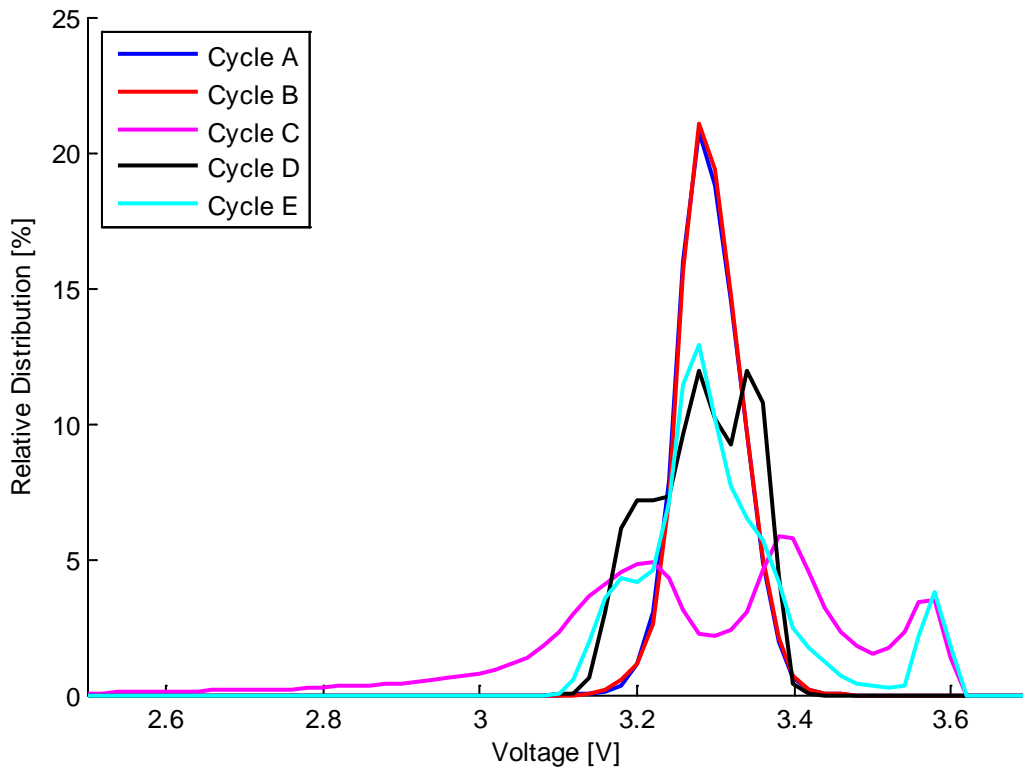
Figure 4.18   Voltage distribution for cells cycled with *Cycle A-E* compensated for R_{CT} and R_{ohmic}.

The voltage distribution shown in Figure 4.17 is not compensated for the voltage drop caused by the charge transfer and ohmic impedance. Consequently, the un-compensated voltage distribution is considerably wider than the distribution shown in Figure 4.18.

Generally, a wide voltage distribution is caused by either a wide SOC range or a wide current range. However, there are still differences between the voltage distributions of *Cycle A*, *Cycle B* and *Cycle D* despite their similarities in SOC range. This difference is most probably caused by the differences in cycle dynamics might be one explanation to the difference in ageing rate that is discussed further in Chapter 6 and Chapter 7.

Chapter 5   Experimental

Battery systems designed for use in HEVs often consists of hundreds to thousands of cells in parallel and / or series connection. Thus, the cells used for this purpose must have an extremely low variation in capacity, cycle life and performance. This is usually the case when cells from medium to high volume production are chosen. However, from a scientific point of view a test using only one cell for each test conditions is almost without value. A larger number of cells per test condition, and multiple variations of test conditions / load cycles quickly expand the test matrix beyond the scope of any laboratory. For the purpose of this research a compromise between accuracy, reliable results and test condition coverage had to be made. It was decided to use cells from high volume production, preferably from the same production batch, and to use at least two cells per test condition / cycle. It should be noted that for all the performed tests, no significant variation within each cell couple was observed.

5.1 Cell Specification & Test Matrix

During the first part of the investigation 3.6 Ah cylindrical cells were used, primarily to develop test methods and analysis tools. Although the results from these tests were confirmed during later test activities, no deep analysis of the results have been made or included in this thesis.

Figure 5.1   A123 ANR26650, 2.3 Ah.

A relatively extensive test process with commercial 2.3 Ah cylindrical cells (Figure 5.1 and Table 9) manufactured by A123 Systems was performed during 3-18 months' time.

Table 9   Cell specification of A132 ANR26650M1A

Component / property	Description / value
Cathode	LiFePO$_4$
Anode	Graphite
Electrolyte	LiPF$_6$ in unspecified solvent
Separator	Unspecified
Capacity	2.3 Ah
Nominal voltage	3.3 V
Maximum discharge current	Approximately 70 A continuous
Maximum charge current	Approximately 10 A continuous
Weight	70 g

A summary of the test matrix setup is presented in Table 10. Each test consists of two cells tested in parallel.

Table 10   Test Matrix, main cycle life test

Cycle	Description	Temperature	Cell Type	Capacity	No. of cells
A	Reference HEV cycle	+23 °C	A123 ANR26650	2.3 Ah	2
A	Reference HEV cycle	+35 °C	A123 ANR26650	2.3 Ah	2
B	Synthetic HEV cycle	+23 °C	A123 ANR26650	2.3 Ah	2
C	Constant current 100% ΔSOC	+23 °C	A123 ANR26650	2.3 Ah	2
C	Constant current 100% ΔSOC	+35 °C	A123 ANR26650	2.3 Ah	2
D	Constant current 17% ΔSOC	+23 °C	A123 ANR26650	2.3 Ah	2
E	PHEV Cycle	+35 °C	A123 ANR26650	2.3 Ah	2

All cell tests have been performed using a custom made cell holder (Figure 5.2) with four-wire connections and individual cell temperature monitoring.
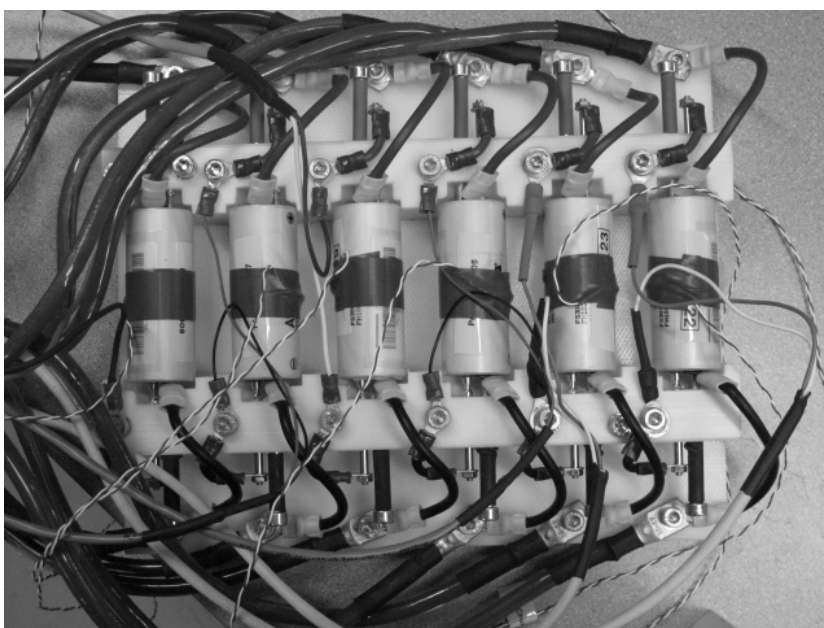
Figure 5.2   Custom made cell holder with four-wire connection

An additional support to the model development has been to test and characterise the individual battery electrodes by performing half-cell tests (Figure 5.3) as described in section 3.5.

Figure 5.3   A123ANR26650 cell and 3 mAh half-cell from UU.

The 3 mAh pouch-type half-cells were manufactured and supplied by UU made from electrode material (see Table 11) manufactured by Quallion LLC, similar to the full-cells supplied directly from Quallion LLC.

Table 11   Cell specification for half-cells

Component / property	Description / value
Cathode	Graphite or LiFePO$_4$
Anode	Li-metal foil
Electrolyte	Merck 1M LiPF$_6$, EC:DEC 1:1
Separator	Solopour
Capacity	3 mAh
Nominal voltage	0.2 V (graphite), 3.4 V (LiFePO$_4$)
Maximum discharge current	Approximately 3 mA
Maximum charge current	Approximately 3 mA
Weight	<1 g

A summary of the test matrix is given in Table 12. No cycle life tests were performed on these cells. Further details on the tests performed are given in section 7.4.

Table 12   Test Matrix, half-cell experiments

Cycle	Description	Temperature	Cell Type	Capacity	No. of cells
-	Constant current tests; C/25, C/10, C/5, C/2	+23 °C	Graphite // Li-metal	3 mAh	2
-	Constant current tests; C/25, C/10, C/5, C/2, C/1	+23 °C	LiFePO$_4$ // Li-metal	3 mAh	2

Furthermore, tests using prototype cells manufactured by Quallion LLC with and without a lithium-titanate reference electrode were initiated. These cells are also tested by other cluster partners, enabling a cross-comparison between material studies at UU and small-cell tests at KTH. The aim with these cell tests is primarily to develop test methods and analysis tools in the continuation of this investigation, thus the test results are not covered in this thesis.

5.2 Test Equipment

A programmable multichannel battery test equipment from MACCOR [78] was used for all cycle life tests (Figure 5.4):

Maccor Series S4000

Current Range:	-60…+60 A
Voltage Range:	0...5 V
Voltage Accuracy:	0.01% + 1 digit
Current Accuracy:	0.02% + 1 digit
Temperature Accuracy:	$\pm 0.5\,°C$
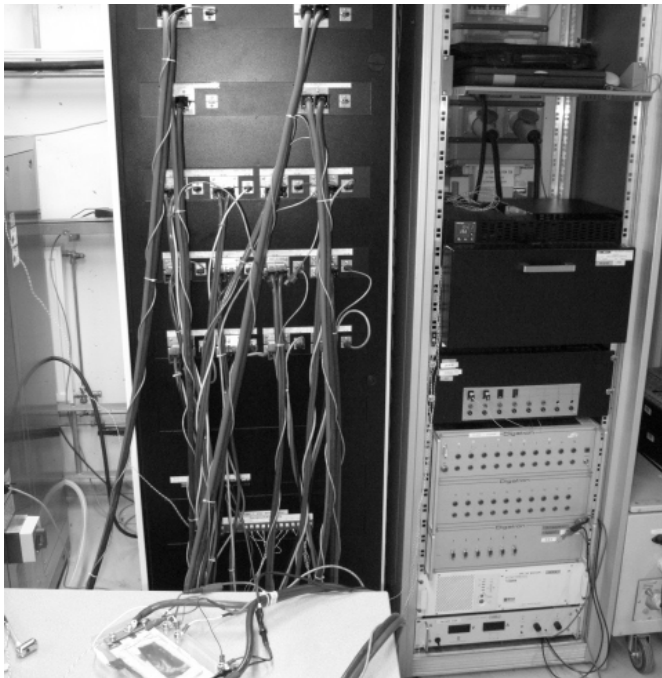
Figure 5.4   Maccor Series 4000 battery test equipment.

Half-cell experiments and impedance spectroscopy were performed using a programmable potentiostat / impedance spectrometer from GAMRY [79] (Figure 5.5):

Figure 5.5   GAMRY Reference 3000 potentiostat [79].

<u>GAMRY Reference 3000</u>

Current Range:	-3…+3 A
Voltage Range:	0...5 V
Voltage Accuracy:	± 1 mV ±0.3% of reading
Current Accuracy:	±0.3% range ± 10 pA
Current Ranges:	11 (300 pA-3 A)
Impedance Range:	0.1 mOhm-1 TOhm
Impedance Accuracy:	see Figure 5.6
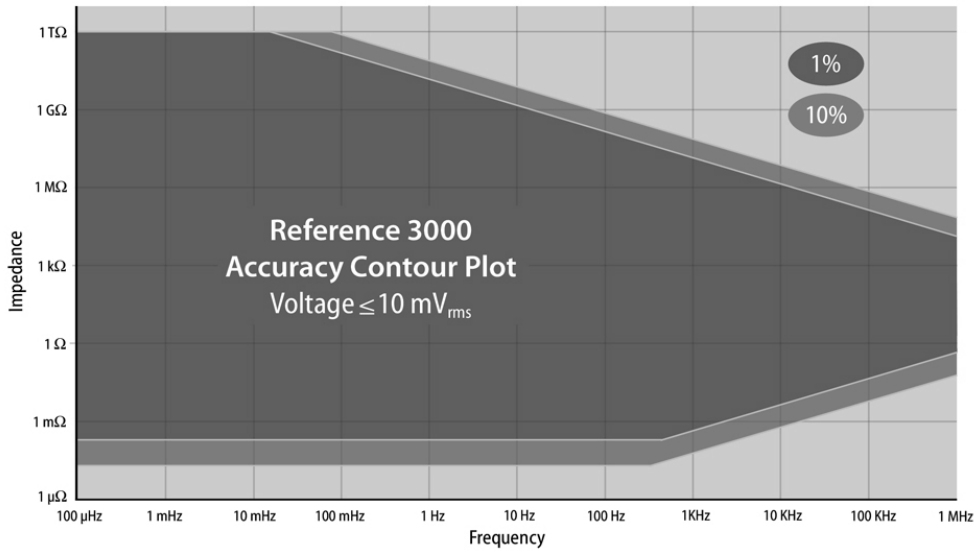
Figure 5.6   Accuracy for GAMRY Reference 3000 [79].

A small programmable climate chamber from MACCOR [80] was used to control the temperature of cells cycled at +35 °C ambient temperature

MACCOR Climate Chamber

Range: ambient…+100 °C

Temperature Uniformity ±0.5 °C

Temperature Accuracy ±0.5 °C

Figure 5.7   Maccor climate chamber with cell fixture.

Chapter 6   Cycle Life Test Results

Indeed, there are numerous ways to characterise ageing. Several different methods has been utilised in this study to highlight the main ageing effects on battery performance. In particular, methods have been selected that stress the differences between ageing with different load cycles. Starting from an application point of view, the main observable ageing effects such as capacity fade and power fade was analysed, followed by a calculation of key parameters linked to electrochemical properties like impedance, changes in material transport and possible causes. Specifically, possible methods to evaluate the ageing mechanisms are presented. These methods include Incremental Capacity Analysis (ICA), Differential Voltage Analysis (DVA), EIS and a comparison to simulated ageing using half-cell data. Most of these methods have been presented previously in literature [81], [82]. However, this thesis presents a comparison and evaluation of different methods when applied to cells being cycled at complex load cycles (see Chapter 4). Also, the combined result of these methods is believed to provide a better view of the ageing results and inputs to a correlation to the performance degradation measures.

This chapter summarises the cell ageing test results from an application point of view; capacity fade, power fade, increase in DC impedance and loss of efficiency.

6.1 Capacity Fade

All tested cells experience a significant capacity fade during cycling. Yet, the rate of the capacity fade differs significantly between different load cycles (*Cycle A-Cycle E*) and test conditions. In Figure 6.1 the capacity in per cent of the initial capacity is presented for all cells in the main cycle life test (Table 10). Here, the measured 1 C-rate capacity for all cells is presented together with a three-point symmetric moving average filter for each cell pair *vs.* the total capacity throughput expressed in C-rates (3.3). According to this definition, one capacity throughput corresponds to one full discharge and one full charge cycle.
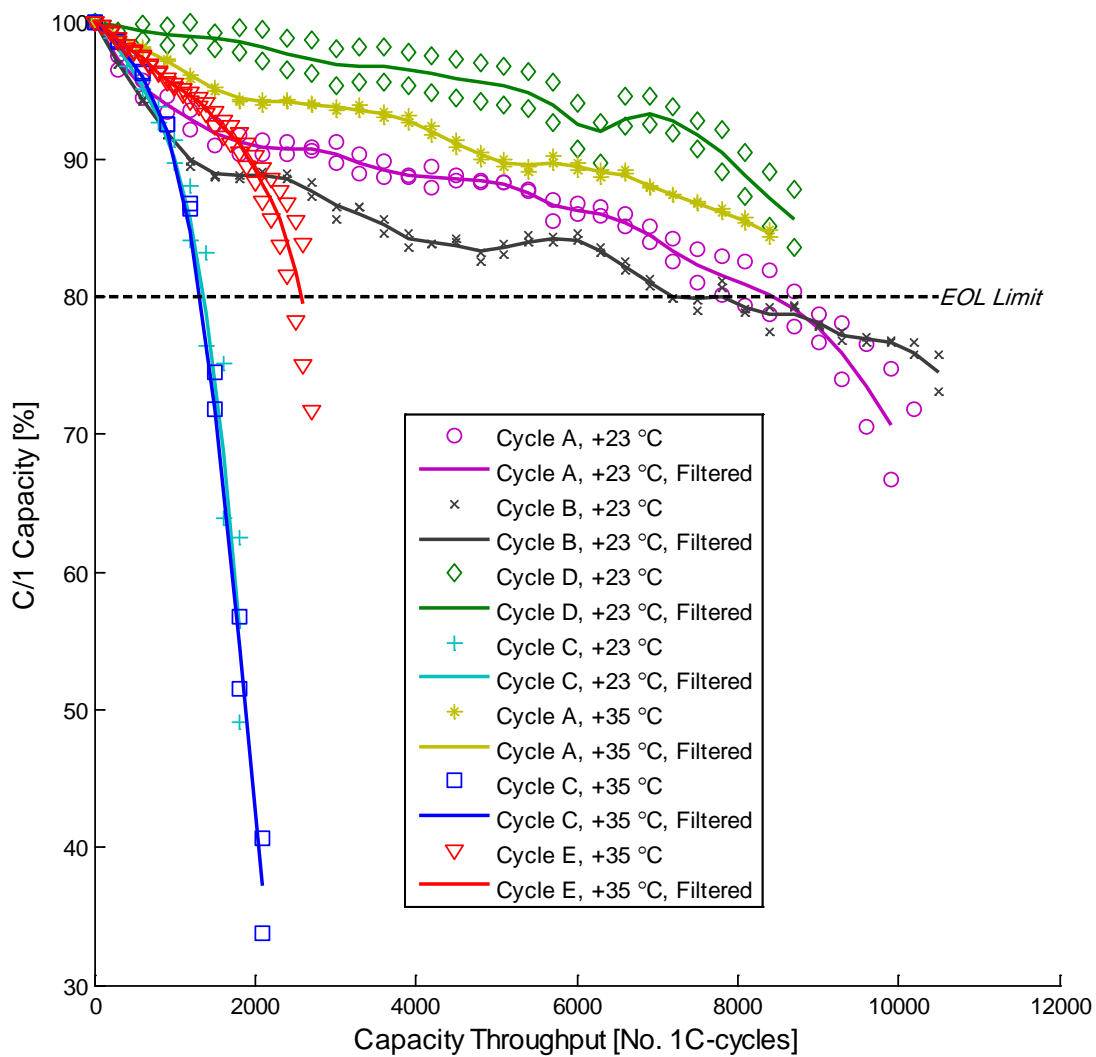
Figure 6.1   Capacity fade *vs.* capacity throughput for cells cycled with *Cycle A-E.*

All HEV-type cycles (*Cycle A*, *Cycle B* and *Cycle D*) show an overall moderate ageing rate with three phases:

Phase 1: Relatively fast initial drop in capacity, probably caused by SEI growth and stabilisation.

Phase 2: Slow and linear capacity loss

Phase 3: Accelerated loss of capacity near EOL

Cells cycled according *Cycle A* and *Cycle B* have reached EOL after approximately 10 000 cycles. Notably, the cells cycled according to *Cycle A* at +35 °C ambient temperature shows a slower ageing rate than those cycled at +23 °C ambient temperature.

The cells cycled over a wide SOC range (*Cycle C* and *Cycle E*) shows a profoundly different ageing pattern; the capacity loss is fast and they hardly experience the Phase 2 region. Instead, the initial capacity fade rate monotonically increases over time until EOL.

In a real application the cycle life corresponds to approximately one year for a heavy-duty HEV and nine months for a heavy-duty PHEV:

Assumptions

Number of HEV cycles per day: 13 ≈ 16 hours

Number of PHEV cycles per day: 8 ≈ 16 hours

Days in operation per year: 350

$$t_{\text{cycle life, HEV}} = \frac{N_{\text{cycles}}}{N_{\text{cycles per day}} \cdot N_{\text{days per year}}} \approx \frac{5000}{13 \cdot 350} \approx 1.1 \text{ year} \tag{6.1}$$

$$t_{\text{cycle life, PHEV}} = \frac{N_{\text{cycles}}}{N_{\text{cycles per day}} \cdot N_{\text{days per year}}} \approx \frac{2000}{8 \cdot 350} \approx 0.7 \text{ year} \tag{6.2}$$

The assumptions above are based on a comparably severe combination of operating conditions. Also, the tested 2.3 Ah cells are not designed specifically for heavy-duty HEVs. Hence, significantly longer cycle life is expected for commercial battery systems in HEVs and PHEVs.

6.2 Power Fade

The power fade may be regarded as a good indicator for the practical performance of a battery in an HEV-application. However, it is less suitable as a qualifying parameter to use when analysing the ageing mechanism since it is depending on several factors such as impedance, self-heating, permitted voltage window, capacity (SOC range) and cell-to-cell imbalance in a battery pack. In Figure 6.2 and Figure 6.3 the charge and discharge power is presented as a function of the capacity throughput.
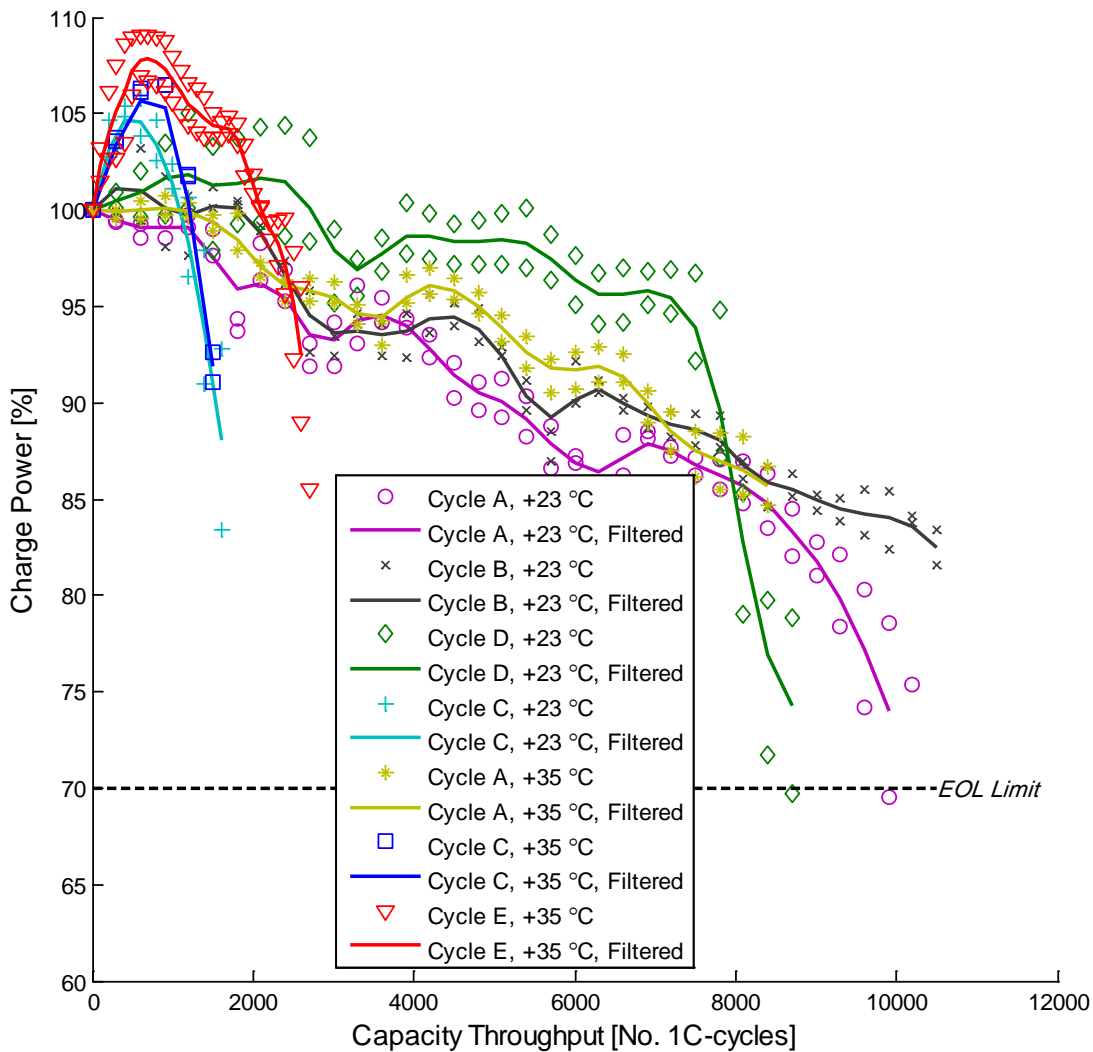
Figure 6.2   Charge power *vs.* capacity throughput for cells cycled with *Cycle A-E.*

Notably, the discharge power fade is significantly lower than the charge power fade, possibly indicating an asymmetrical material transport limitation in the cell during ageing. In a real HEV application this may lead to a decrease in recuperated energy, in turn leading to an increase in fuel consumption.
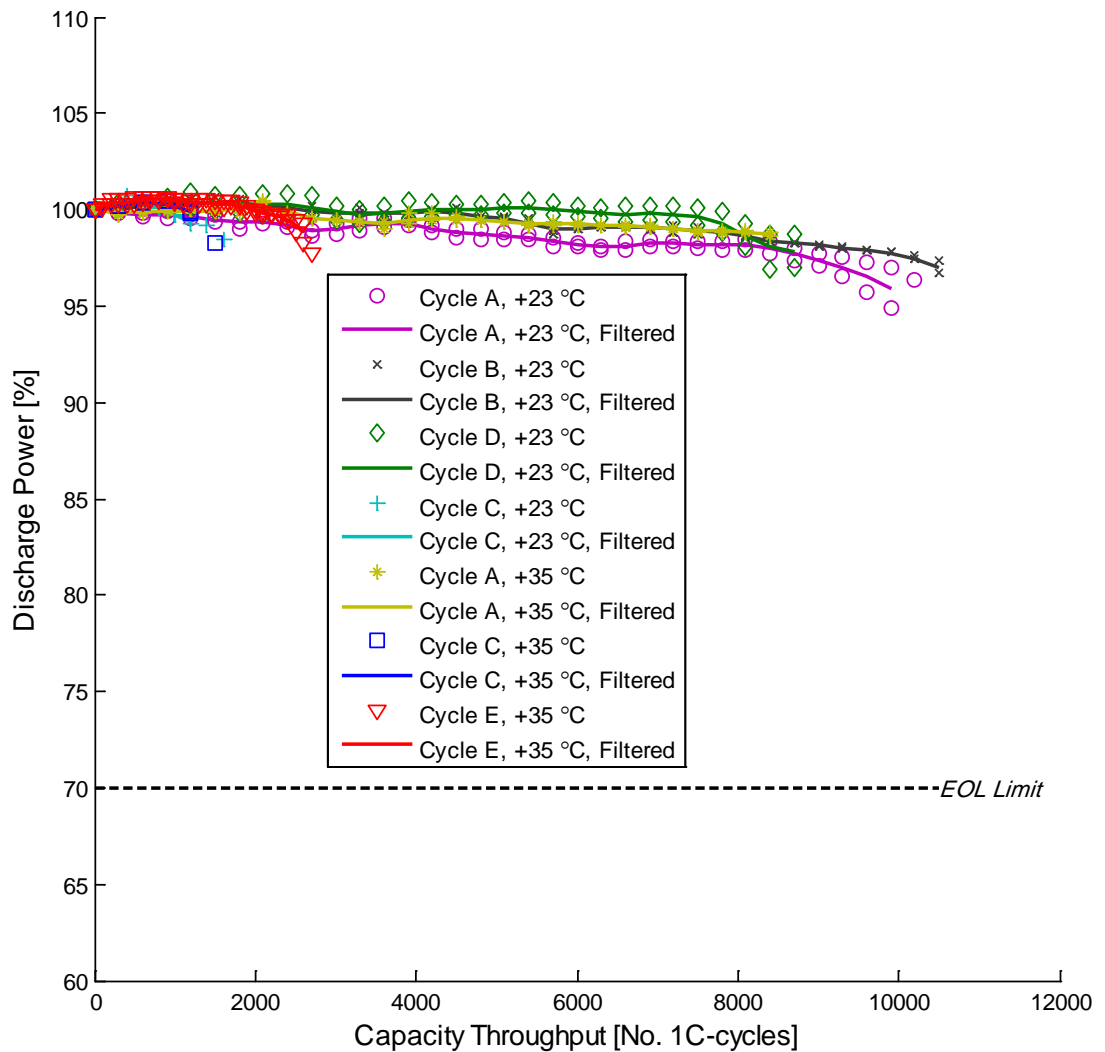
Figure 6.3   Discharge power *vs.* capacity throughput for cells cycled with *Cycle A-E.*

Another aspect that is important to point out is that a rise in charge impedance leads to an increase in charge power as long as the upper voltage limit is not reached. On the other hand, such an increase in power is irrelevant since it also leads to a significant reduction in power efficiency. Also, it should be noted that all cells cycled with constant charging current over a large SOC range experience an initial and rapid increase in charge power. This is a profoundly different ageing pattern than that of the cells cycled according to HEV cycles.

6.3 Impedance Growth

Similarly to the fade in charge and discharge power, the impedance rise is more pronounced for charge pulses than for discharge pulses (Figure 6.4 and Figure 6.5, respectively).
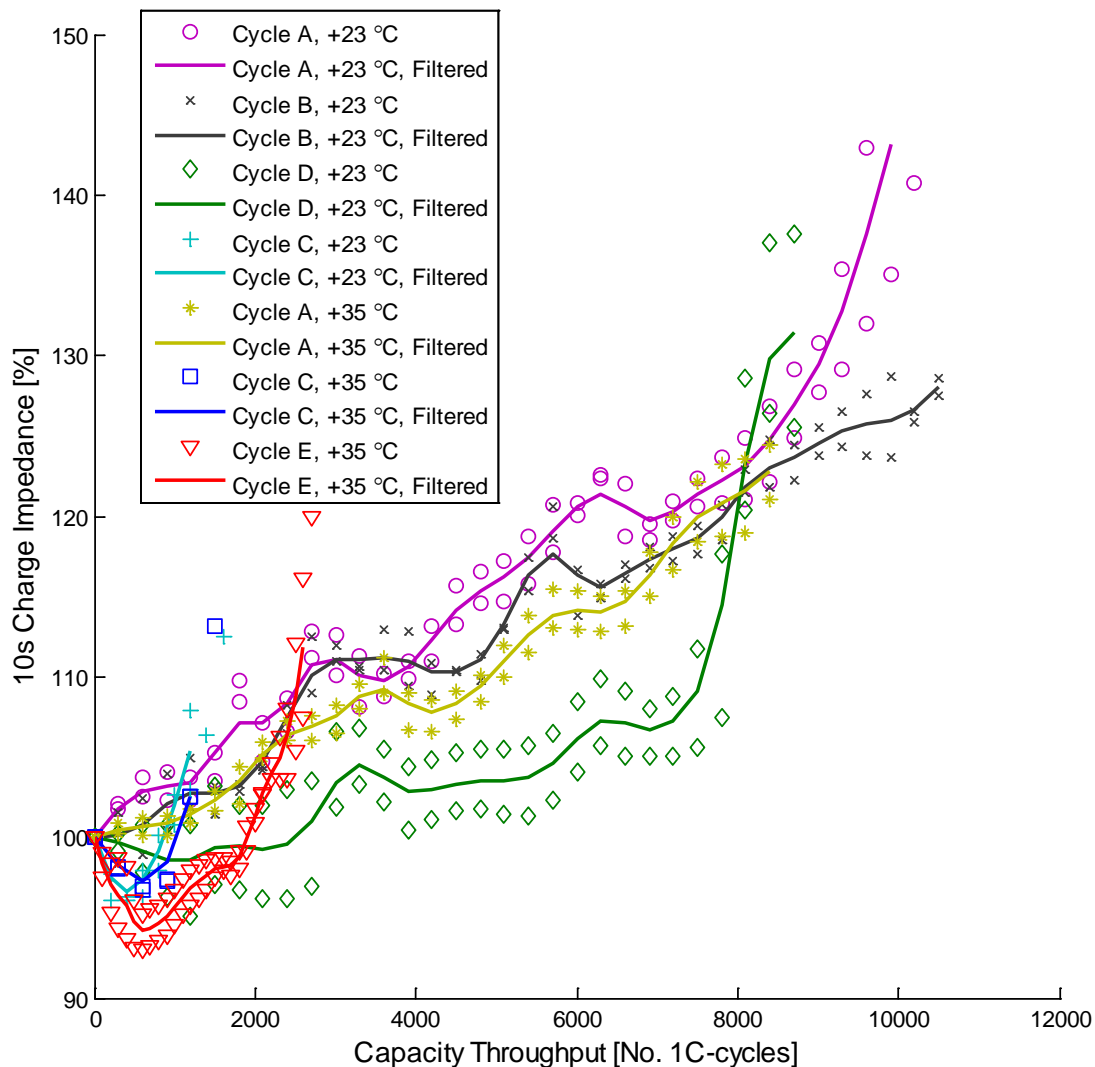
Figure 6.4   Charge 10 s DC impedance *vs.* capacity throughput for cells cycled with *Cycle A-E*.

Furthermore, during the first phase of ageing up to approximately 1000 capacity throughputs all cells cycled at a wide SOC range experience a decrease in impedance that is correlated to the initial increase in power. None of the cells cycled with a narrow SOC range (*Cycle A*, *Cycle B* and *Cycle D*) shows the same trend in initial impedance decrease, which may indicate that a different ageing mechanism is dominating when a wide SOC range is used.
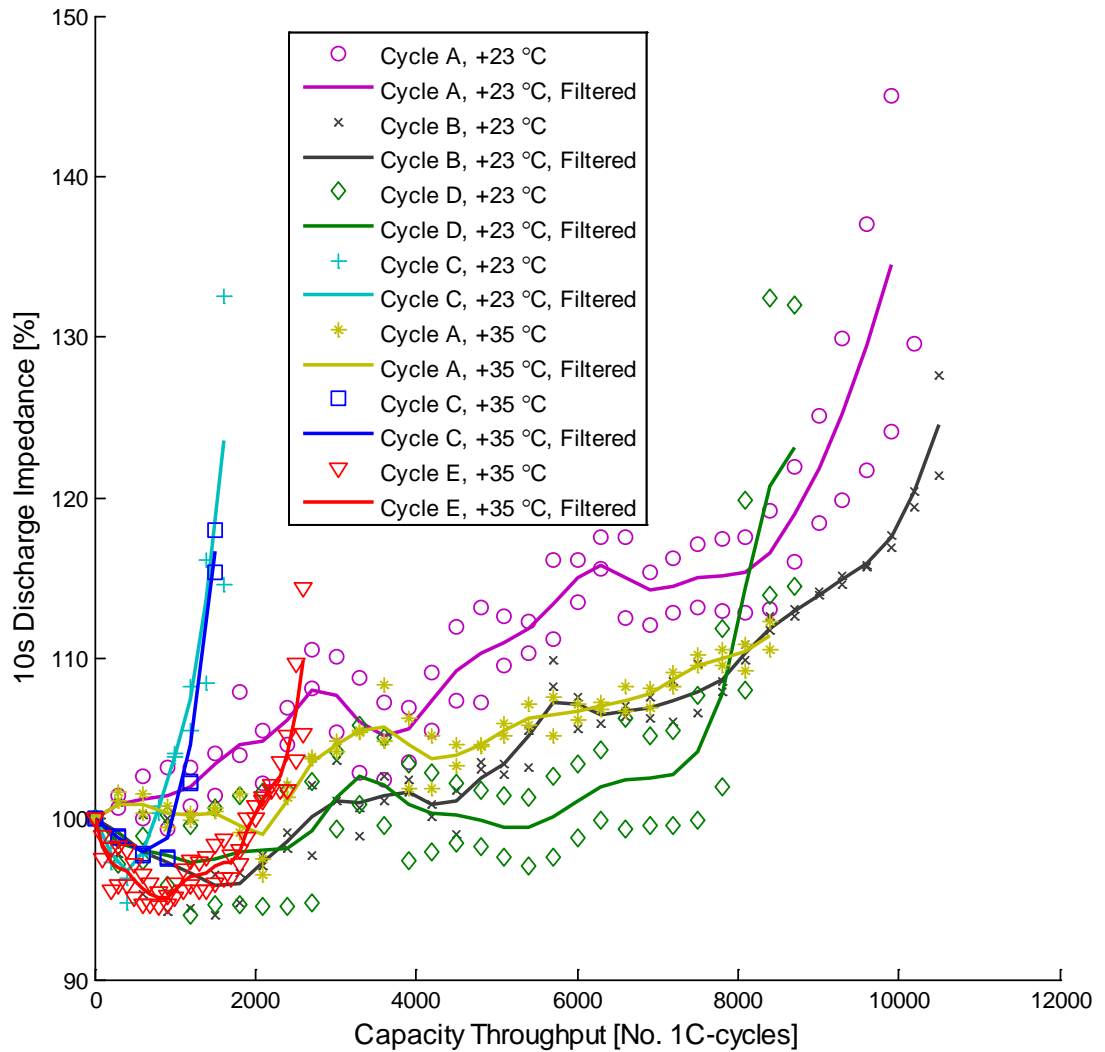
Figure 6.5   Discharge 10 s DC impedance *vs.* capacity throughput for cells cycled with *Cycle A-E.*

Another similarity to the capacity fade is the appearance of an accelerated ageing pattern close to EOL. For an HEV application this means that both the usable capacity of the cell and the available power decreases significantly over time, thus limiting the performance of the energy storage system, in turn affecting the overall fuel efficiency.

6.4 Power Efficiency at Low Power

Although the capacity, the maximum power and DC impedance are significantly deteriorated during cycling, the power efficiency calculated from the dynamic response tests (see section 3.1.2) stays surprisingly stable throughout the cycle life test (Figure 6.6).
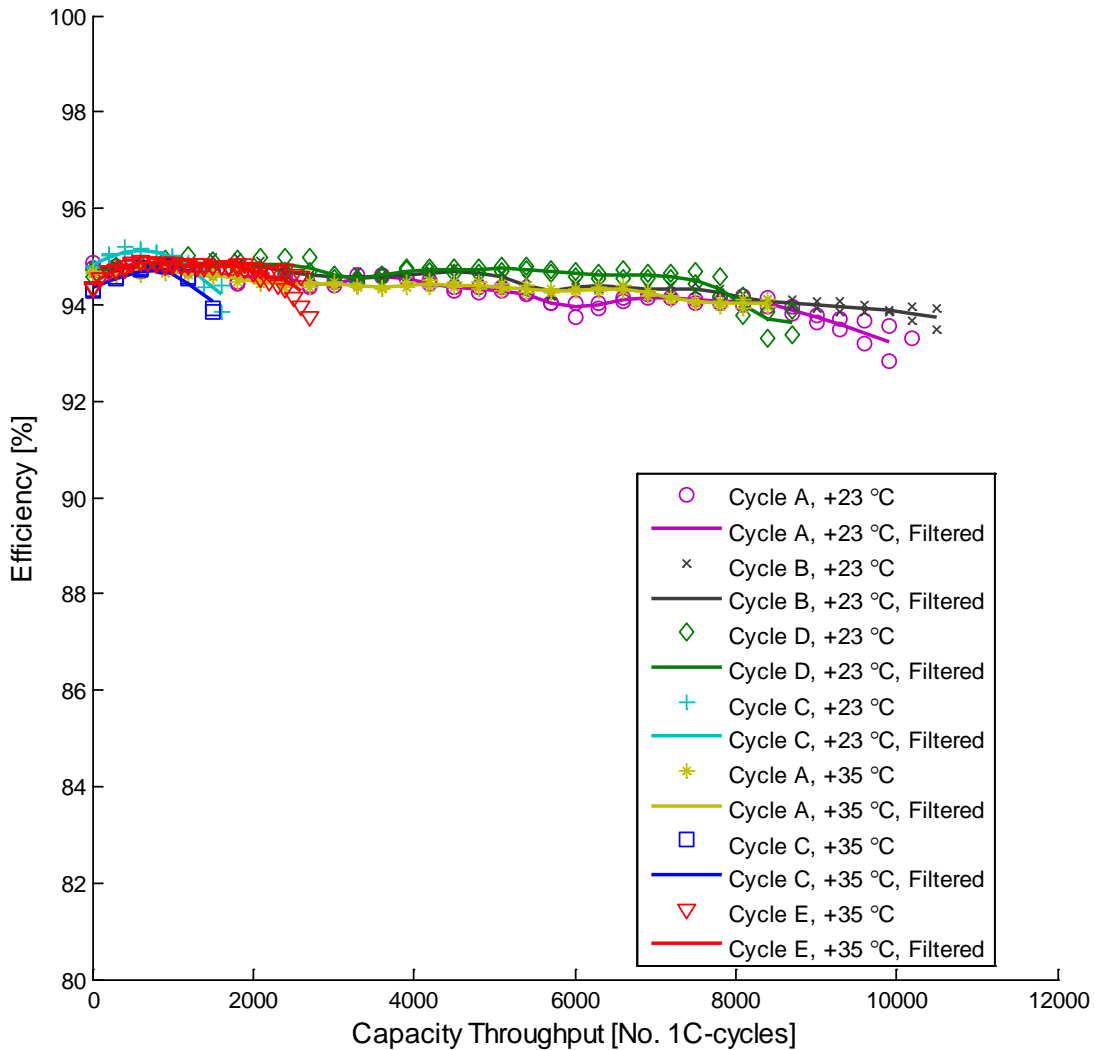
Figure 6.6   Power efficiency *vs.* capacity throughput from dynamic response test for cells cycled with *Cycle A-E.*

The stable power efficiency indicates that at low to medium power, the cell will be able to provide sufficient performance in terms of power and efficiency throughout its lifetime. It should however be emphasised that this reasoning is strongly dependant on the definition of "low to medium power"; in this case 1-5 C-rate. Furthermore, the results are in line with the definition of instantaneous power efficiency (3.7-3.8) where an increase in total impedance yields a similar change in power efficiency.

6.5 Calendar Ageing

The effect of calendar ageing (see section 2.4.2) was not a part of the present work. However, all cells were manufactured at approximately the same date and the different cycle life tests were initiated at different dates. Hence, an overview of the effect of calendar ageing can be made using the test result from the first RPT for each cell. The measured capacity at 1 C-rate and the 10s DC impedance for discharge at 60% SOC (see section 3.1) is presented *vs.* storage time in Figure 6.7.
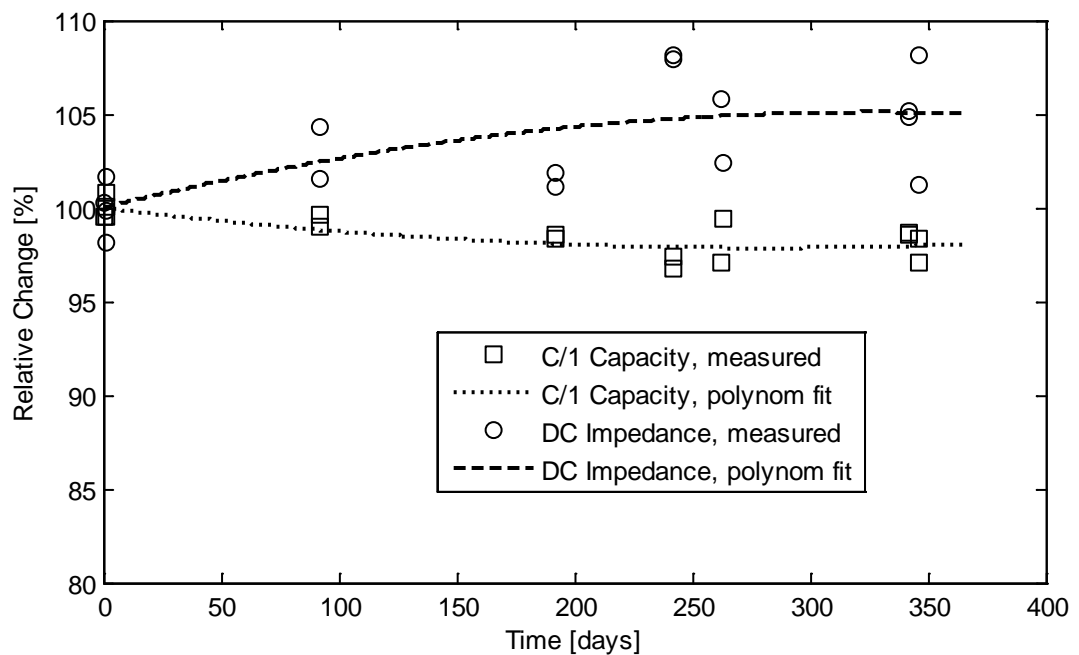
Figure 6.7   Capacity at 1 C-rate and 10s DC impedance for discharge at 60% SOC *vs.* storage time.

There is slight distribution of capacity and impedance within the cells characterised at each time period. Typically 1-2 cell tests were characterised at approximately the same time, yielding the five distinct groups seen in Figure 6.7. Also, the distribution of impedance is significantly larger than for capacity. Nevertheless, the differences are small compared to the trends observed during the cycle life tests (see section 6.1 and 6.3). The differences may also be dependent on the properties (accuracy) of the different channels of the battery test equipment.

Since all the ageing properties evaluated within the scope of this investigation are normalised to the respective initial property this is assumed to have a negligible effect on the analysis.

6.6 Summary

A brief analysis of the results can be summarised as follows:

- The synthetic cycle (*Cycle B*) is more detrimental than the reference cycle (*Cycle A*), during the first phase of ageing, but *Cycle A* results in an earlier EOL.

- A higher average temperature does not necessarily lead to a faster capacity fade in this case; there is no significant difference between the cell pairs cycled with *Cycle C* at +32 °C and +42 °C. More notably, the cells cycled at *Cycle A* at +35 °C shows a slower capacity fade than what is observed at +23 °C.

- When cycling at constant current, the SOC range has a profound effect on the capacity fade. Cells cycled with 17% ΔSOC (*Cycle D*) do not show a capacity fade rate that is comparable to those cycled with 95-100% ΔSOC (*Cycle C*).

- The capacity fade rate is neither constant nor monotonically increasing over time. All cells show a capacity fade rate that varies over time.

- The increase in charge impedance and the corresponding decrease in charge power are considerably higher than the corresponding figures for discharge, possibly leading to higher fuel consumption in an HEV. This may indicate an "asymmetric" ageing with respect to anode and cathode.

- The discharge power at high current rate and the efficiency at low to medium current rate stay relatively constant over time.

Chapter 7   Cell Ageing Analysis

Although battery ageing is often characterised using capacity fade and power fade as reviewed in section 2.2 and summarised in section 6.6, there are several other possible methods suitable for analysis and characterisation. This section presents an analysis based on a selection of methods used within the work covered by this thesis. Specifically, methods that can be used on commercial large cells to distinguish between different ageing mechanisms have been evaluated.

The purpose of this section is to evaluate different methods for evaluating and quantifying ageing mechanisms. This analysis may also provide input to how different properties of load cycles and operating conditions affect the observed change in cell performance during cycling.

7.1 Galvanostatic Voltage Profiles

Galvanostatic charge and discharge tests are probably one of the methods that most clearly show how the electrochemical properties of a Li-ion cell changes during ageing. Such tests at C/1 and C/4 current rate were included in the RPTs (see section 3.1). In good correlation to the overview in Chapter 6, these voltage profiles provide a qualitative view of both capacity fade and impedance increase. Voltage profiles measured at BOL and EOL for cells cycled according to *Cycle A-E* are shown in Figure 7.1 and Figure 7.2.
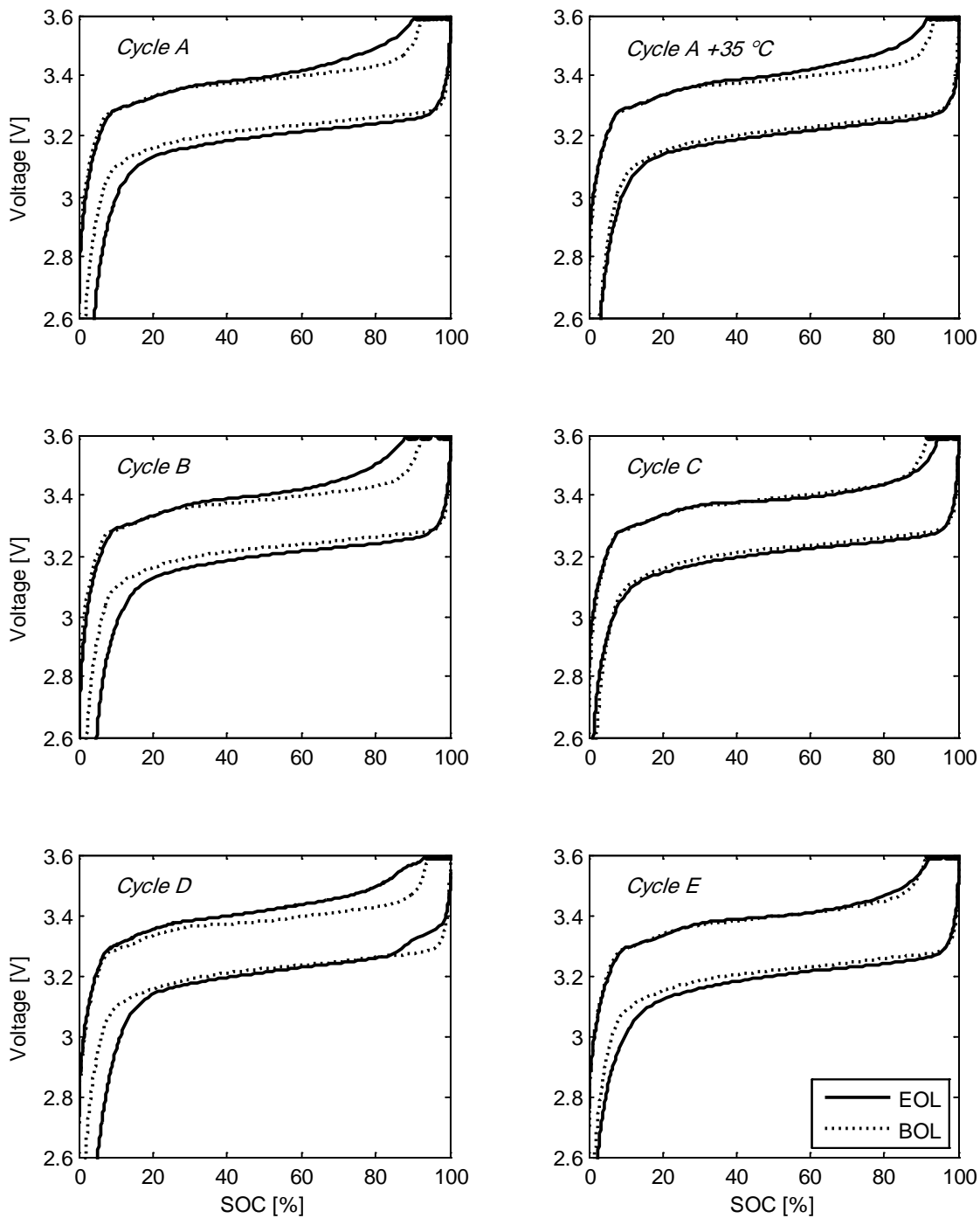
Figure 7.1   C/1 voltage profile *vs.* SOC for cells cycled with *Cycle A-E.*

Figure 7.1 shows the C/1 voltage profile as a function of cell SOC based on measured capacity. That is, the reference capacity used to calculate SOC changes over time to allow SOC=100% to correspond to a fully charged cell regardless of an observed decrease in capacity. For cells cycled with the HEV cycles *Cycle A* and *Cycle B* the impedance increase is more evident than for the PHEV cycles *Cycle C* and *Cycle E*. Here, the impedance increase for *Cycle A and Cycle B* causes a higher voltage drop, especially close to SOC=100% and SOC=0%, possibly indicating a slow migration of

Li-ions in the solid phase. Notably, the cells cycled with *Cycle A* at +35 °C does not show higher impedance growth than those cycled at +23 °C.
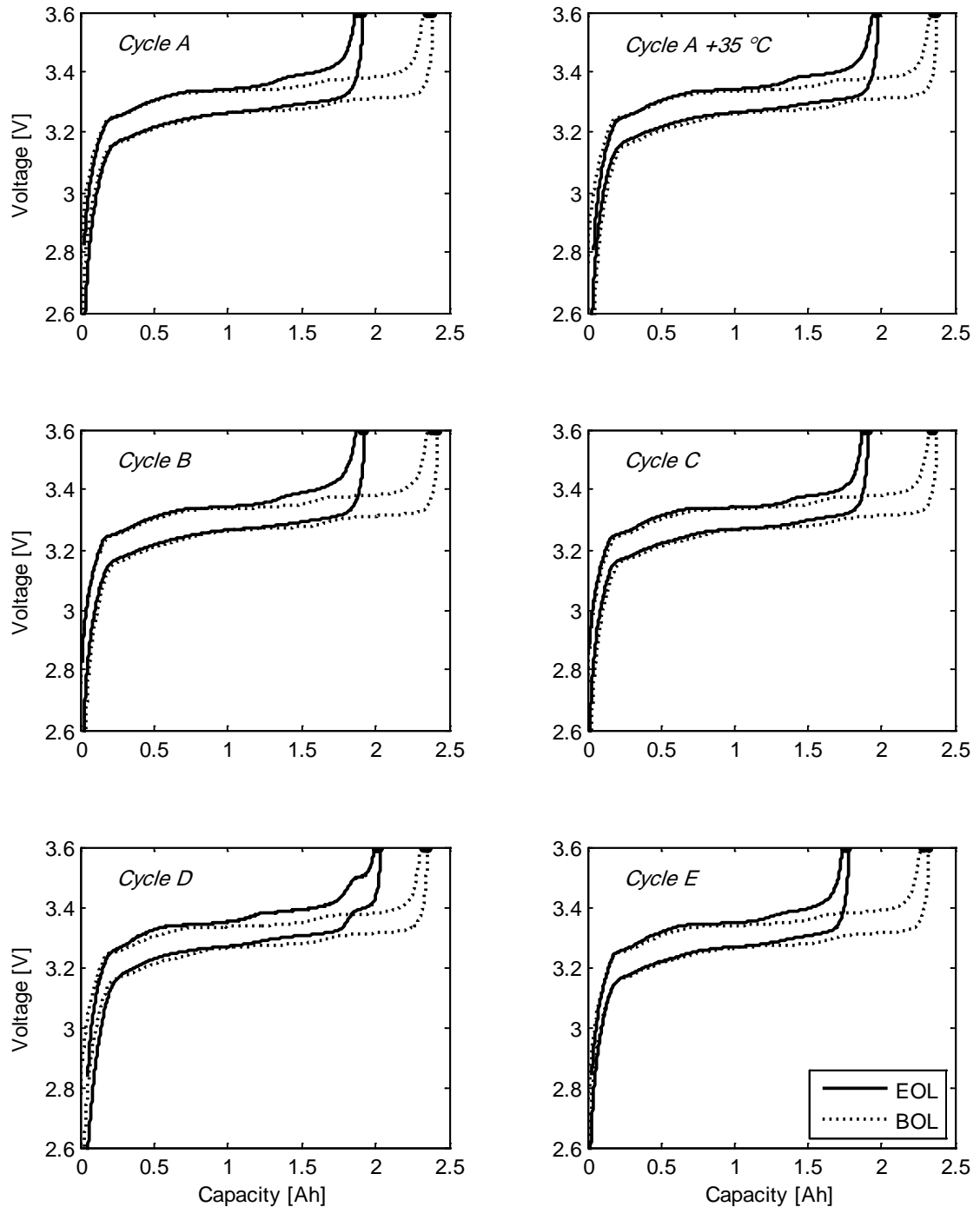
Figure 7.2   C/4 voltage profile *vs.* capacity for cells cycled with *Cycle A-E*.

An alternative to comparing voltage profiles vs. SOC is to use an absolute capacity scale. Figure 7.2 shows the voltage profile as a function of measured capacity at C/4 current rate, highlighting both the change in cell characteristics and the decrease in capacity; first and foremost the voltage plateau close to SOC=100% is significantly compressed for all cells, indicating that the cathode limits the charge before the anode is

fully charged. The absence of a notable difference in impedance increase at C/4 further supports the hypothesis that the large voltage drop close to SOC=0% and SOC=100% for the HEV cycles (Figure 7.1) is caused by slow mass transport rather than an overall loss of conductivity in electrodes or electrolyte.

The voltage profile of cells cycled according to the constant current *Cycle D* shows an abnormal voltage plateau at approximately SOC=90% as illustrated in Figure 7.2 and Figure 7.3. Also, the impedance increase is larger than what is observed for *Cycle A* and *Cycle B*.
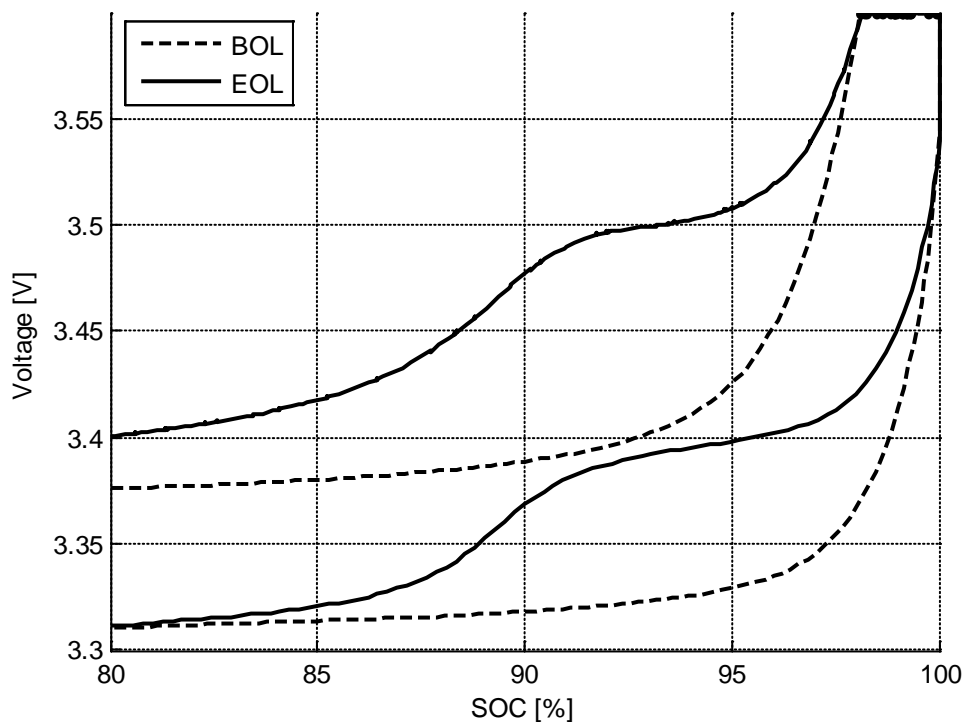
Figure 7.3   Detailed view of high-SOC C/4 voltage profile for cell cycled with *Cycle D*.

This new plateau is not related to any of the graphite stages (see section 7.2) and the cause has not been confirmed. However, it might be due to a reversible Li-plating on the anode since the new voltage plateau approximately corresponds to an anode potential of 0 V *vs.* Li/Li$^+$. This hypothesis is discussed further in the following sections.

7.2 Differential Voltage Analysis & Incremental Capacity Analysis

By using the galvanostatic voltage profiles at C/4 from the RPTs (described in section 3.1) it is possible to analyse and quantify the changes in electrochemical properties of the cell further. Both the ICA and the DVA have been proposed and used before [15], [81]-[85] and proved to serve as valuable tools.

In Figure 7.4 the different phases of graphite during intercalation/de-intercalation is presented as suggested by [86] together with a charge and discharge voltage profile measured on a Li//graphite half-cell (see section 7.3).
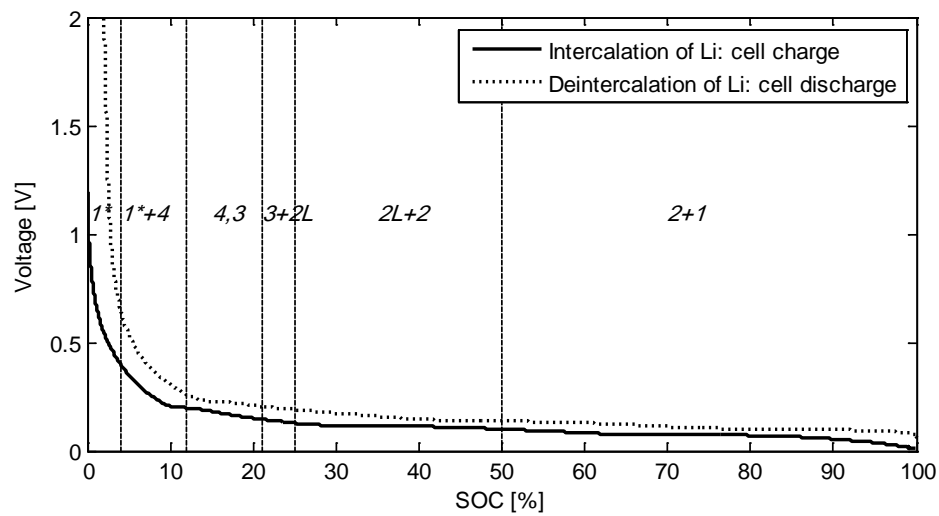
Figure 7.4   Phase diagram for Li-intercalation into graphite based on measured cell voltages at C/25 and [86].

The different plateaus and voltage gradients are directly linked to the different stages, further quantified by Table 13 and graphically represented by Figure 7.5.

Table 13   Graphite phases in Li_xC_6 according to [86]

SOC Range [x in Li_xC_6]	Graphite Phase
0-0.04	Stage-1(dilute)
0.04-0.12	Stage-1(dilute) & stage 4
0.12-0.20	Stage-4 & Stage-3
0.20-0.25	Stage-3 & Stage-2(liquid)
0.25-0.50	Stage-2(liquid) & Stage-2
0.50-1	Stage-2 & Stage-1
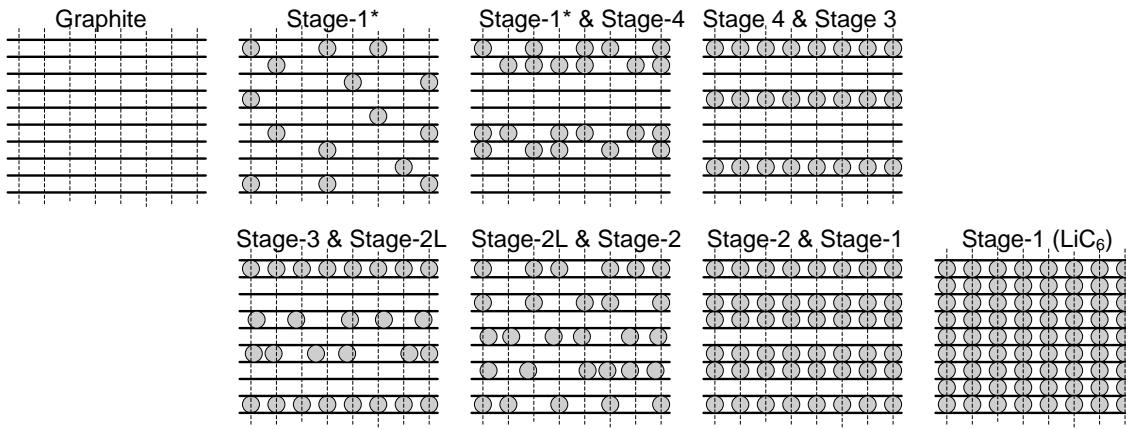
Figure 7.5   Graphical representation of the different graphite stages according to [26] and [87].

The dilute sub-stage is an in-plane ordered phase with random Li-positions occupied. Similarly, the liquid sub-stage is random but with no in-plane ordering. Several different sub-phases have been proposed by V.A. Sethuraman *et al.* [26], Dahn *et al.* [86] and R. Yazami *et al.* [87]. Note that the graphic representation in Figure 7.5 is merely a schematic view of the lithium intercalation stages in graphite. Furthermore, according to this model a graphite anode that is charged beyond 100% SOC will reach 0 V *vs.* Li/Li$^+$ which in turn may lead to Li-plating at constant potential.

7.2.1 Calculation of DVA Profile

The DVA is a method widely used to highlight the different areas in a voltage profile where the voltage derivative with respect to capacity is plotted as a function of capacity. Following the cell voltage relation to electrode voltage (7.1) and the definition of individual electrode DVA (7.2-7.3), the cell DVA is a linear combination of the two according to (7.4).

$$V_{cell} = V_{anode} + V_{cathode} \tag{7.1}$$

$$DVA_{anode} = \frac{dV_{anode}}{dC_{anode}} = f(C) \tag{7.2}$$

$$DVA_{cathode} = \frac{dV_{cathode}}{dC_{cathode}} = f(C) \tag{7.3}$$

$$DVA_{cell} = \frac{dV}{dC_{cell}} = \frac{d(V_{anode} + V_{cathode})}{dC_{cell}} = DVA_{anode} + DVA_{cathode} = f(V)$$

(7.4)

$$\text{for } C = [C_{min}...C_{max}], \quad dC \rightarrow \approx 1mAh$$

A peak in the DVA spectrum denotes a relatively fast change in voltage which for graphite electrodes is associated to the different stages of lithium intercalation. In order to observe the peaks it is necessary to record the voltage profile at sufficiently low current rate (usually < 1 C-rate) to avoid mass-transport related over-potential to overshadow the subtle changes in anode potential. An example of a DVA calculated from a C/4 charge voltage profile for a cell cycled according to *Cycle A* is shown in Figure 7.6.
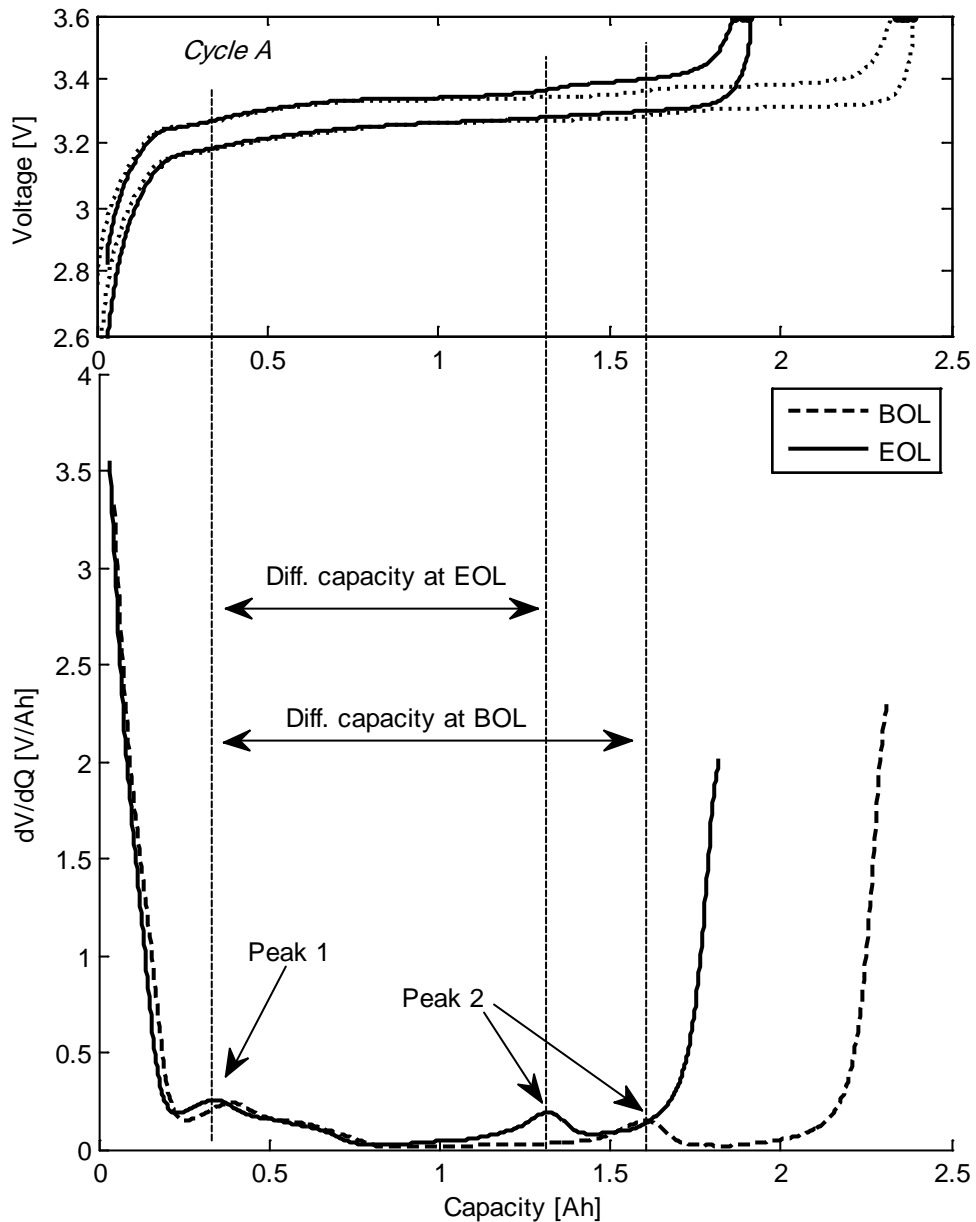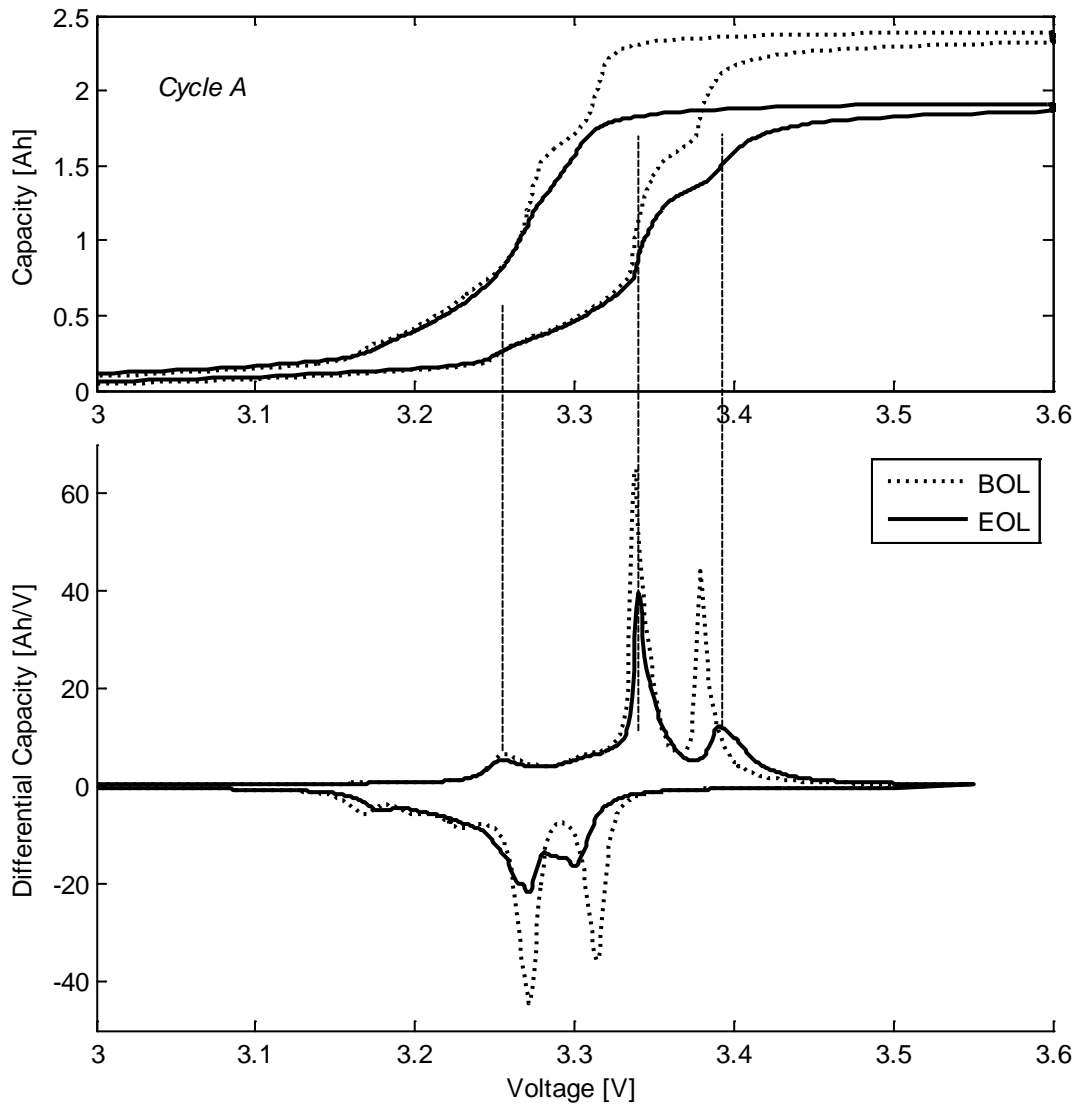

Figure 7.6   Example of DVA and C/4 voltage profile for a cell cycled according to *Cycle A* at BOL and EOL respectively.

The two peaks related to the two most significant voltage gradients in the charge curve around 0.3/0.4 and 1.1/1.7 Ah (Figure 7.2) are also highlighted in this figure to show their position change upon ageing. A reduction in anode capacity related to ageing will cause a reduction of the peak distance in the DVA, whereas ageing solely depending on the loss of lithium will leave the peak distance unaffected.

7.2.2 Calculation of ICA Profile

A closely related method to analyse the contributions from anode and cathode to the total cell voltage is the ICA. The calculation of an ICA profile is in principle the inverse of the DVA. Consequently, the anode and cathode contribution is not linearly combined to form the total cell ICA.

The ICA relies on calculation of the differential capacity for small changes in voltage according to (7.5-7.7).

$$ICA_{anode} = \frac{dC_{anode}}{dV_{anode}} = f(V) \tag{7.5}$$

$$ICA_{cathode} = \frac{dC_{cathode}}{dV_{cathode}} = f(V) \tag{7.6}$$

$$ICA_{cell} = \frac{dC_{cell}}{dV} = \frac{1}{DVA_{cell}} = \frac{1}{DVA_{anode} + DVA_{cathode}} =$$
$$= \frac{1}{\dfrac{1}{ICA_{anode}} + \dfrac{1}{ICA_{cathode}}} = f(V) \tag{7.7}$$

$$\text{for } V = [V_{min}...V_{max}], \quad dV \rightarrow \approx 1mV$$

A peak in the ICA spectrum denotes a flat region in a voltage profile. If the voltage profile is obtained at sufficiently low current rate it is possible to observe the different voltage plateaus associated to the staging of the graphite anode (see Figure 7.4) as peaks at defined voltage levels. In relation to ageing, a symmetric reduction of the peak

height is in this case an indication of an ageing regime where the cell is symmetrically aged. This is what is expected if the active material of both anode and cathode is lost at the same rate, thereby causing a loss of total cell capacity. In contrast, if other ageing mechanisms have a significant impact on the ageing, the spectrum changes in an asymmetrical way. An example of such regime is shown in Figure 7.7 where the peaks associated to the highest SOC (3.35-3.40 V for charge) are significantly more affected during ageing than the one at low SOC (3.25 V).

Figure 7.7   Example of ICA and C/4 voltage profile for a cell cycled according to *Cycle A* at BOL and EOL respectively.

From the ICA it is also possible to observe an increase in voltage drop due to an increase in overall cell impedance. In Figure 7.7 this can be seen as the shift to higher voltages for all peaks at EOL associated to charge (>0 Ah/V) and to lower voltages for peaks associated to discharge (<0 Ah/V).

7.3 Half-cell Test Results

A number of constant current charge and discharge cycles were tested on the half-cells manufactured by UU. These small pouch-type cells are made from a single coated current collector of either graphite or LiFePO$_4$ combined with a separator, a lithium metal foil and electrolyte (see section 5.1). Despite their low capacity, approx. 3 mAh, the half-cells were used to extract detailed voltage profiles for anode and cathode voltage curves representative to LiFePO$_4$//graphite cells in general. The measured voltage profiles were then used to simulate different ageing mechanisms such as loss of active lithium and loss of active material (see section 7.4). A selection of voltage profiles with current rates ranging from C/25 to C/1 is presented in Figure 7.8 and Figure 7.9 respectively. The SOC values in these graphs are calculated with the cell SOC as reference, *i.e.* not as the individual lithium content in respective electrode. Likewise, the current direction is also defined with a full-cell as reference.
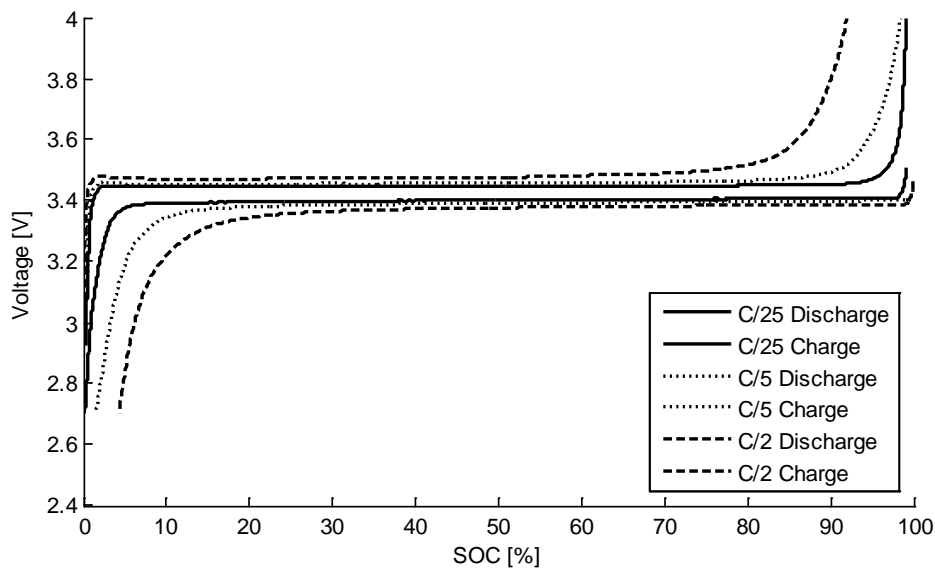

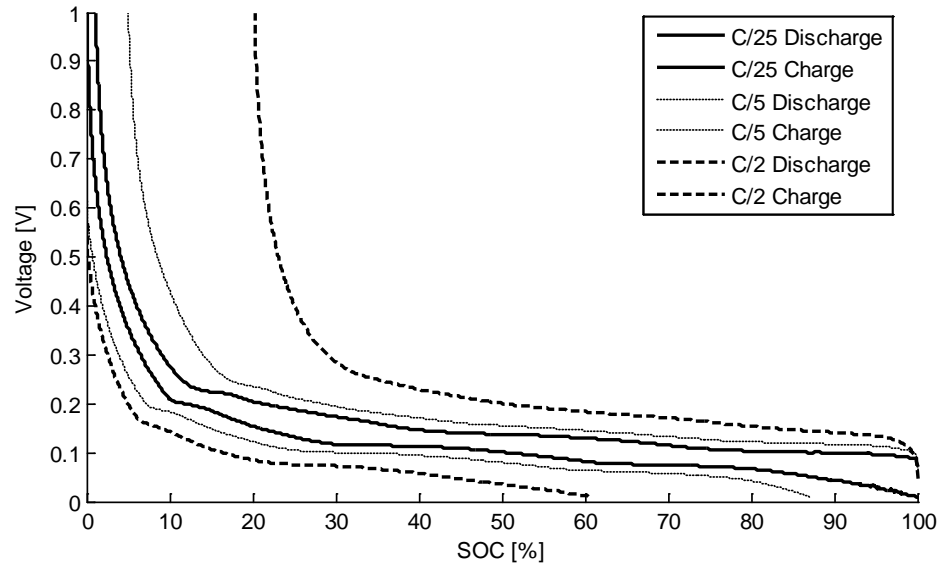Figure 7.8   Constant current voltage profiles for LiFePO$_4$ // Li half-cell.

Figure 7.9   Constant current voltage profiles for graphite//Li half-cell.

Judging from the constant current voltage profiles at higher current rates (>C/10), the small half-cells have significantly higher impedance per unit capacity than the commercial cells. Hence, they are less suitable to use in an analysis of large cell impedance or dynamics. In addition, the impedance is not constant; close to SOC=0% and SOC=100% the apparent impedance increases significantly, indicating a reduction of mass transport rate. Nevertheless, analysis methods such as ICA and DVA rely on low rate charging/discharging to characterise aging. Thus, using the low-rate profiles of half-cells may provide an insight to ageing mechanisms in commercial cells. Such analysis is presented in detail in the following section.

7.4 Cell Capacity Fade Model based on Half-cell Measurements

The measurements of half-cell voltage profiles at low current rate (C/25) were used to evaluate the use of ICA and DVA to quantify full-cell ageing mechanisms. Voltage profiles at C/25 current rate for a lithium//graphite cell between 0.01 and 2.00 V *vs.* Li/Li$^+$ and a LiFePO$_4$//lithium cell between 2.70 and 4.00 V *vs.* Li/Li$^+$ were obtained at room temperature using a Gamry Reference 3000 potentiostat and the half-cells manufactured by UU. An example of anode voltage, cathode voltage and a simulated cell voltage is shown in Figure 7.10.
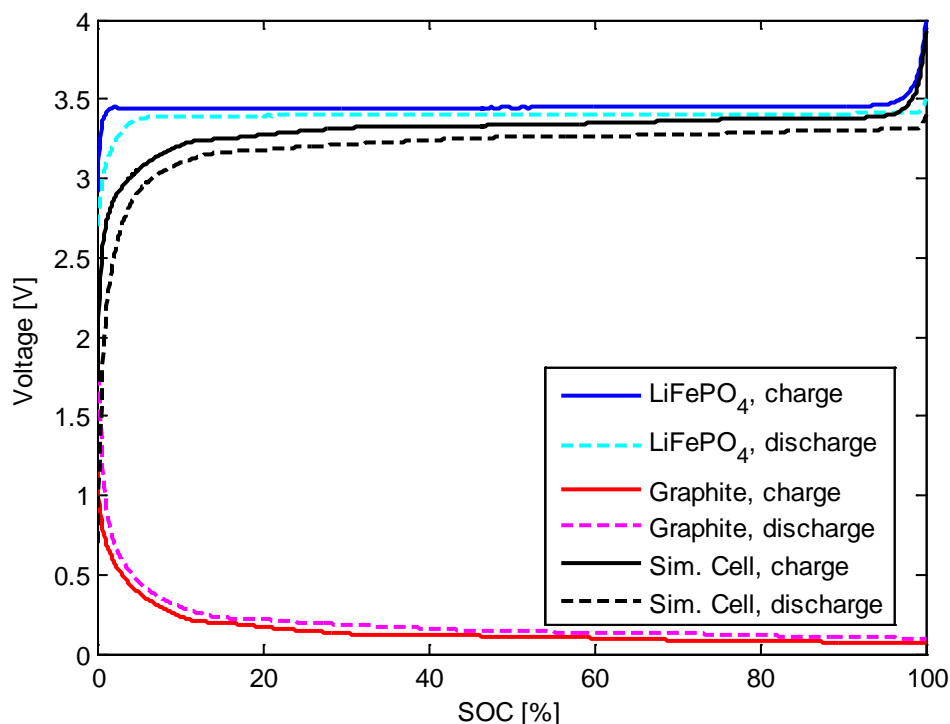
Figure 7.10   Measured half-cell voltages at C/25 and simulated cell voltage.

The voltage profiles in Figure 7.10 are obtained by normalising the capacity of the anode and cathode half-cells and then express the logged voltages as function of SOC. Then, a simulated cell voltage can be calculated as the difference between the two electrode voltages, assuming that the electrodes of this simulated cell are perfectly matched in capacity.

However, in most Li-ion cells with a graphite anode the electrodes are not matched. The cells are intentionally designed in this way to ensure that the anode voltage does not drop to zero (enabling Li-plating, see section 2.3.3) when the cell is fully charged. In addition, a slightly oversized anode might also mitigate the effect of anode ageing.

The overall effect of ageing on the voltage profiles can be simulated if a couple of simplifications are made:

- an initial anode capacity of 120% related to the cathode active material, leading to a cathode-limited charge process
- both electrodes limit the cell discharge and the cathode limits the cell charge at BOL
- loss of cyclable lithium occurs during charging or directly from the anode. That is, the stoichiometric amount of lithium in the anode decreases, in turn causing a miss-

alignment of the electrodes. If cyclable lithium is lost directly from the electrolyte when the cell is not being charged or discharged, a miss-alignment will not occur since both electrodes then preserve their respective SOC. However, any loss of lithium from the electrolyte will result in a loss of electrolyte conductivity.

- loss of active electrode material occurs gradually and evenly distributed, i.e. such loss will not cause miss-alignment between electrode SOC
- Li-plating at constant anode potential (0 V vs. Li/Li$^+$) will follow normal Li-intercalation if the anode SOC exceeds 100%

Based on these assumptions a cell model for the observable cell capacity as a function of the loss of electrode active material and cyclable lithium can be derived:

$$C_{A,EOL} = C_{A,BOL} \cdot (1 - Loss_A) \tag{7.8}$$

$$C_{C,EOL} = C_{C,BOL} \cdot (1 - Loss_C) \tag{7.9}$$

$$C_{A,startpoint} = Loss_{Li} C_{C,BOL} + \frac{Loss_A C_{A,BOL}}{2} \tag{7.10}$$

$$C_{C,startpoint} = \frac{Loss_C C_{C,BOL}}{2} \tag{7.11}$$

$$C_{A,endpoint} = C_{A,BOL} + Loss_{Li} C_{C,BOL} - \frac{Loss_A C_{A,BOL}}{2} \tag{7.12}$$

$$C_{C,endpoint} = C_{C,BOL} - \frac{Loss_C C_{C,BOL}}{2} \tag{7.13}$$

$$C_{Cell} = \min(C_{A,endpoint}, C_{C,endpoint}) - \max(C_{A,startpoint}, C_{C,startpoint}) \tag{7.14}$$

where

$C_{X,BOL}$: initial electrode capacity

$C_{X,EOL}$: electrode capacity after ageing

$C_{X,startpoint}$: position [Ah] of SOC=0% of each electrode relative to cell SOC=0%

$C_{X,\,endpoint}$:　　　　　　position [Ah] of SOC=100% of each electrode relative to cell SOC=100%

C_{Cell} :　　　　　　observable cell capacity.

An example of a cell simulation based on assuming 20% loss of cyclable lithium is shown in Figure 7.11.
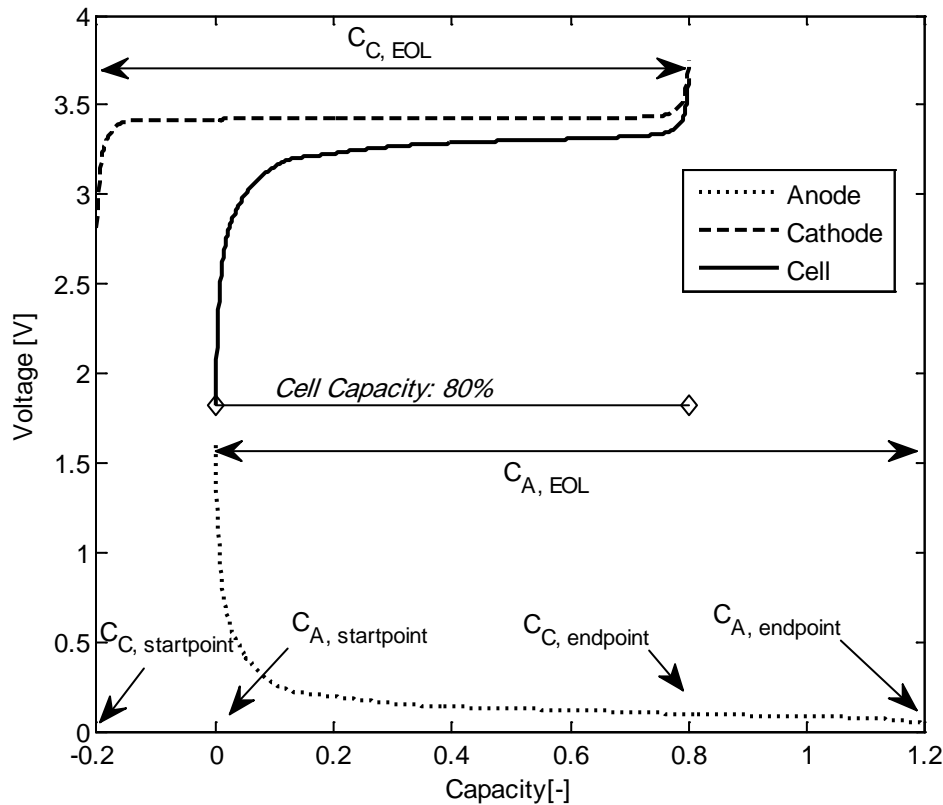

Figure 7.11　Calculation of observable capacity assuming 20% loss of cyclable lithium.

This simulation is made by calculating the individual electrode capacities as function of ageing (7.8-7.9), their alignment on a normalised capacity scale (7.10-7.13) and the resulting cell capacity as the difference between the electrode capacity positions (7.14). The cell voltage is calculated as the difference between electrode potentials between the two capacity boundaries used in (7.14).

In Figure 7.11 the anode limits the discharge of the cell when it reaches zero SOC (rapid increase in potential *vs.* Li$^+$/Li). Similarly, the cathode limits the charge of the cell as its potential increase although the anode is still at SOC < 100%. The miss-alignment of the electrodes is clearly visible in this figure as the shift in start-point of the cathode voltage curve from zero to -0.2. Also, note that the respective electrode capacities do not change

in this example: anode capacity is still 1.2 and the cathode capacity 1.0 according to the assumed start conditions.

In cases where the cathode limits the initial capacity of the cell ($C_{A,BOL}>C_{C,BOL}$), the expression for the cell capacity (7.14) can be simplified further:

$$C_{Cell} = C_{C, endpoint} - C_{A, startpoint} =$$
$$= C_{C, BOL} - \frac{Loss_C C_{C, BOL}}{2} - Loss_{Li} C_{C, BOL} - \frac{Loss_A C_{A, BOL}}{2} = \tag{7.15}$$
$$= C_{C, BOL}\left(1 - \frac{Loss_C}{2} - Loss_{Li}\right) - \frac{Loss_A C_{A, BOL}}{2}$$

This relation shows that a loss of cyclable lithium has a more profound effect on the observable cell capacity than loss of active electrode area. However, this observation is strongly depending on the assumption that loss of active electrode material is evenly distributed with respect to electrode SOC. To further relate the changes of the electrode capacity and relative alignment, (7.8 – 7.15) can be used to calculate the respective SOC of the two electrodes as functions of loss of active material or cyclable lithium:

$$SOC_{C, \text{ cell }0\%} = \frac{\max\left(C_{A, startpoint}, C_{C, startpoint}\right) - C_{C, startpoint}}{C_{C, endpoint} - C_{C, startpoint}} \tag{7.16}$$

$$SOC_{C, \text{ cell }100\%} = \frac{\min\left(C_{A, endpoint}, C_{C, endpoint}\right) - C_{C, startpoint}}{C_{C, endpoint} - C_{C, startpoint}} \tag{7.17}$$

$$SOC_{A, \text{ cell }0\%} = \frac{\max\left(C_{A, startpoint}, C_{C, startpoint}\right) - C_{A, startpoint}}{C_{A, endpoint} - C_{A, startpoint}} \tag{7.18}$$

$$SOC_{A, \text{ cell }100\%} = \frac{\min\left(C_{A, endpoint}, C_{C, endpoint}\right) - C_{A, startpoint}}{C_{A, endpoint} - C_{A, startpoint}} \tag{7.19}$$

Here, the SOC-values are related to that of the full cell. That is, $SOC_{C, \text{ cell }100\%}=100\%$ is equal to 100% $FePO_4$ in the cathode and $SOC_{A, \text{ cell }100\%}=100\%$ is equal to 100% LiC_6 in the cathode.

To highlight the main result of this simplified cell ageing modelling method, four different cases of ageing are presented in this investigation:

    Case 1:   0-30% loss of cyclable lithium

    Case 2:   0-45% loss of active anode material

                The case of 45% anode loss leads to Li-plating

    Case 3:   0-30% loss of active cathode material

    Case 4:   0-10% loss of cyclable lithium and 0-10% loss of active electrode material

These four cases are presented and analysed in more detail in the following sections.

7.4.1 Case 1: Loss of Cyclable lithium

A loss of cyclable lithium may cause a miss-alignment of the electrodes and an increase in cell impedance. That is, the amount of lithium in the anode at cell SOC=100% decreases. In Figure 7.12 the potential of the anode, the cathode and the corresponding simulated cell potential are presented at BOL assuming a 20% oversized anode.
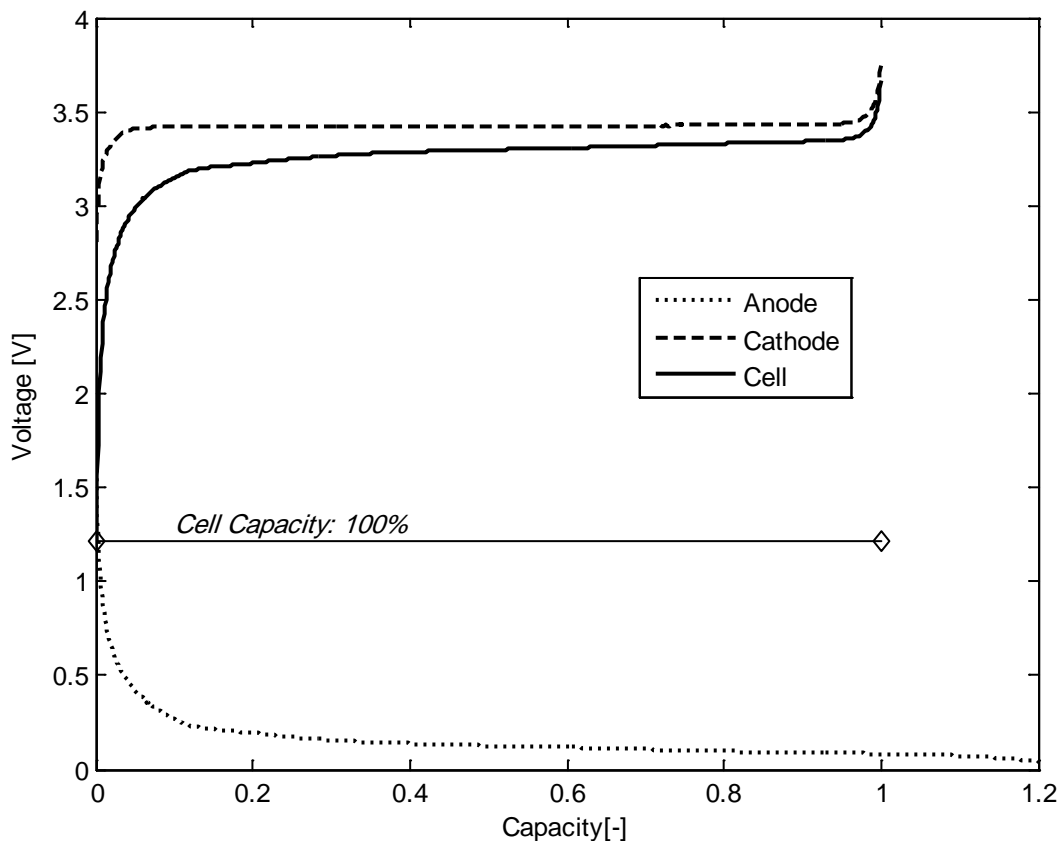
Figure 7.12   Anode, cathode and simulated cell potential at BOL.

Note that at cell SOC=100%, the rise in cathode potential limits the charge, and at 0% SOC both anode and cathode limit the cell operation as their respective rapid changes in potential results in a rapid decrease in cell voltage.

A 30% loss of cyclable lithium was simulated using the model presented in the previous section, causing a severe miss-alignment between electrode potentials. The effect of this ageing mechanism on the cell voltage is presented in Figure 7.13 and Figure 7.14, respectively.
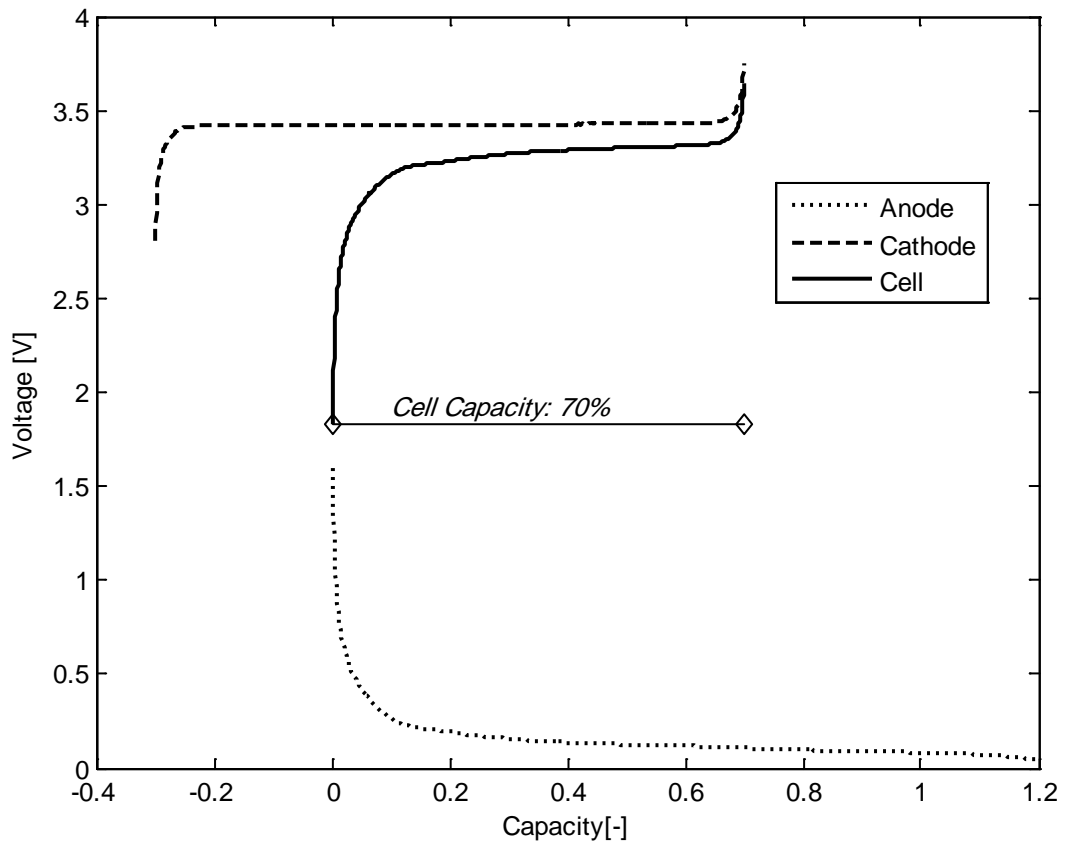

Figure 7.13   Anode, cathode and simulated cell potential *vs.* capacity at 30% loss of cyclable lithium.

The indicated cell capacity in this simulation is relative to the available capacity in the cell rather than the electrode capacities. Here, one of the most obvious effects on the observable cell voltage is that the plateau related to the stage-2/stage-1 two-phase region of the graphite is shortened as the cathode is limiting the charge at a lower anode charge level (Figure 7.14). Neither the cathode nor the anode is utilized to its full extent in this severe case of loss of cyclable lithium.
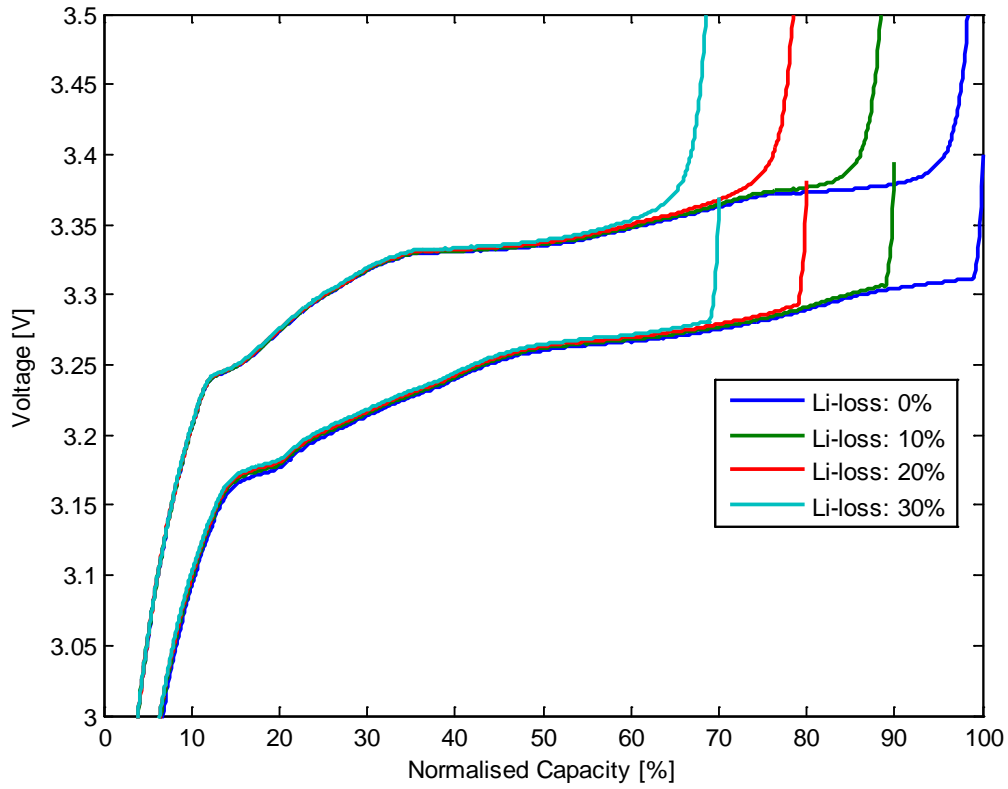
Figure 7.14   Cell voltage *vs.* normalised capacity at simulated Li-loss of 0-30%.

Furthermore, the corresponding DVA (Figure 7.15) and the ICA (Figure 7.16) profiles also show distinguishable changes in their characteristics upon loss of cyclable lithium.
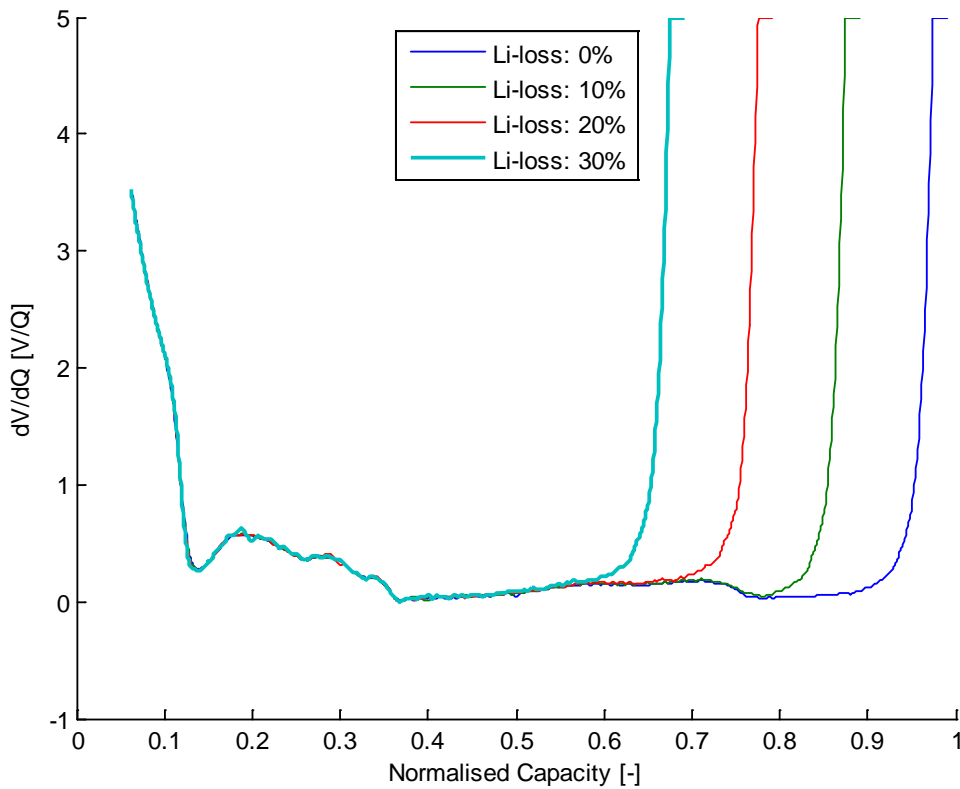

Figure 7.15   DVA at simulated Li-loss of 0-30%.

In the DVA (Figure 7.15), the profile is almost identical for Li-loss 0-20% except an early cut-off in the right region where the cathode limits the charge.
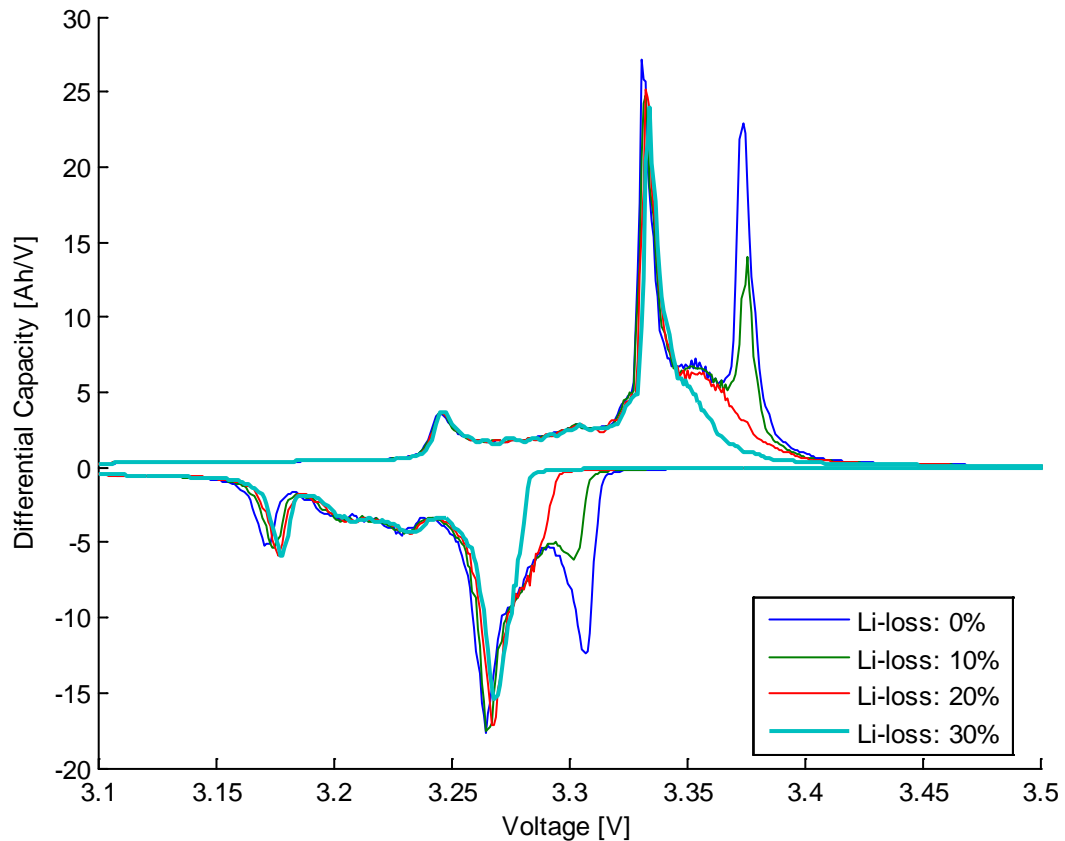

Figure 7.16   ICA at simulated Li-loss of 0-30%.

Likewise, the absence of the stage-2/stage-1 plateau in the graphite is shown clearly in the ICA (Figure 7.16) where the peaks at 3.38 V(charge) and 3.31 V(discharge) gradually disappear.

As a concluding remark, a loss of cyclable lithium results in observable changes in both voltage profiles, DVA and ICA.

7.4.2 Case 2: Loss of Active Anode Material

When anode material is lost the effect on the cell voltage profiles are less pronounced (Figure 7.17 and Figure 7.19). At 30% loss, the anode is fully utilized compared to the 80% utilization rate at BOL. The cell voltage profile then occurs to be compressed, preserving the main characteristics although the stage-2/stage-1 plateau in the graphite is widened as the cathode cuts off the charging at 100% graphite SOC.
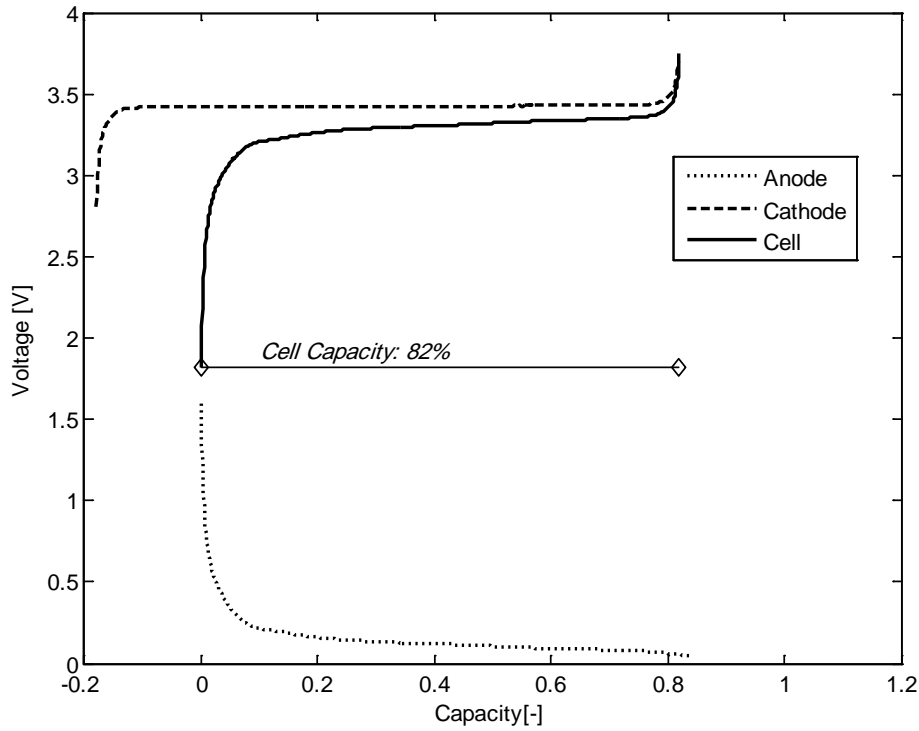
Figure 7.17   Anode, cathode and simulated cell potential *vs.* capacity at 30% loss of active anode material.

When 45% active anode material is lost the anode voltage reaches 0 V vs. Li/Li$^+$ which in turn, in this simulation, leads to Li-plating (Figure 7.18).
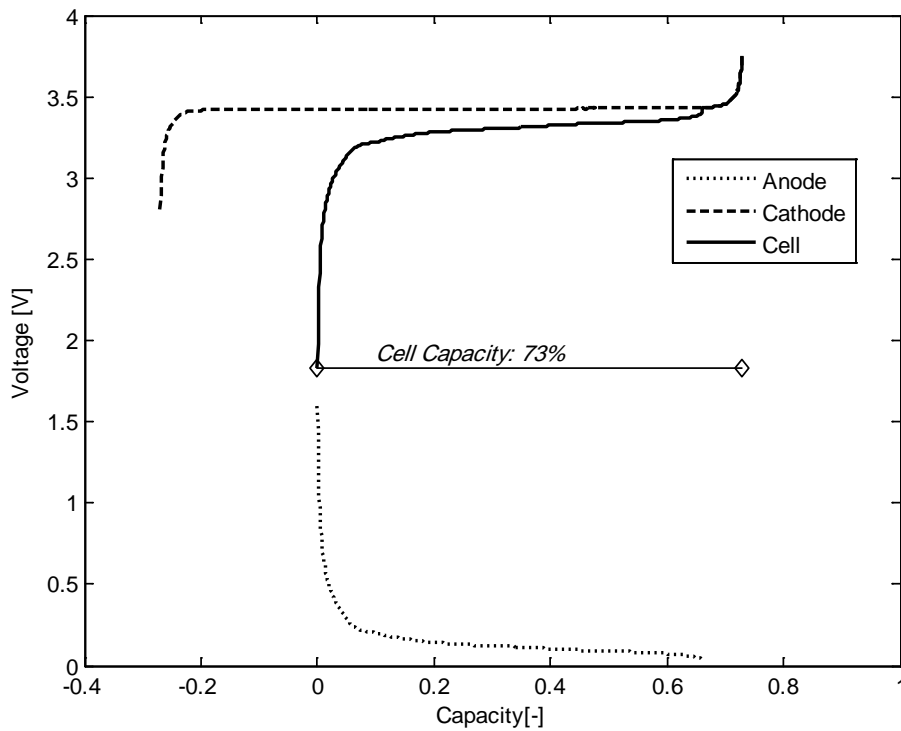

Figure 7.18   Anode, cathode and simulated cell potential *vs.* capacity at 45% loss of active anode material.

In the voltage profile this can be observed as the additional voltage plateau close to SOC=100% at the point where the anode potential is stabilised at 0 V *vs.* Li/Li$^+$ (Figure 7.19).
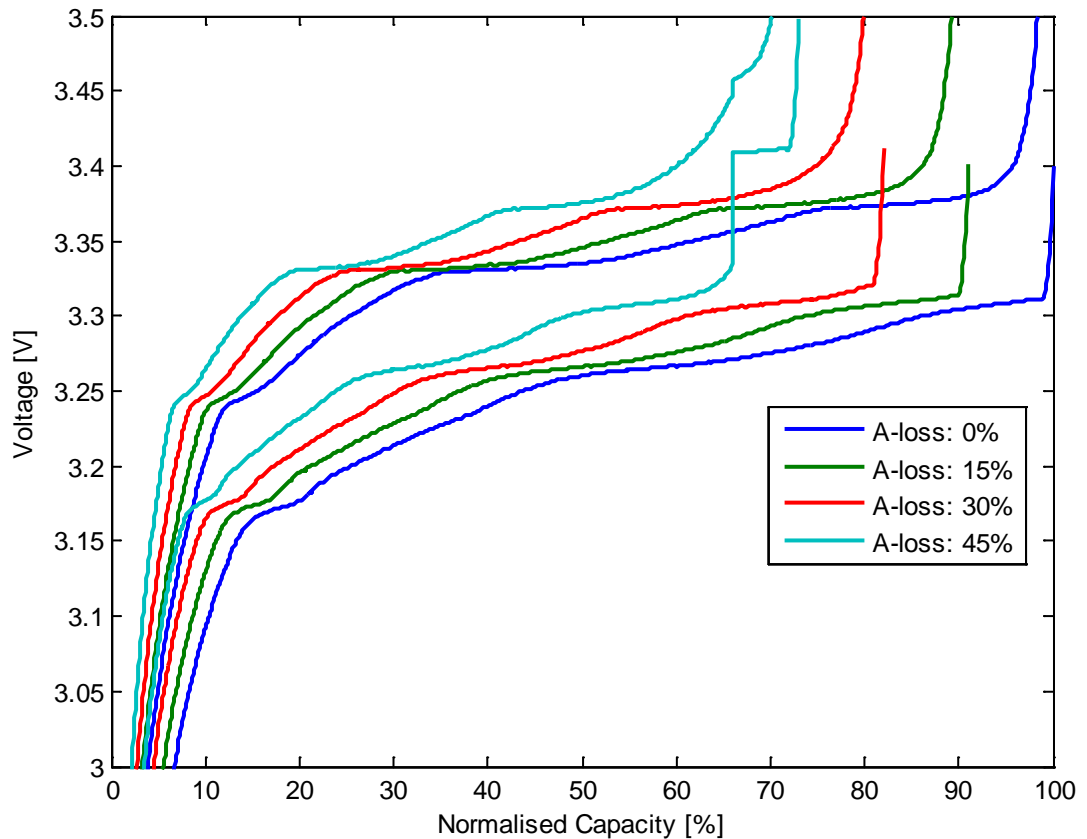

Figure 7.19   Cell voltage *vs.* normalised capacity at simulated anode material loss of 0-45%.

In this simulation no measurements of the anode potential during Li-plating has been made. Hence, the estimated voltage profile does not take the changes in the cell dynamics into account which leads to a discontinuous voltage profile for cell discharge.

The compression of the voltage curve and the widening of the stage-2/stage-1 plateau are also shown in the DVA and the ICA profiles (Figure 7.20 and Figure 7.21 respectively).
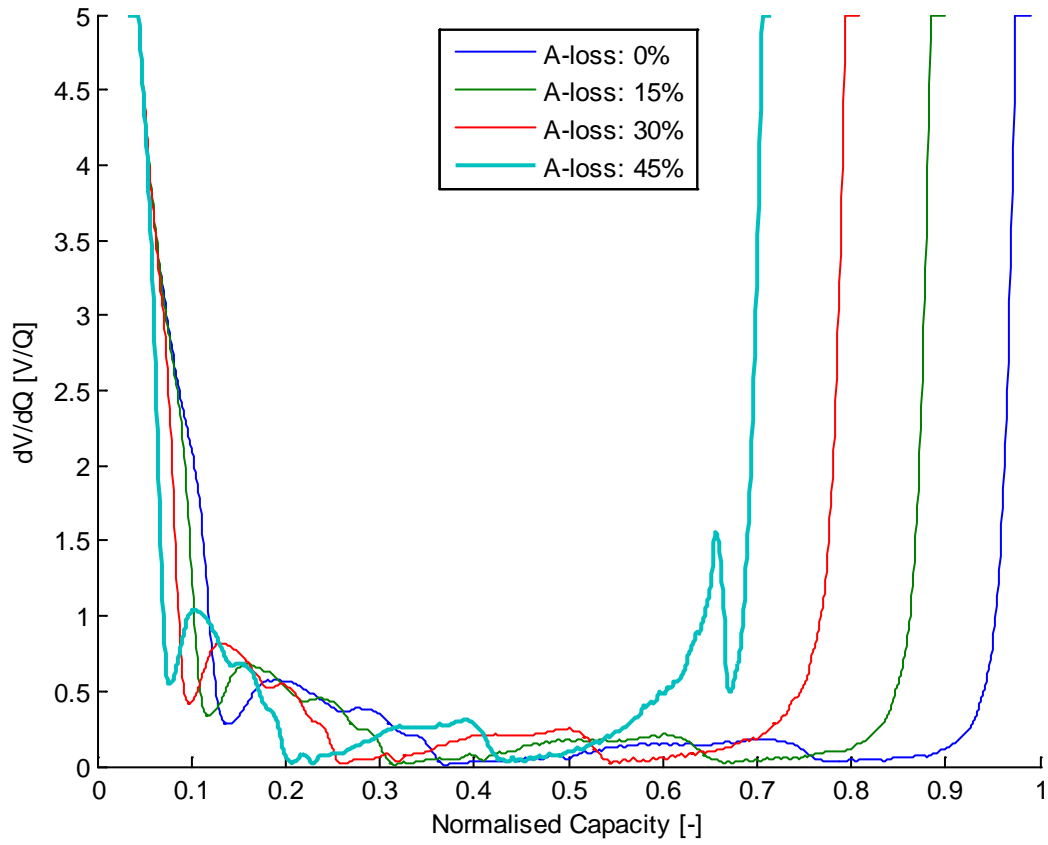
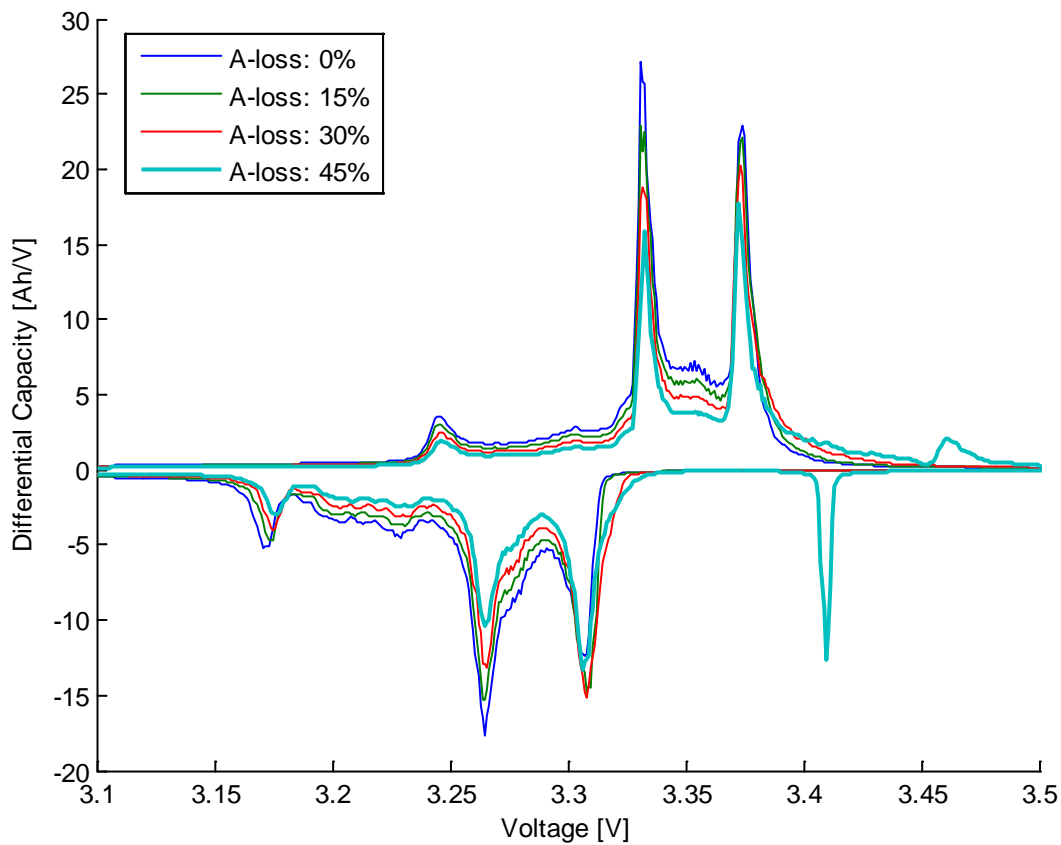Figure 7.20   DVA at simulated anode material loss of 0-45%.

Figure 7.21   ICA at simulated anode material loss of 0-45%.

Of special interest is that the inter-distance between the peaks in the DVA profile is reduced at the same rate as the loss of active anode material. Also, note that the peak at 3.31 V (discharge) in the ICA (Figure 7.21) increases in magnitude.

The new plateau at high SOC causes an extra peak in the DVA profile when the anode reaches 100% SOC. Likewise, two new peaks directly related to Li-plating can be observed in the ICA profile at 3.47 V (charge) and 3.41 V(discharge).

7.4.3 Case 3: Loss of Active Cathode Material

Despite the lack of multiple two-phase regions yielding several voltage plateaus, a loss of active cathode changes the voltage profiles (Figure 7.22 and Figure 7.23) in a profound way; after ageing the cathode will limit both charge and discharge, effectively limiting the utilization of the anode until the cell operates in the mid-range of the curve with only two observable graphite phase plateaus. In addition, the cut-off at low cell SOC will be very sharp.
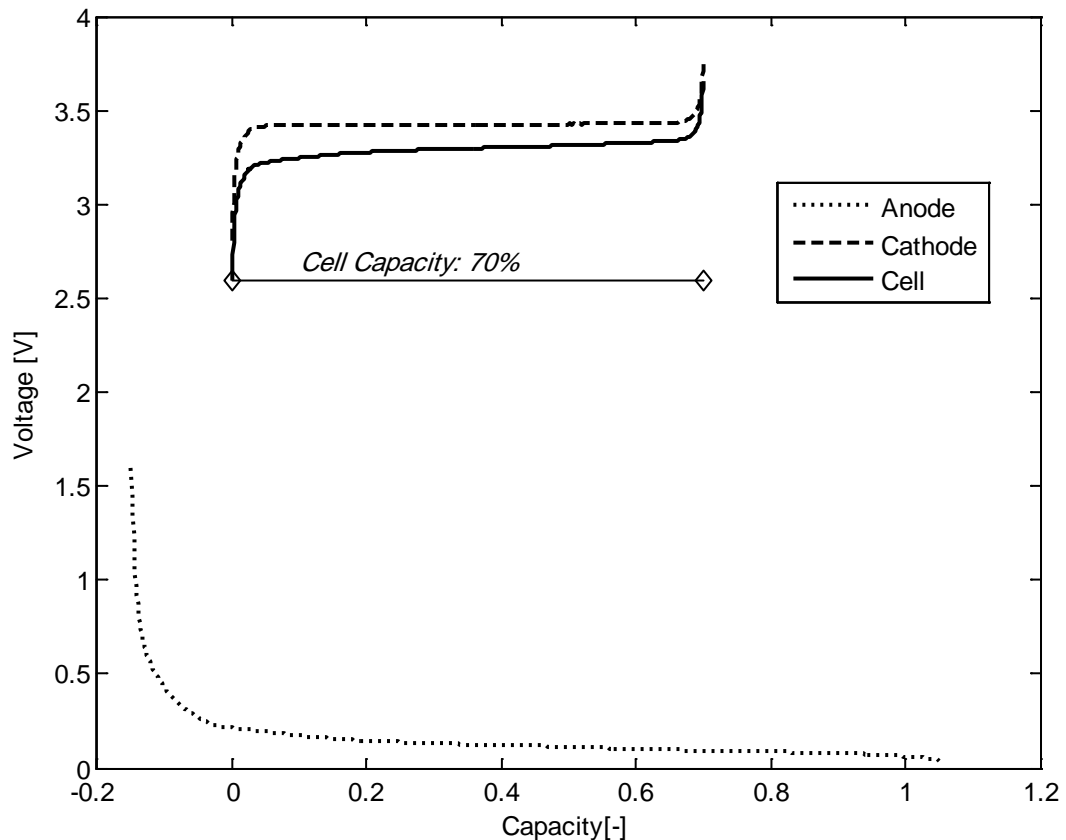

Figure 7.22   Anode, cathode and simulated cell potential *vs.* capacity at 30% loss of active cathode material.
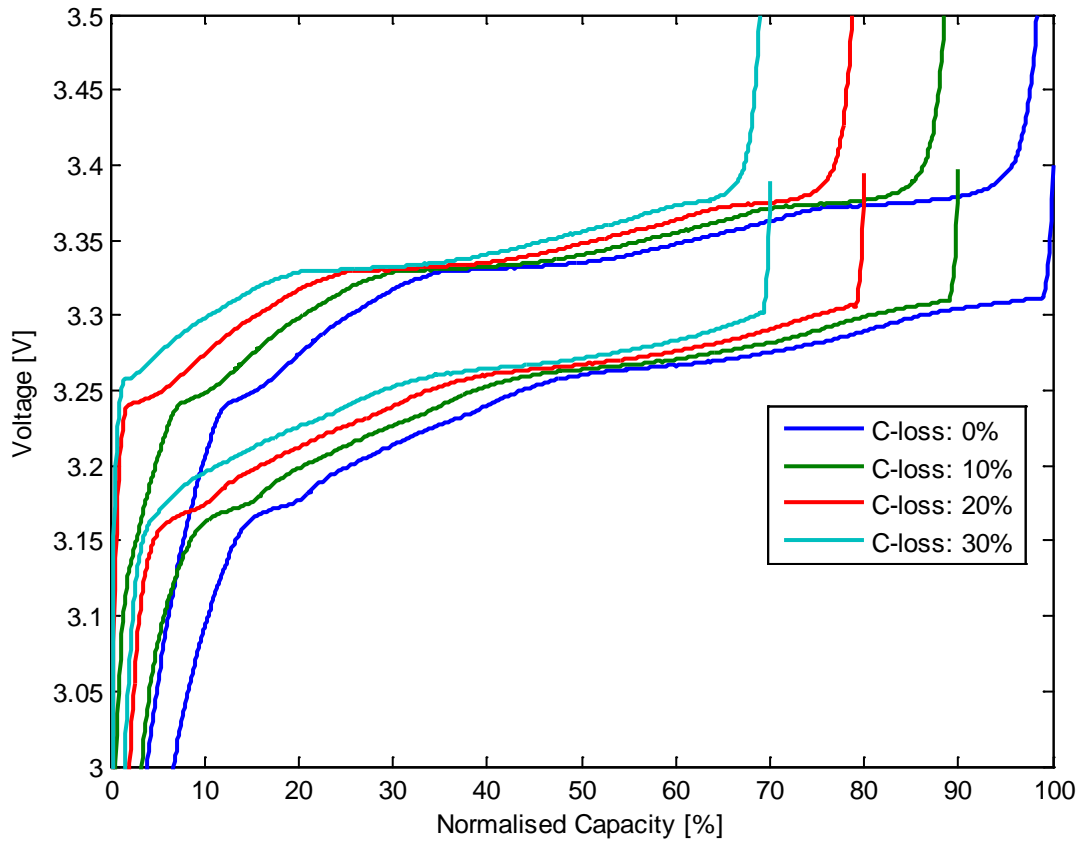
Figure 7.23   Cell voltage *vs.* normalised capacity at simulated cathode material loss of 0-30%.

Subsequently, the peaks in the DVA and ICA profiles associated the graphite stage-4 and stage-3 gradually disappears (Figure 7.24 and Figure 7.25) but leaving the centre peak at 3.35 V(charge) in the ICA profile mainly associated to the cathode virtually unaffected.
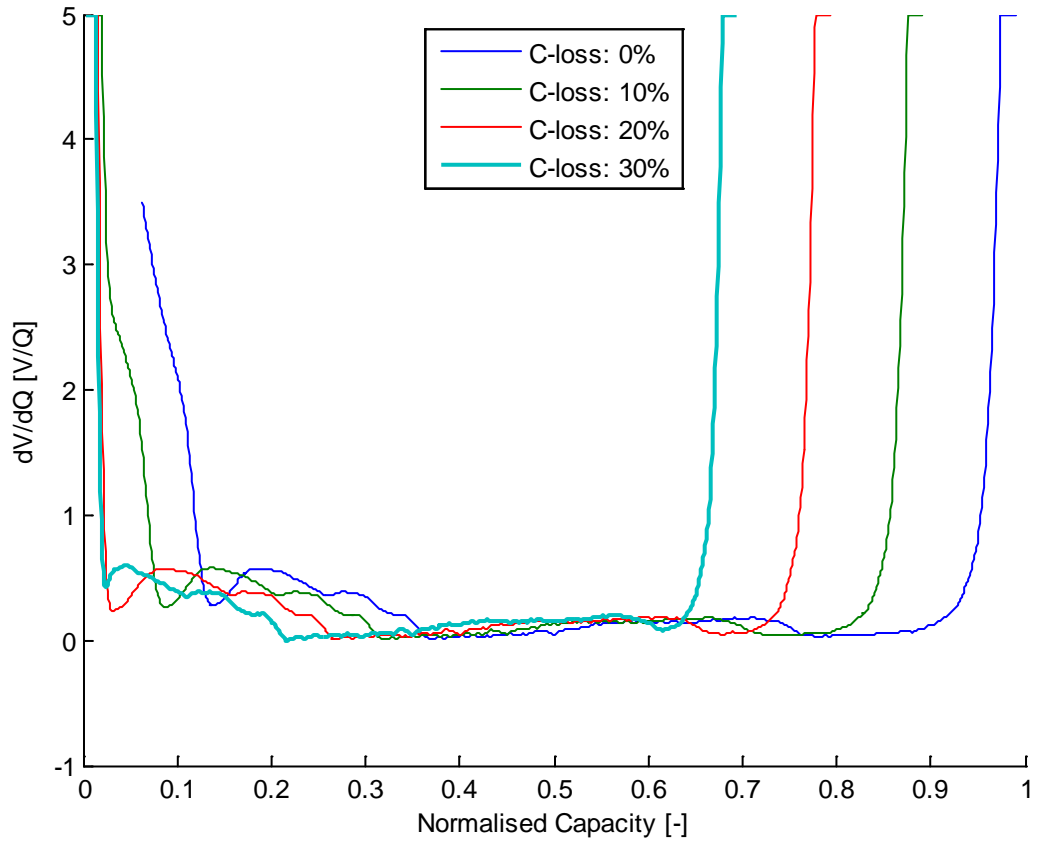
Figure 7.24   DVA at simulated cathode material loss of 0-30%.
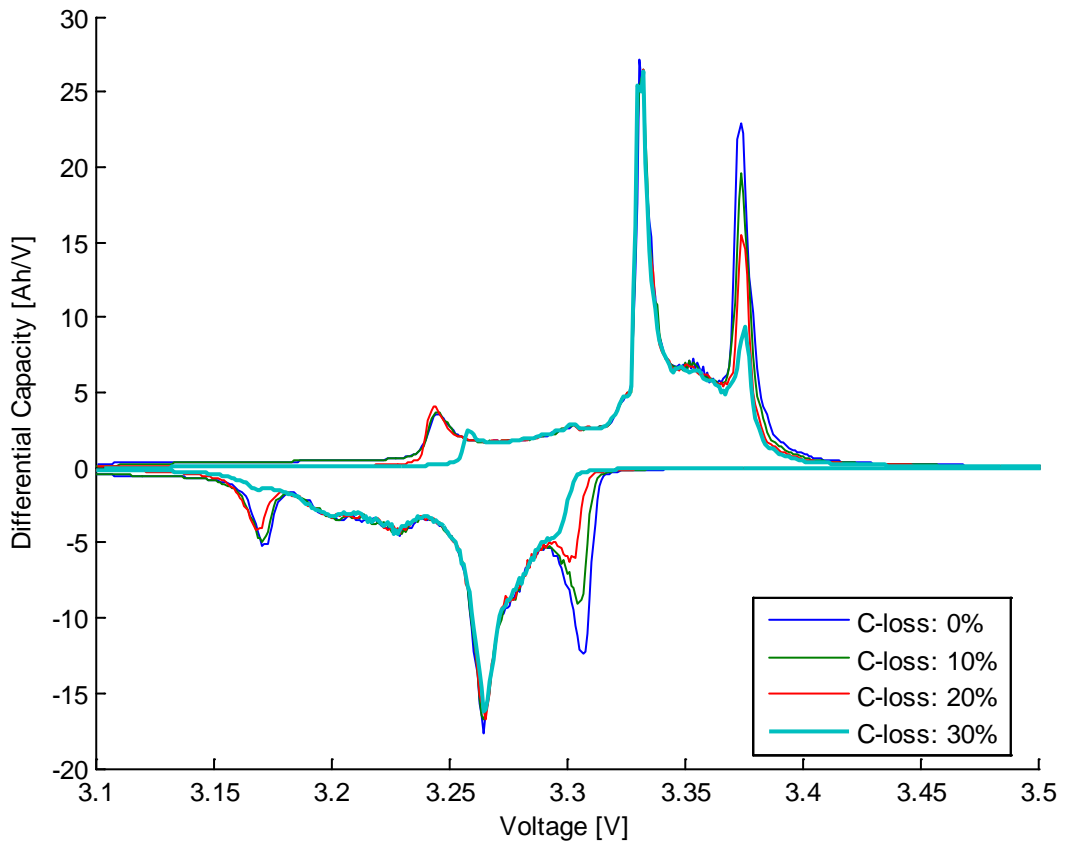

Figure 7.25   ICA at simulated cathode material loss of 0-30%.

7.4.4 Case 4: Loss of Cyclable lithium and Active Electrode Material

The last example of simulated ageing is probably one of the most realistic: a combination of loss of cyclable lithium (10%) and active electrode material (10% loss of anode and cathode material respectively).

Starting with voltage profiles (Figure 7.26 and Figure 7.27) both the effect of lithium loss and electrode material loss is observable in the compression of the voltage profile and the reduction of the anode utilization range at high electrode charge level.
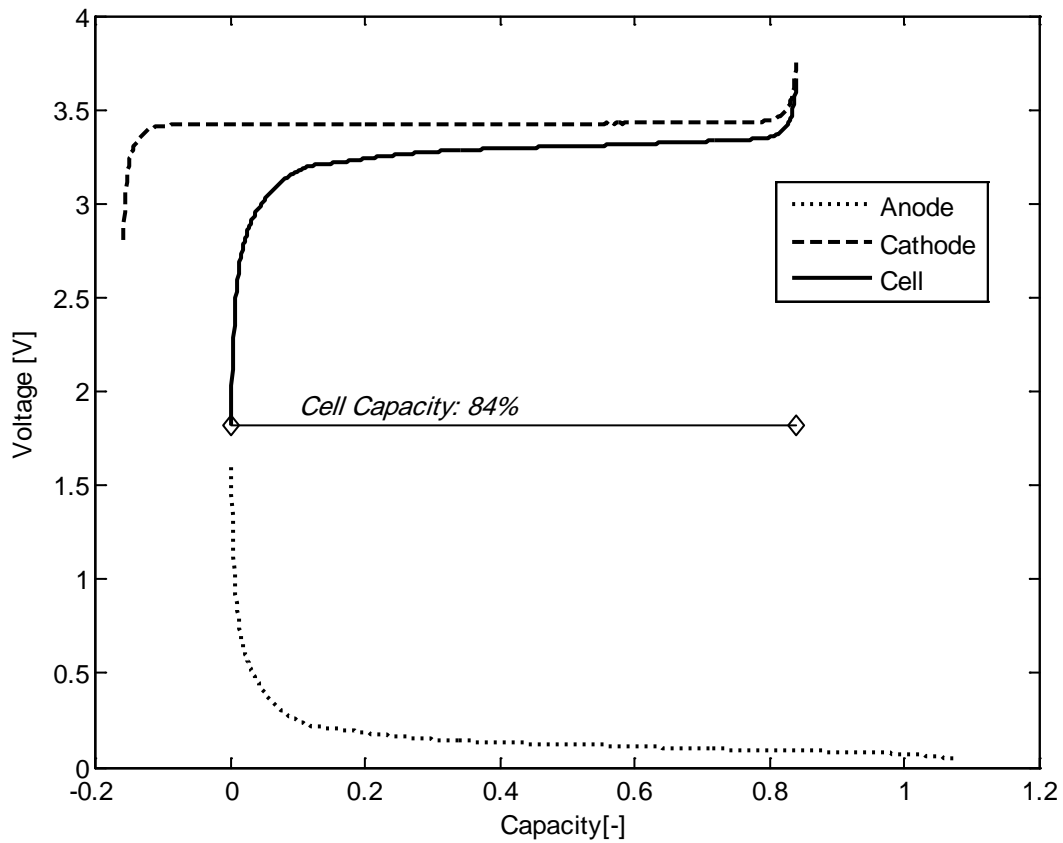

Figure 7.26   Anode, cathode and simulated cell potential *vs.* capacity at 10% loss of Li and electrode material.
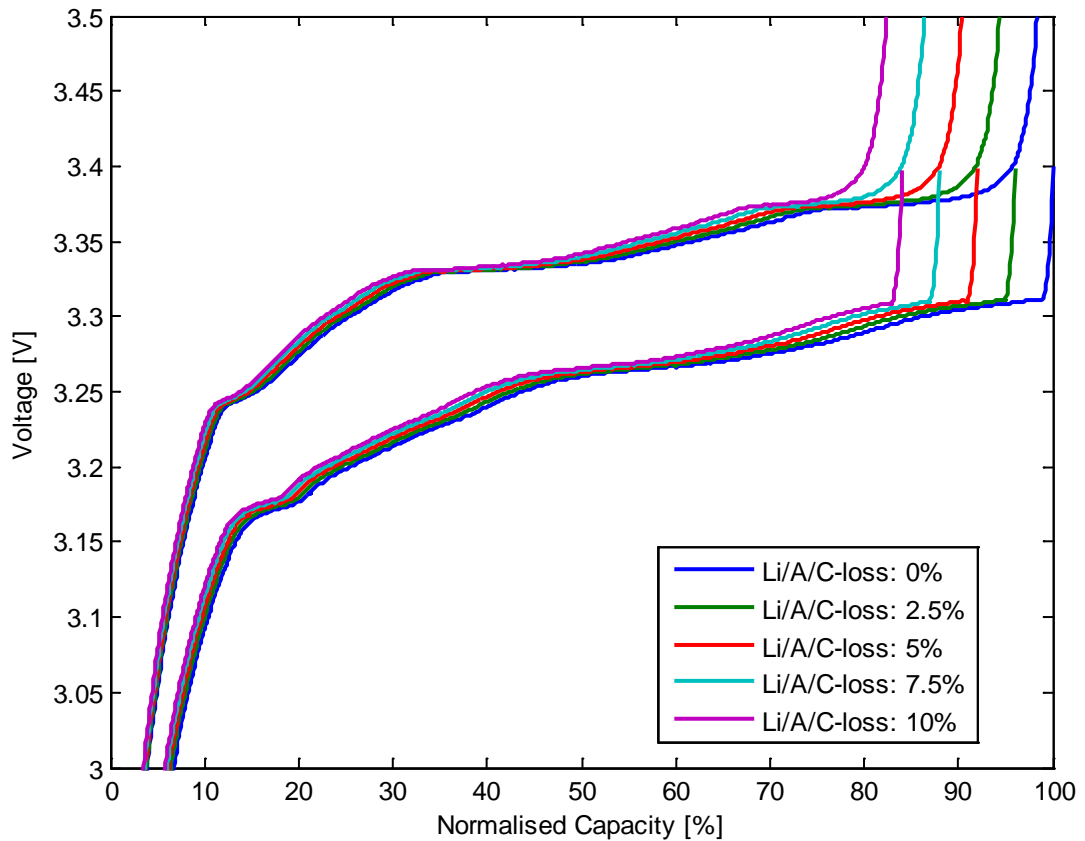
Figure 7.27   Cell voltage *vs.* normalised capacity at simulated Li-loss and electrode material loss of 0-10%.

Again, the same effect is observed in the DVA profile (Figure 7.28); a reduction of the peak corresponding to the stage-2/stage-1 and a compression of the profile. In the ICA profile (Figure 7.29) all peaks are reduced but with an emphasis in the 3.38 V (charge) peak.

Despite that different ageing mechanisms have a different effect on voltage profiles, DVA and ICA, it can be concluded that this method can prove to be a useful method when evaluating the ageing of full-cells.
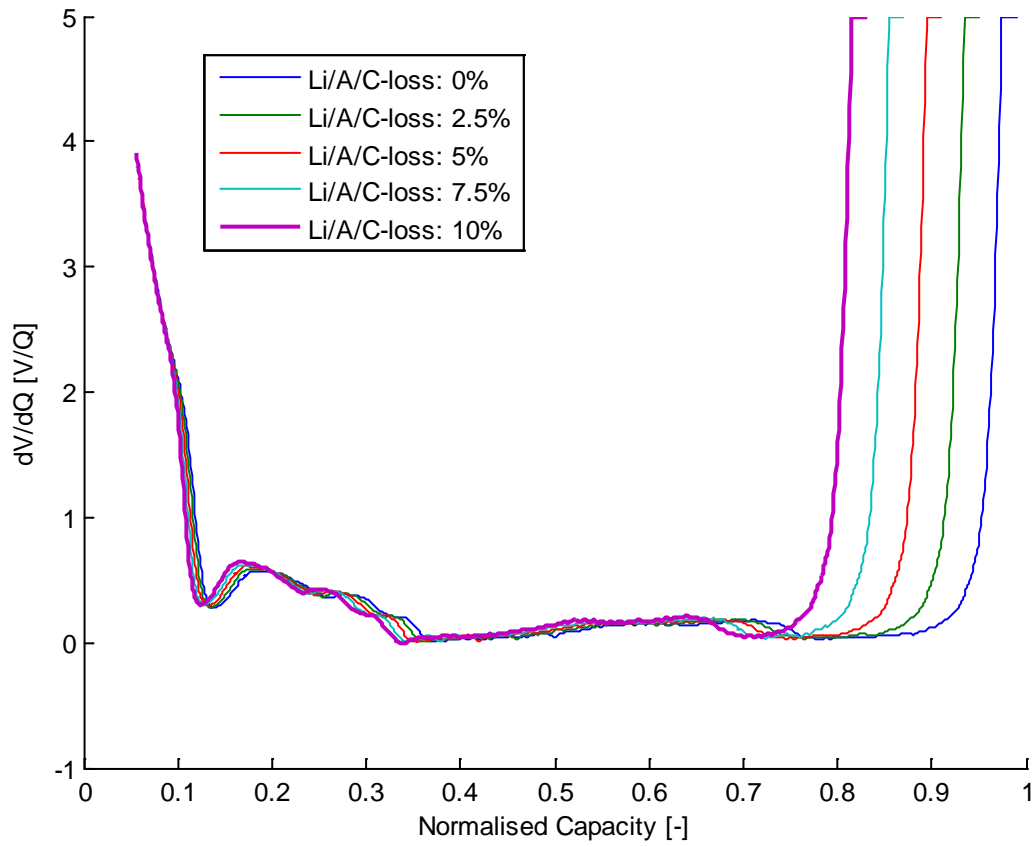
Figure 7.28   DVA at simulated Li-loss and electrode material loss of 0-10%.
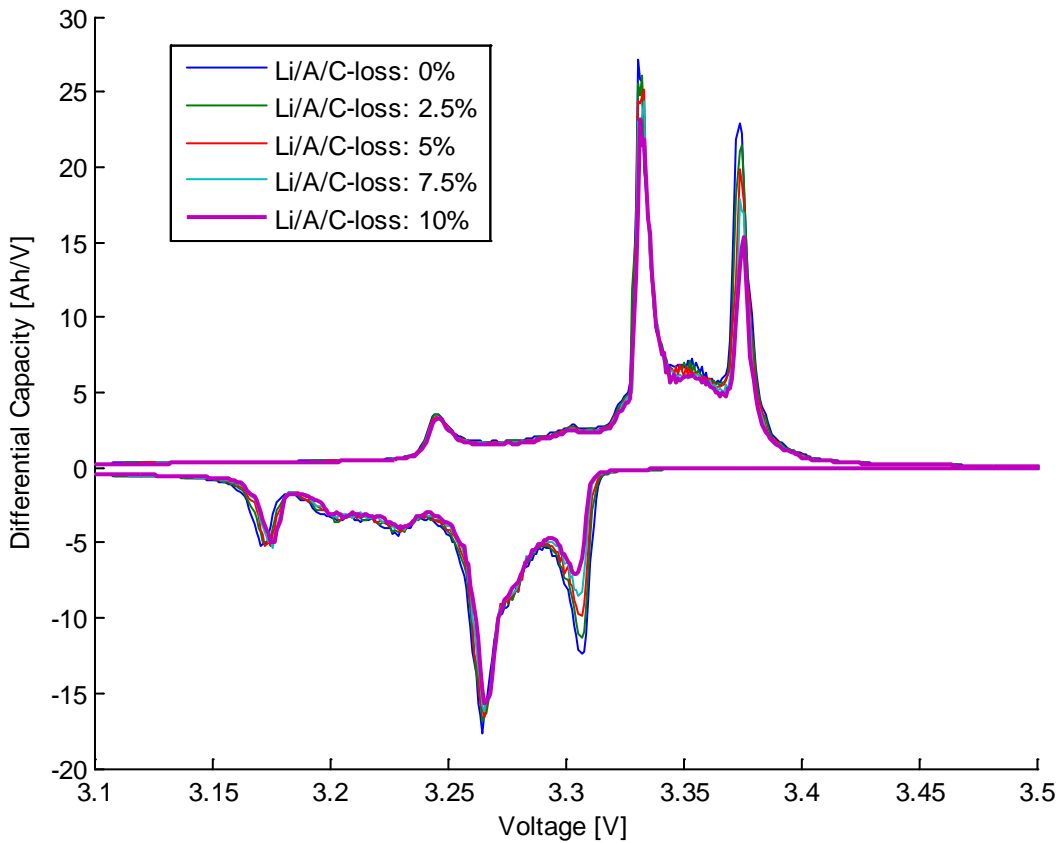
Figure 7.29   ICA at simulated Li-loss and electrode material loss of 0-10%.

7.5 ICA & DVA of Aged Cells

Incremental capacity analysis and differential capacity analysis were performed for all cells based on the C/4 voltage profiles measured during each RPT. A collection of results are briefly presented in this section. These results are then used to quantify the aging in terms of loss of cyclable lithium and active electrode material (see section 7.6).

An ICA was calculated at BOL and EOL for all cells cycled according to *Cycle A-E* (Figure 7.30).

Figure 7.30   ICA for cells cycled according to *Cycle A-E*.

For all cells in Figure 7.30 the ICA profiles indicate that several ageing mechanisms are contributing to the ageing. Firstly, the peak associated to the stage-2/stage-1 lithiation of the graphite is significantly reduced, in turn indicating loss of cyclable lithium in correspondence with the model presented in the previous section and as reported in literature. Secondly, all other peaks are reduced in magnitude which indicates a loss of active anode material. Lastly, the shift in peak position reveals a significant increase in cell impedance.
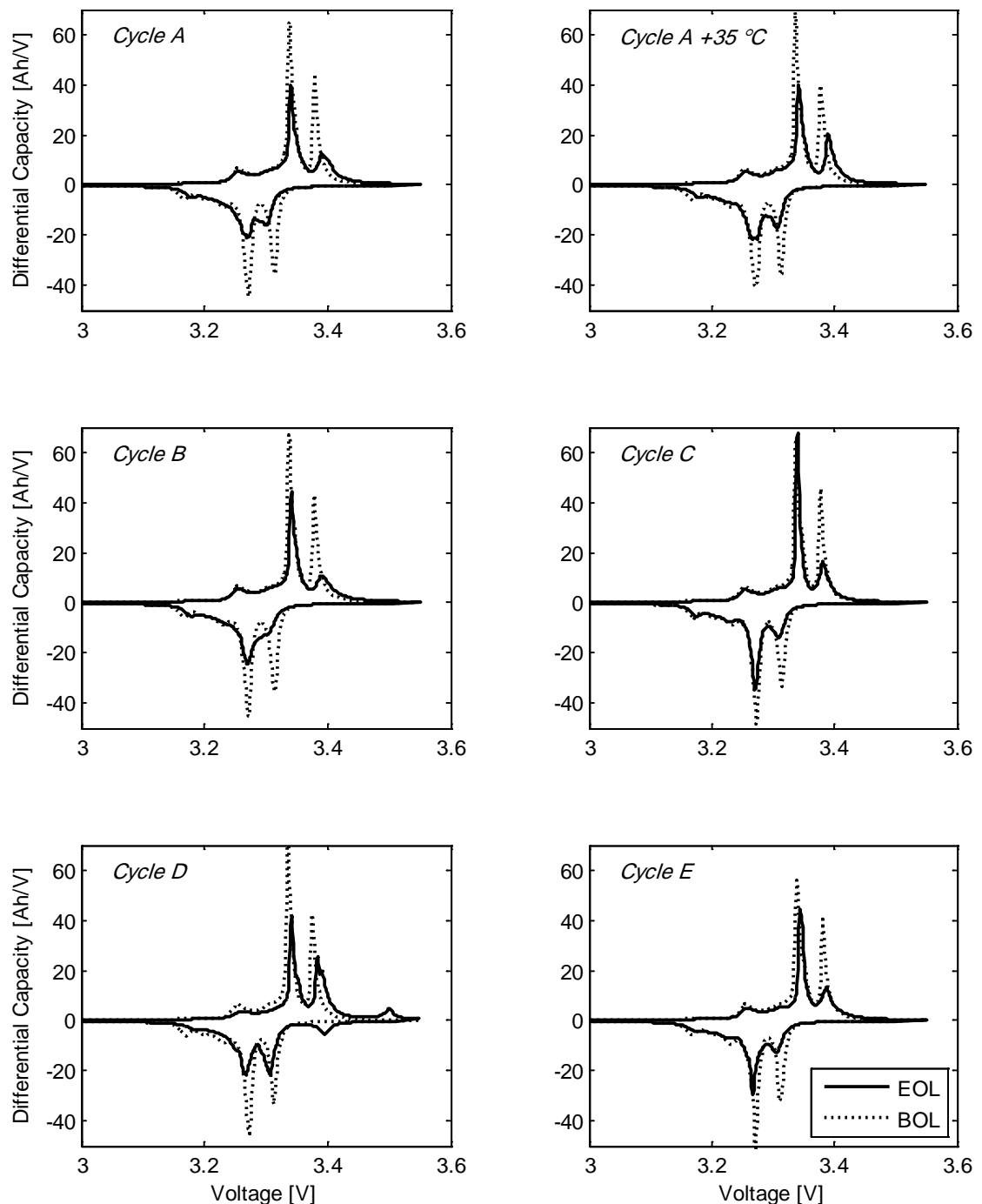
There are two differences in ICA between the PHEV cycles *Cycle C* and *Cycle E* and the HEV cycles *Cycle A* and *Cycle B*; the peak positions do not change indicating a lower impedance increase and the reduction of the centre peak in the ICA is not at all as reduced. Furthermore, *Cycle D* shows two additional peaks in the ICA profile at high cell voltage, possibly indicating reversible Li-plating in correspondence with the results obtained with cell fade model simulations in section 7.4.2. Similar conclusions can be drawn from the DVA for the same cells (Figure 7.31).

The DVA profiles in Figure 7.31 are compressed representing a loss of active anode material that can be quantified by calculating the peak distance as described in section 7.2. Also, the capacity related to the stage-2/stage-1 is greatly reduced; demonstrating the effect of lithium loss. However, it should be noted that the cells cycled according to *Cycle C* reaches EOL significantly earlier in terms of total capacity throughput than cells cycled with *Cycle A* or *Cycle B* (see section 6.1).

EOL is reached at approximately twice the capacity throughput for *Cycle E* compared to *Cycle C*. Hence, the ageing with the PHEV cycle is half as fast in terms of capacity fade, but the impedance increase at EOL is comparable.

Likewise to the ICA results, there is an extra peak seen for *Cycle D* for high SOC, positioned approximately where Li-plating would occur according to the cell fade model simulation results.
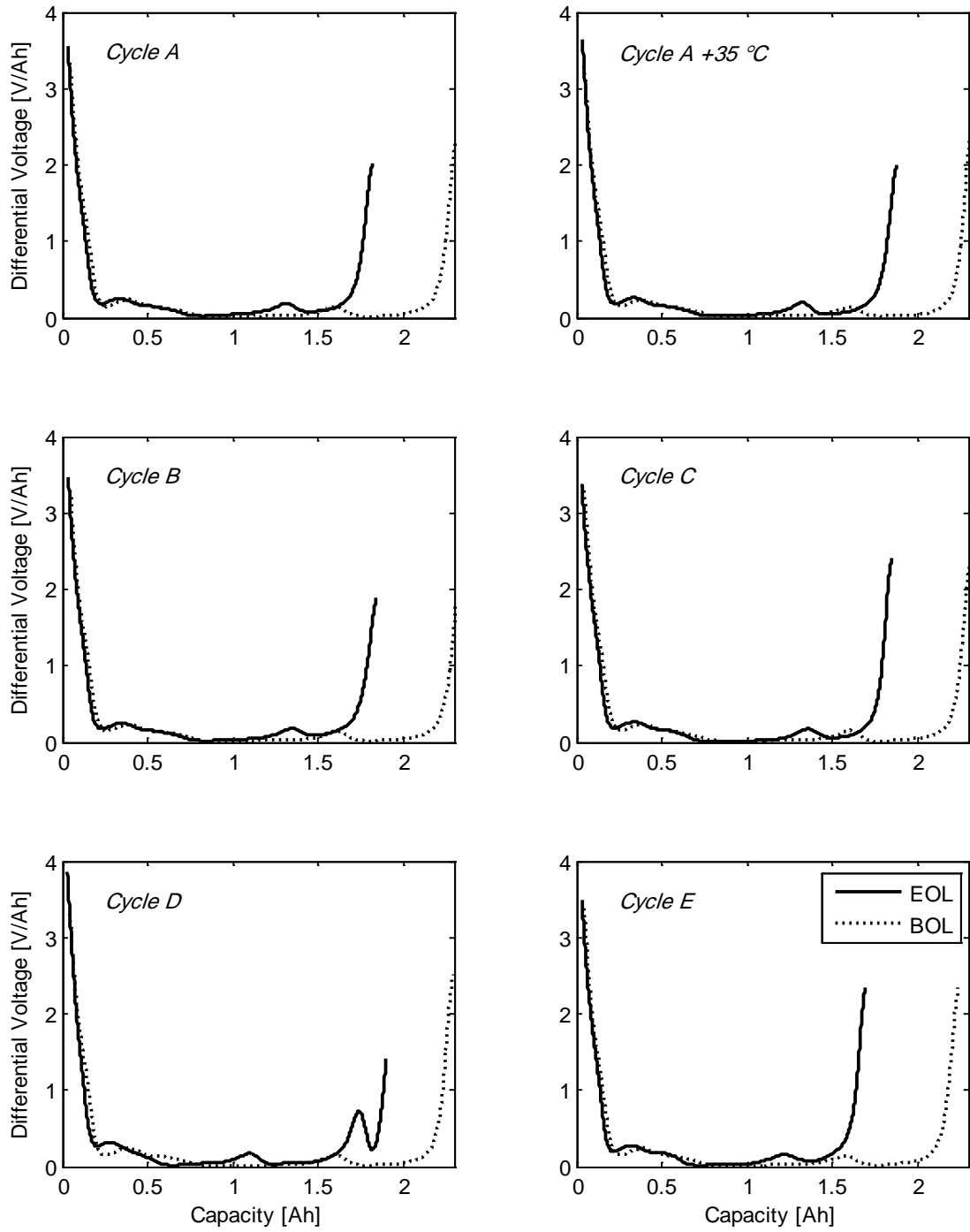
Figure 7.31   DVA for cells cycled according to *Cycle A, Cycle B, Cycle C* and *Cycle E.*

7.6 Estimation of Loss of Electrode Capacity and Cyclable Lithium

The method for estimating loss of active electrode material and loss of cyclable lithium described in section 7.2 and illustrated with the cell simulations in section 7.4 was applied to the cycle life tests with *Cycle A-E* using data from the C/4 voltage profiles. Since it is not easily conceivable to distinguish between loss of cyclable lithium and loss of active cathode material based on the presented cell model these ageing mechanisms will be displayed as one quantity in the graphical representation. Also, the estimation of the anode ageing is made using the same assumptions as in section 7.4 which in this case might not be fully valid since the detailed cell properties are unknown.

In this section the C/4 capacity is shown together with the estimated cell capacity loss due to anode loss and residual loss (cyclable lithium and cathode) for each of the tests using load *Cycle A-E*.

The result from the reference *Cycle A* in Figure 7.32 indicates that the anode ageing rate is lower than that of the cathode, and also lower than the rate of loss of cyclable lithium until the last phase of the ageing where both cell capacity and anode capacity rapidly decreases, indicating that the cell aging process undergoes several stages.

The EOL limit is set to the point when the cell capacity at 1 C-rate is 80% of the initial capacity as defined in Chapter 3. Another observation is that the two tested cells show a very similar ageing pattern.
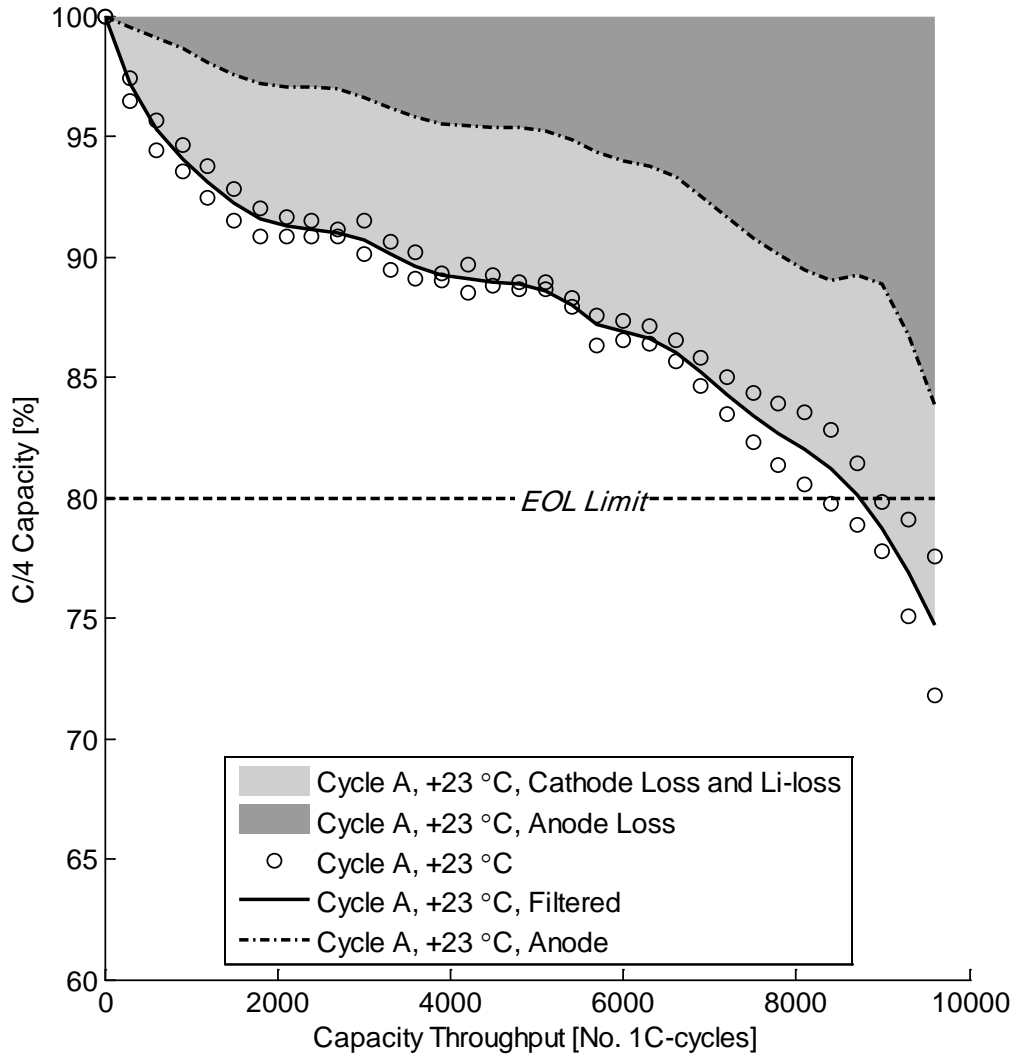
Figure 7.32   C/4 capacity and loss distribution for cells cycled with *Cycle A* at +23 °C.

For the cell cycled according to *Cycle A* in +35°C, presented in Figure 7.33, the overall characteristics is similar to that of Cycle A in +23°C but the fade rate is, surprisingly, lower.
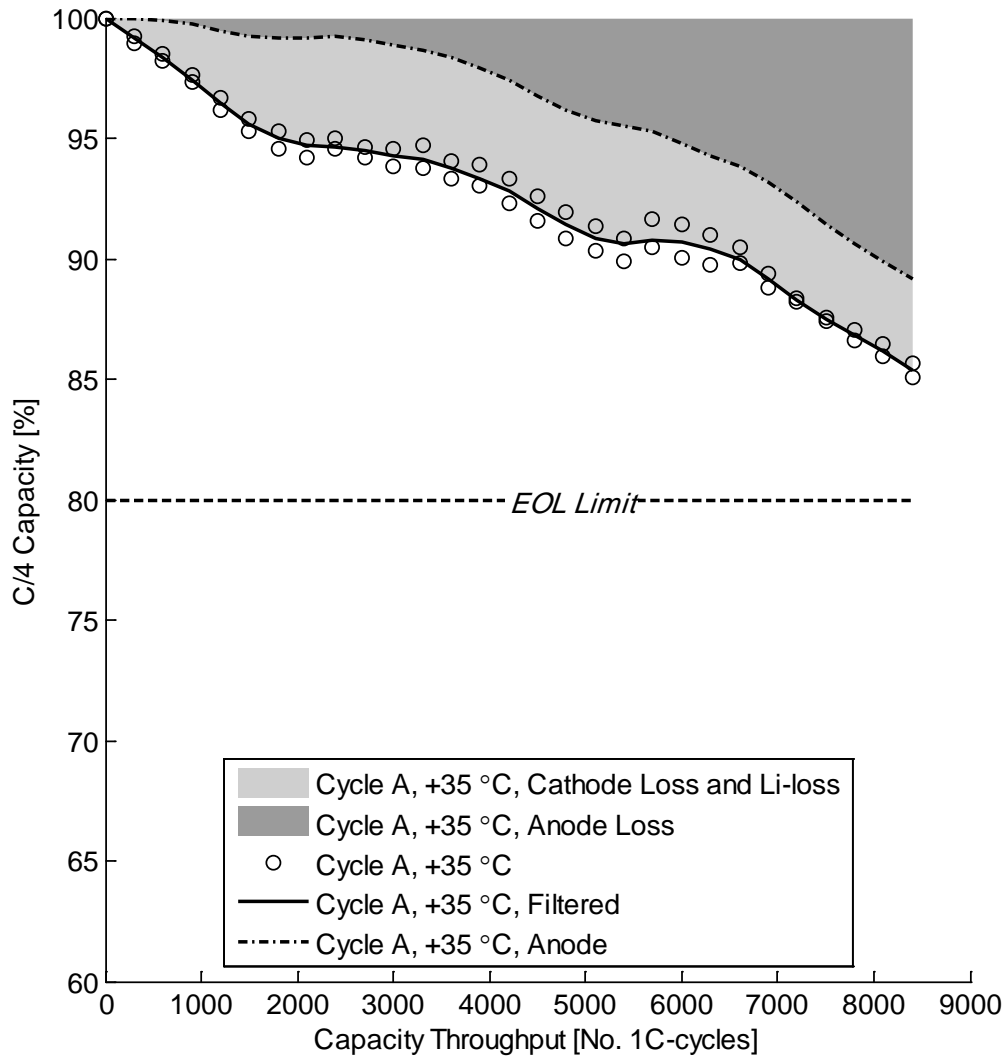
Figure 7.33   C/4 capacity and loss distribution for cells cycled with *Cycle A* at +35 °C.

However, the estimated anode fade rate is comparably lower for the first phase of ageing compared to that of *Cycle A* in +23°C. This can possibly indicate that initially a more stable SEI is formed in higher temperature.

In comparison with the reference *Cycle A*, the synthetic *Cycle B* (Figure 7.34) appears to accelerate anode ageing although the loss of lithium and cathode loss is lower.
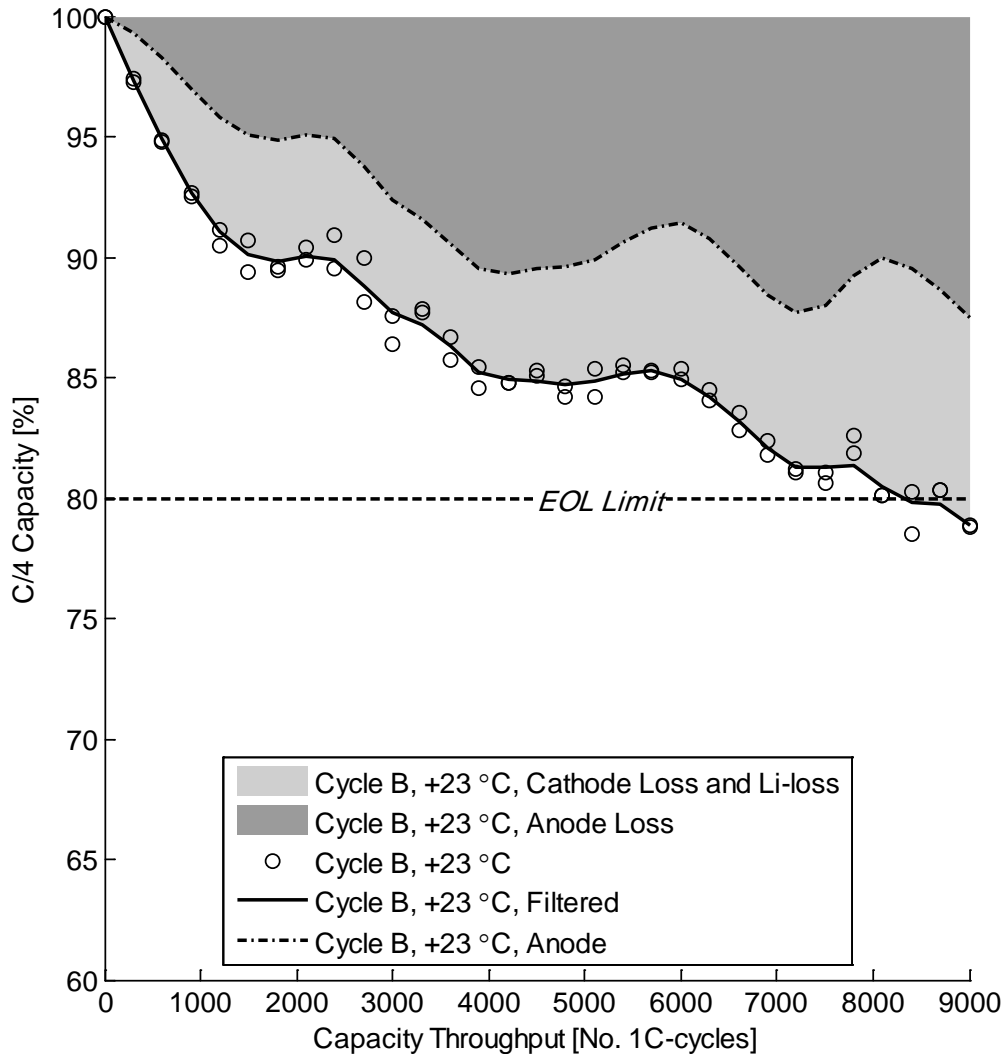
Figure 7.34   C/4 capacity and loss distribution for cells cycled with synthetic *Cycle B* at +23 °C.

Another observation is that the signature of the anode ageing is clearly visible in the overall capacity loss; whenever there is a local increase in capacity, the same increase can be observed in the anode capacity. The capacity is not monotonically decreasing, possibly indicating a complex correlation between different ageing mechanisms.

When the same analysis is applied to the constant current *Cycle C* (Figure 7.35 and Figure 7.36), a similar ageing pattern is perceived although the overall fade rate is significantly faster; the total cycle life expressed in capacity throughput is dramatically lower than for cells cycled with HEV cycles (*Cycle A, Cycle B* and *Cycle D*).
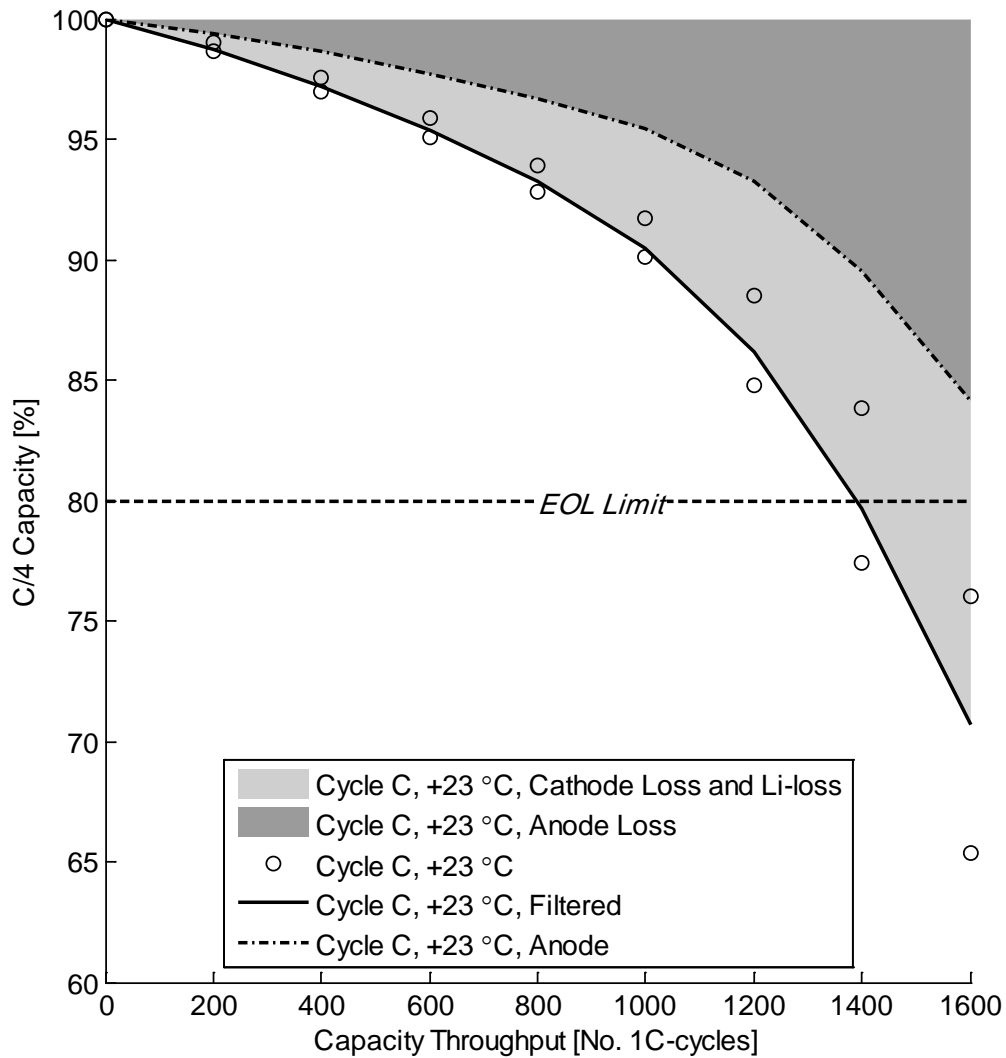
Figure 7.35   C/4 capacity and loss distribution for cells cycled with *Cycle C* at +23 °C.

In contrast to what might have been expected, the cell life is in this case slightly higher for the cells cycled at +35 °C (Figure 7.36) than those cycled at +23 °C (Figure 7.35).
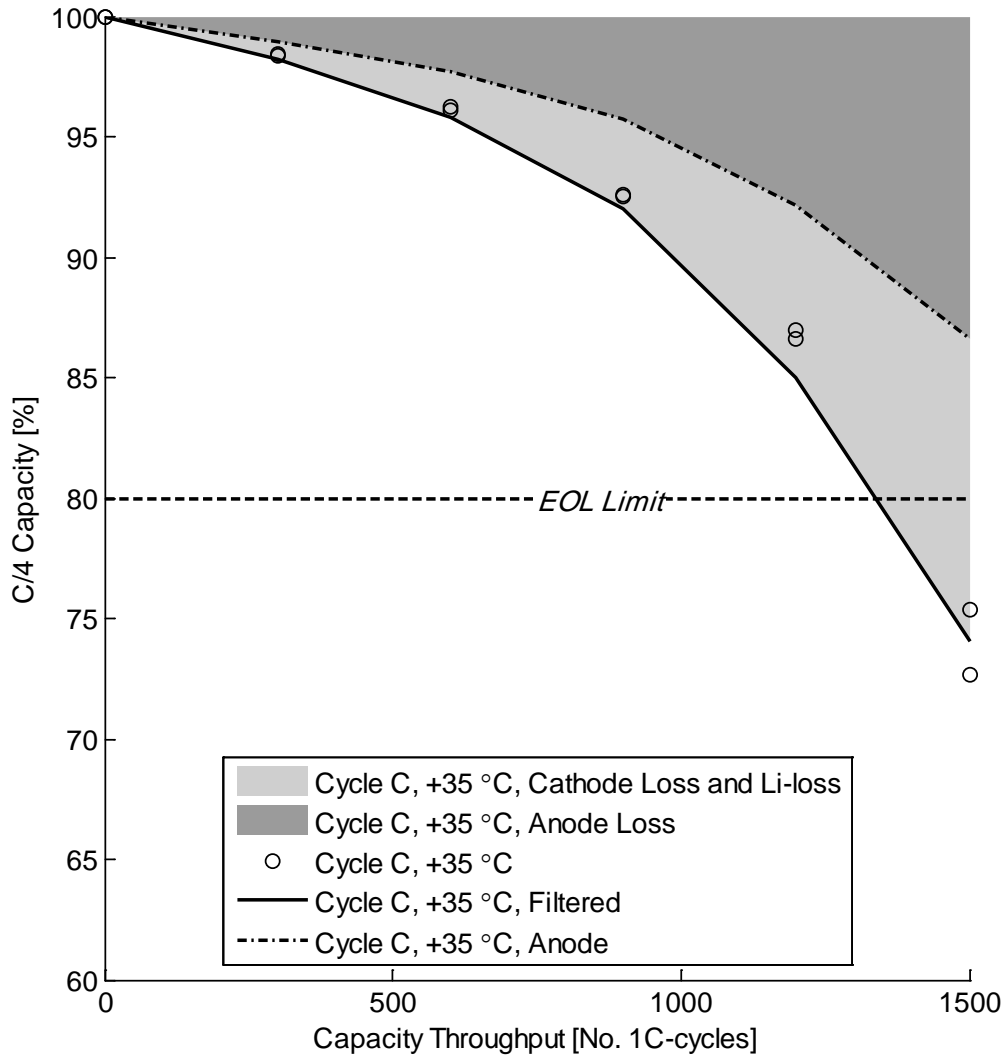
Figure 7.36   C/4 capacity and loss distribution for cells cycled with *Cycle C* at +35°C.

However, the average cell temperature does not differ significantly between these two test series since the losses are lower at +35°C and the convection is more effective in the climate chamber.

Constant current *Cycle D* shows an ageing trend similar to that of *Cycle A* and *Cycle B* when comparing the capacity fade (Figure 7.37).
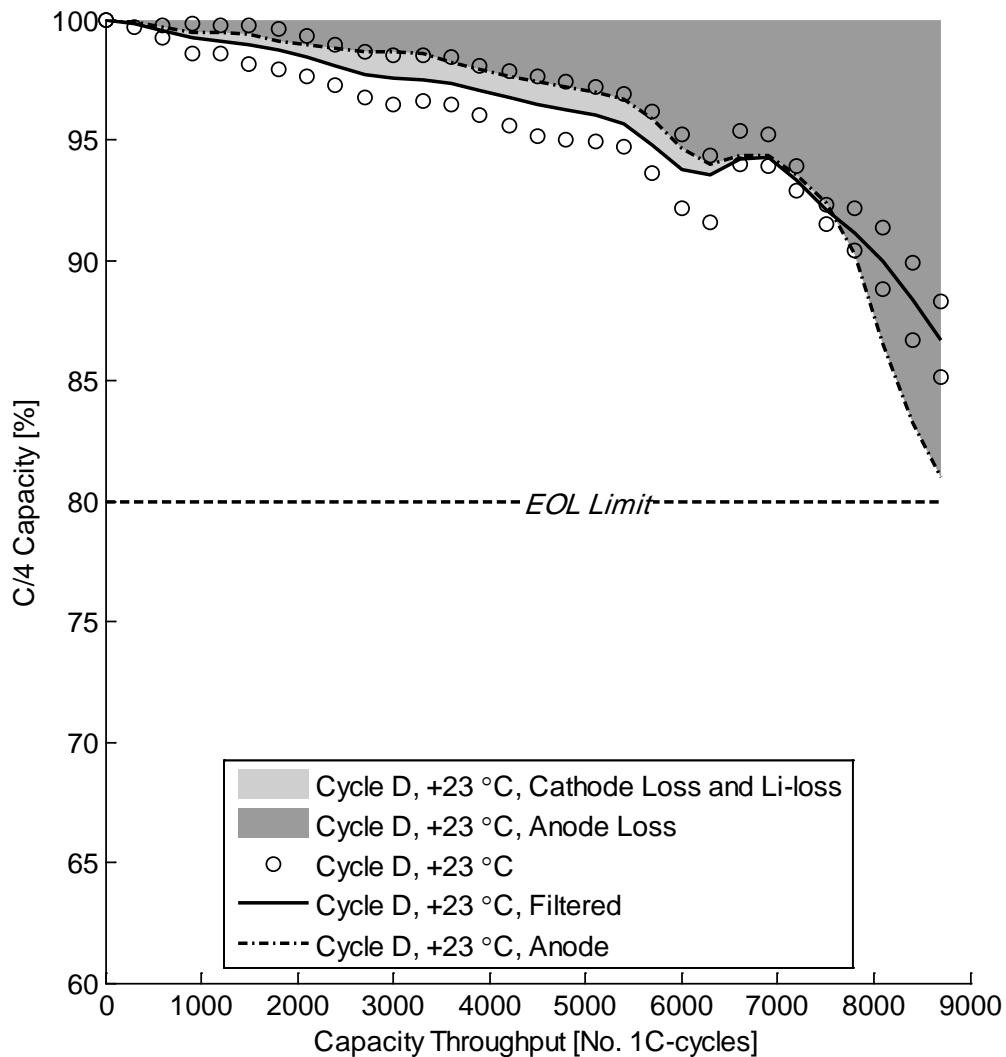
Figure 7.37   C/4 capacity and loss distribution for cells cycled with *Cycle D* at +23 °C.

However, the estimated loss of lithium and cathode ageing is almost negligible throughout the test. Towards the end of the test, the anode capacity estimated with the presented method decreases dramatically until it, according to the model, limits the overall cell capacity. This would by definition lead to Li-plating. Alternatively, it may indicate that the start condition assumptions of the cell fade model must be changed. Nevertheless, when comparing the estimated loss of anode material by *Cycle D* with the results from *Cycle A*, *Cycle B* and *Cycle C*, it can be concluded that the loss of lithium and cathode loss seems to be accelerated by either a wide SOC range or high peak current. Also, results from galvanostatic voltage profiles (section 7.1), ICA and DVA (section 7.5) all indicate a possible case of Li-plating. Despite that all these methods

point out possible Li-plating, it is believed that further analysis such as *post mortem* should be made to confirm the results.

In general, the analysis of the PHEV *Cycle E* test (Figure 7.38) shows a trend similar to that of the constant current tests at wide SOC range (*Cycle C*); a comparably rapid decrease of cell capacity.
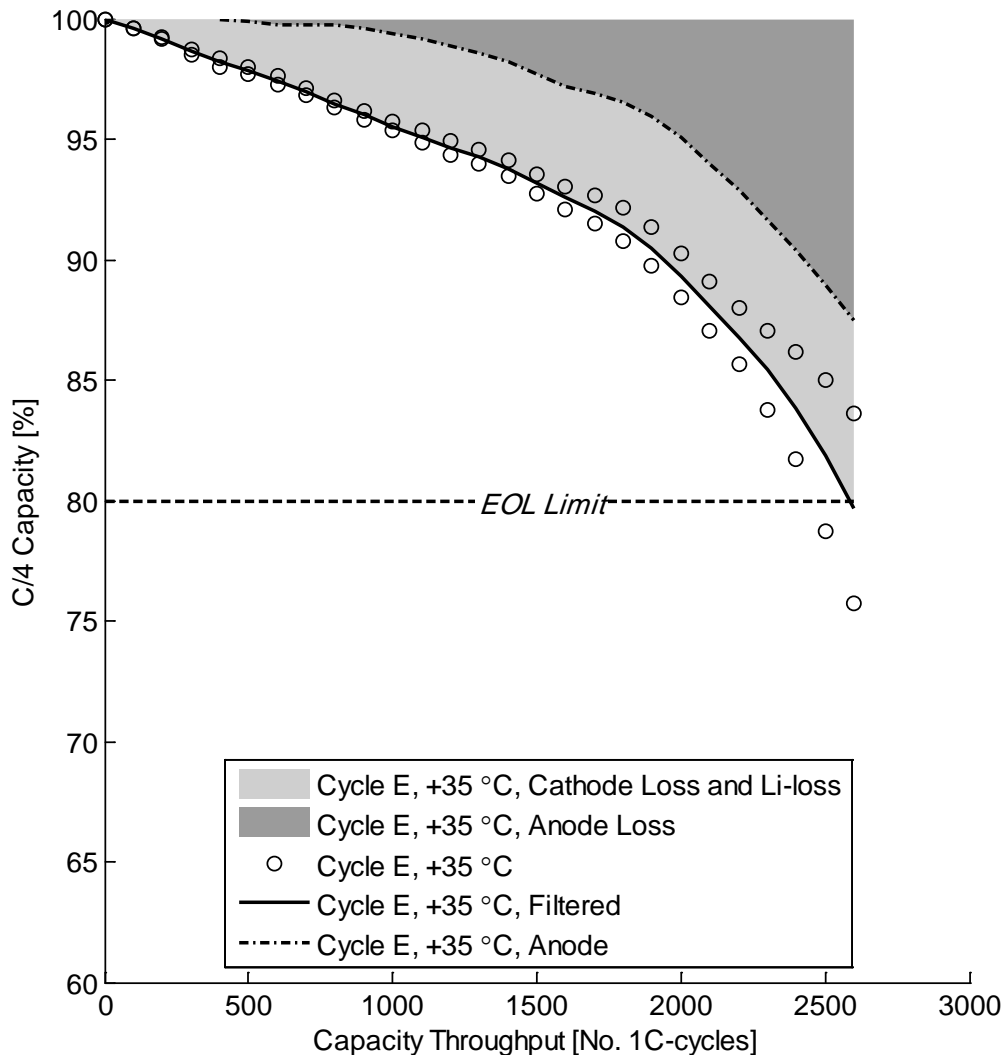
Figure 7.38   C/4 capacity and loss distribution for cells cycled with *Cycle E* at +35 °C.

In contrast to the *Cycle C*, the anode ageing is negligible for the first half of the test duration, possibly indicating that the higher current rate used in *Cycle C* accelerated anode ageing in a similar respect as observed for *Cycle A* and *Cycle B*. The loss of lithium and, and possibly, loss of cathode active material dominates the ageing until approximately 10% of the capacity has been lost, similar to what has been showed for LiFePO$_4$/graphite cells before [88].

7.7 Impedance Growth

In parallel with the RPTs carried out at regular basis throughout the cycle life test a limited EIS was performed every other RPT. Numerous ways of characterising the change in an EIS exist. In this section two of key parameters were extracted according to the description in section 3.2 and the equivalent circuit in Figure 3.7:

- Ohmic resistance R_{ohm} approximately equal to the real impedance at the intersection of the *Nyqvist*-curve with the real axis.
- Charge transfer resistance R_{CT} approximately equal to the real impedance at the local minima found at frequencies lower than that of the depressed semi-circle.

These fitted model parameters are used instead of direct measurement in order to filter out noise in measurements. Furthermore, since these values are extracted from small-signal impedance spectroscopy they are not necessarily as affected by changes in mass-transport properties as the charge and discharge impedance presented in Chapter 6.

Both the charge transfer resistance (Figure 7.40) and the ohmic resistance (Figure 7.39) estimated from the impedance spectroscopy measurements show a good correlation with the DC impedance measurements (Figure 6.4 and Figure 6.5). However, the trends in the curves are more consistent, indicating that EIS may provide higher accuracy and less noise than the DC impedance.

A noticeable difference between these two impedance measurements is that the ohmic impedance (Figure 7.39) is more strongly correlated to the change in estimated anode capacity than the charge transfer resistance (Figure 7.40). To some extent this is expected since the ohmic impedance is directly dependent on the active surface area whereas the charge transfer resistance is also linked to changes in the mass transport properties and the reaction kinetics. Furthermore, a loss of lithium in the electrolyte is also expected to decrease the conductivity and result in cell ohmic impedance increase.
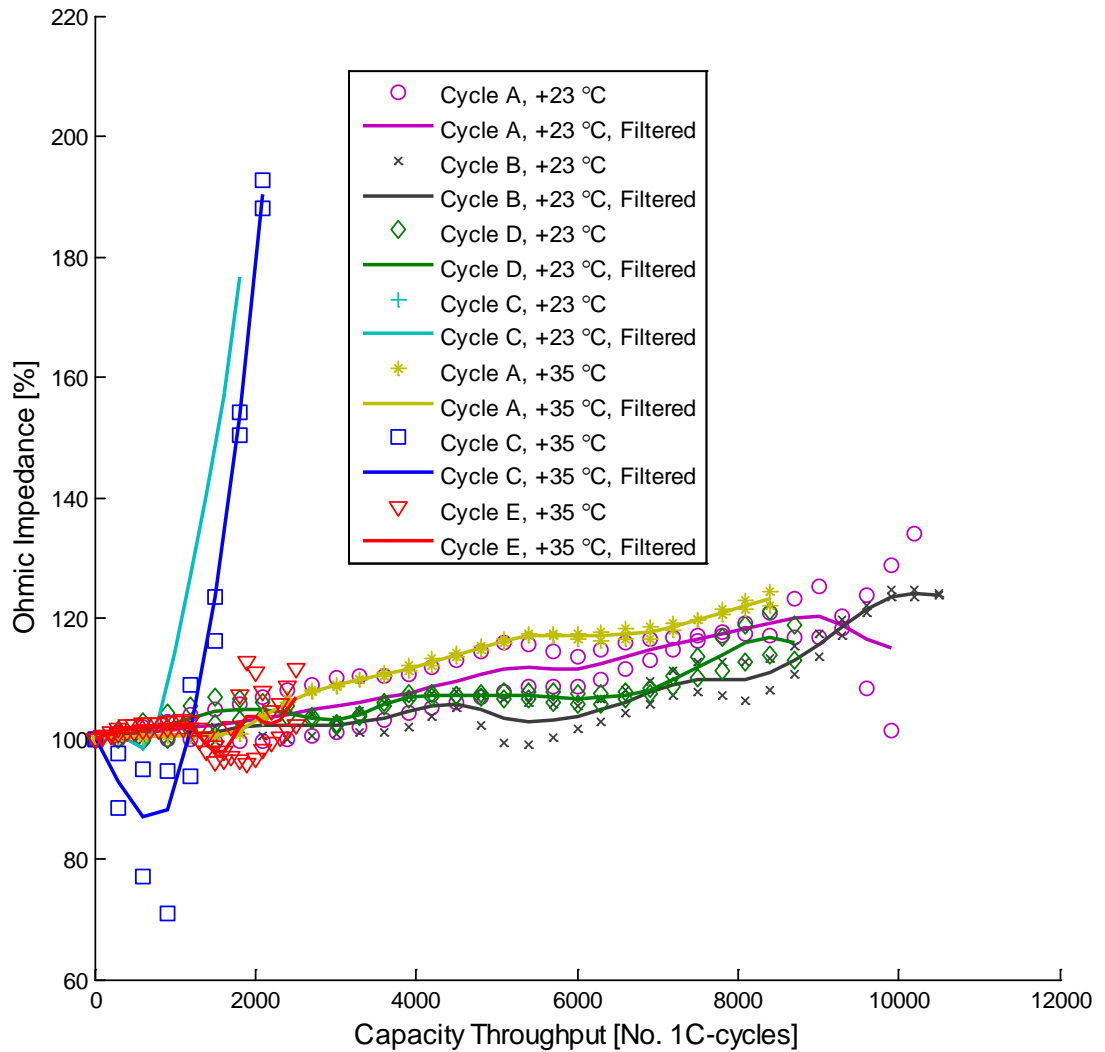
Figure 7.39   Ohmic impedance R_{ohm} *vs.* capacity throughput for cells cycled with *Cycle A-E.*

In addition, the ohmic impedance may serve as an indicator of imminent cell failure; the impedance rises quickly just before the cell capacity starts to decline rapidly.

Also, it is possible to observe a non-consistent change in the ohmic resistance evolution. In other words, although the impedance of the cell increases significantly overtime, the impedance is not monotonically increasing; in turn a possible indication that the cells undergo different ageing phases involving increase (SEI growth), decrease (SEI dissolution) and increase again (SEI formation). Towards the EOL all cells shows a rapid increase indicating a loss of active anode material, a rapid growth of SEI and decrease of conductivity in electrodes and electrolyte.
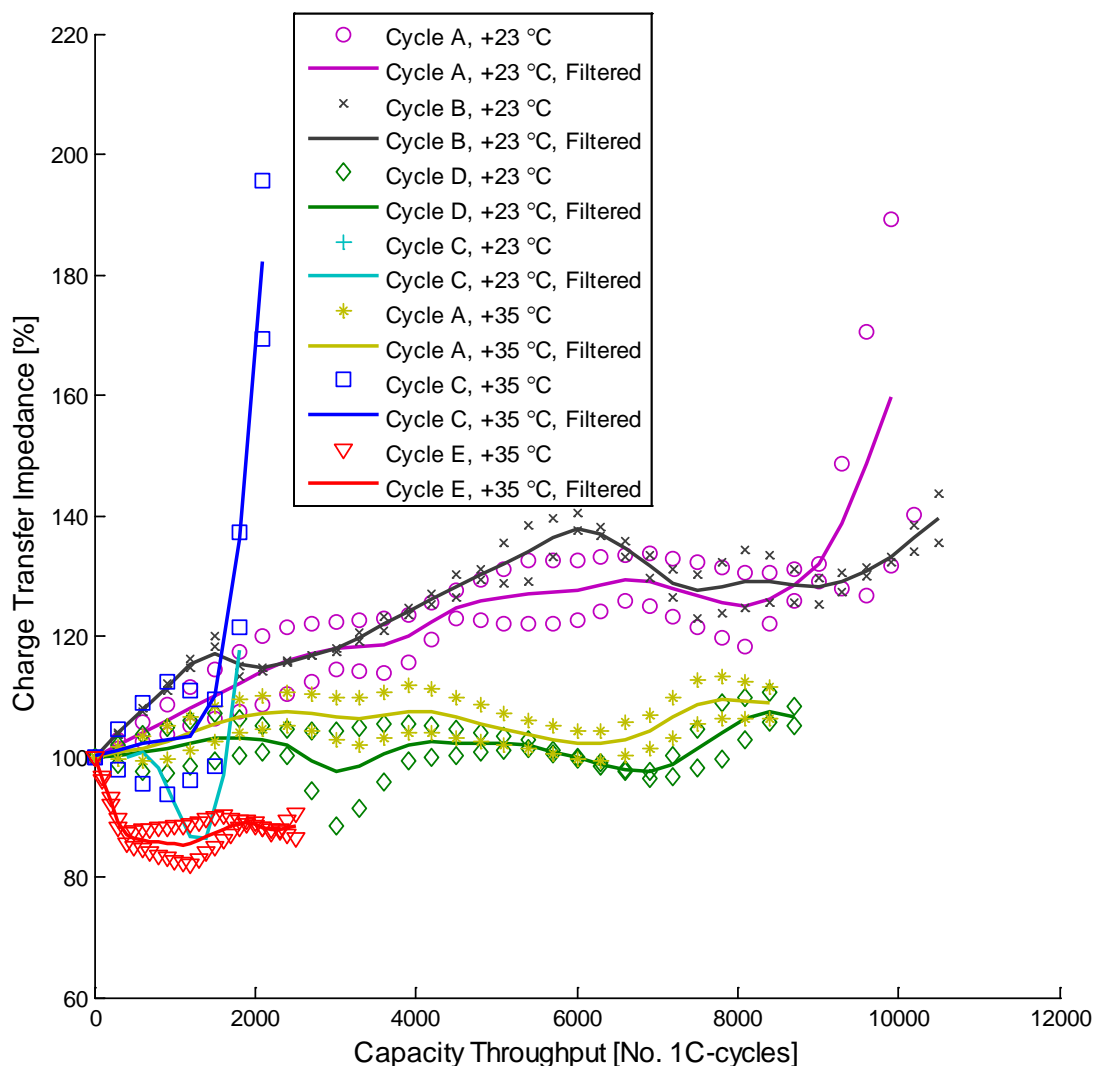
Figure 7.40   Charge transfer impedance R_{CT} *vs.* capacity throughput for cells cycled with *Cycle A-E*.

Furthermore, all cells cycled with a wide SOC range (*Cycle C* and *Cycle E*) show an initial decrease in charge transfer resistance before it increases towards EOL. This behaviour might be linked to rapid change in the thickness of the SEI. It may also be used as an early sign of a rapid ageing since the behaviour is only observed for cycles resulting in an overall rapid ageing pattern.

Further analysis of the impedance growth can be made using the impedance spectra. However, only impedance spectra measured at the same state of ageing can be compared. In Figure 7.41 the impedance spectrum at 50% SOC is shown at BOL and EOL (20% C/1 capacity loss) for cells cycled according to the *Cycle A-E*.
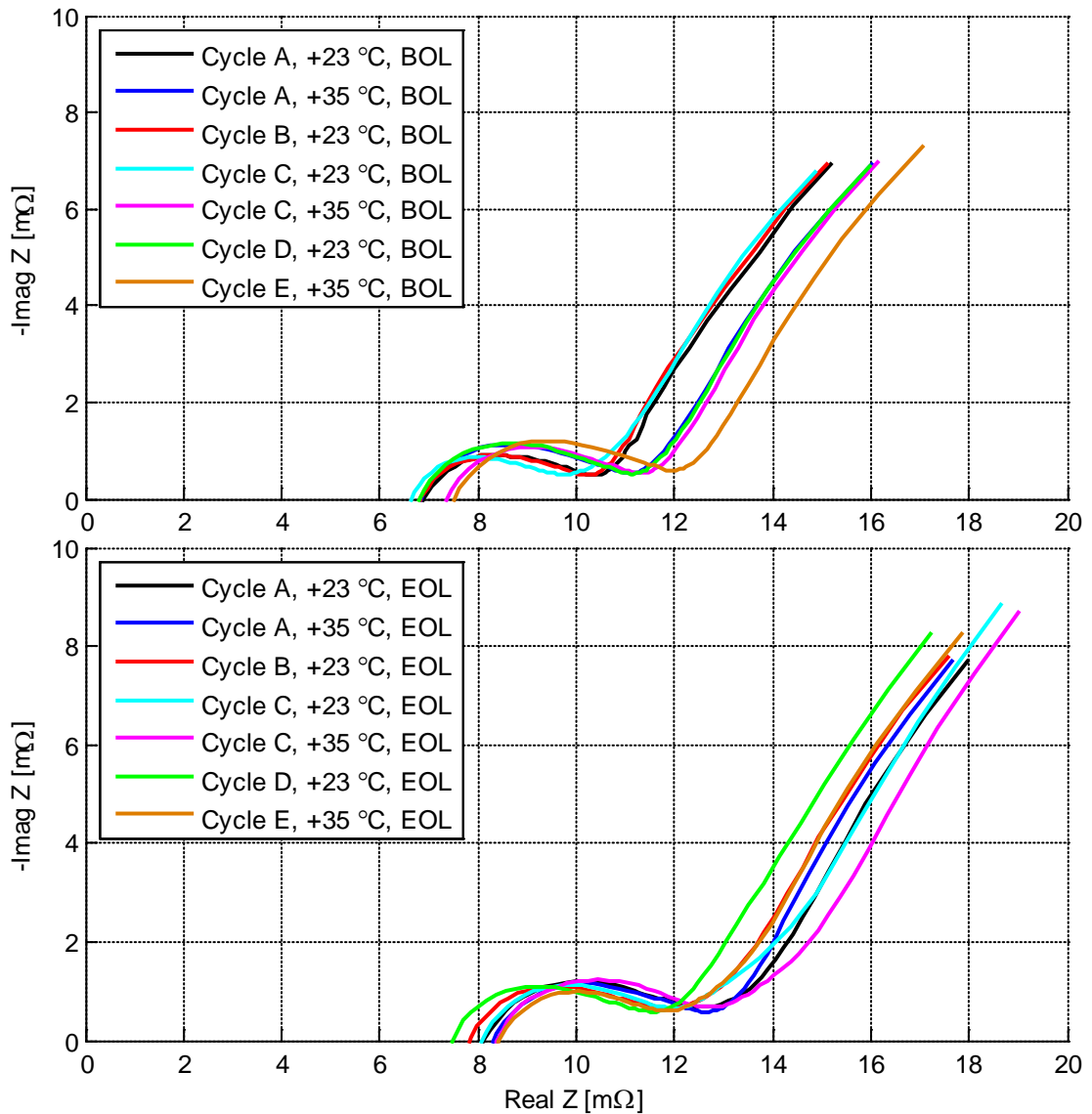
Figure 7.41   EIS at BOL and EOL for cells cycled with *Cycle A-E*.

There is a distribution in initial impedance spectra that most probably is due to calendar ageing since some of the tests were initiated up to one year after the first tests. Further details are given in section 6.5. However, the cells with the highest initial impedance (*Cycle D* and *Cycle E*) have the lowest impedance growth at EOL, indicating that the calendar ageing not necessarily should be treated as an offset to the cycle ageing.

Also, at approximately the same capacity loss (at EOL), all cells show the same impedance characteristics although the impedance growth rate differs. Notably, cells cycled according to *Cycle B* and *Cycle D* have a comparably low impedance increase.

Chapter 8   Concluding Remarks

The loss of cyclable lithium is found to be the main contribution to ageing during the first phase of cycling. Yet, the loss of active anode material accelerates close to EOL for all cycle life tests presented in this thesis. As expected, the longest lifetime is observed for cells cycled with low peak currents and a narrow SOC range and they also show the lowest late of lithium loss. For one of the tested load cycles a possible case of reversible Li-plating at EOL is observed.

Despite similarities in average current and SOC range, the three HEV cycles yield different ageing characteristics, indicating that a more detailed evaluation of load cycle properties is needed to enable a cycle life estimation model. A brief analysis of the load cycles indicates that voltage distribution and SOC distribution over time are the most important characteristics of a cycle.

The temperature is not found to be an important factor in the range between +30...+45 °C. On the contrary, cells cycled according to an HEV cycle at +35 °C ambient temperature had a slower fade rate than those cycled at +23 °C. This may indicate that the moderately higher temperature leading to a more narrow voltage distribution is a more important factor than the temperature induced increase of parasitic reactions within the cell.

The work described in this thesis focused on the effect on ageing that five different load cycles has on $LiFePO_4$//graphite cells and an assessment of different *ex situ* analysis methods. Three cycles were set-up to resemble HEV type operating conditions; wide current distribution, high peak currents and a narrow SOC range. In addition, two cycles were designed to highlight PHEV characteristics; narrow current distribution and wide SOC range.

A combination of capacity and power measurements, incremental capacity analysis, differential voltage analysis and impedance spectroscopy was used to quantify the ageing mechanisms. Also, experiments on half-cells were used to develop a simplified cell ageing model used to simulate loss of active electrode material and cyclable lithium.

The battery cells cycled according to the HEV cycles using a narrow SOC range showed a slow capacity and power fade for approximately 10 000 capacity throughputs before reaching the EOL criteria of 20% capacity fade. For a heavy-duty HEV this corresponds to approximately one year of operation assuming 16h service per day, 350 days per year. In comparison, the cells cycled according to the PHEV cycles with a wide SOC showed a rapid fade in capacity and power resulting in approximately 2 000 capacity throughputs before reaching EOL, corresponding to approximately 9 months of operation assuming 8 cycles per day.

For the PHEV cycles the charge rate appears to be a very important factor for the ageing; a reduction from 3.75 C-rate charge to 2 C-rate charge increased the cycle life with almost 100%.

The ageing processes of Li-ion batteries are complex and strongly dependent on operating conditions. In addition, it is difficult to quantify the different mechanisms without performing an extensive *post mortem* analysis of aged cells. In addition, a test matrix covering all possible combinations of operating conditions is extremely large and such test would require many years of testing to obtain relevant and reliable results.

Chapter 9   Future Work

The work presented in this thesis will continue and include further cycle life tests, cell modelling and development of algorithms for estimating the SOH as a function of operating conditions including the load cycle characteristics. Whereas the cycle life tests presented in this thesis was focused on HEV and PHEV load cycles, several specific load cycles will be developed to test the ageing factors of various load cycle properties such as SOC range, current range and temperature.

Although the ICA and the DVA methods showed promising results as indicators of ageing mechanisms, a *post mortem* analysis of aged cells will be needed to verify the results. In addition, cells with reference electrodes may be used to confirm the validity of these methods and possibly to quantify the loss of cyclable lithium and loss of active cathode material.

Further cooperation with UU, KTH and Scania CV AB may also enable a correlation between cycle life tests of large cells and small-scale research cells. This may in turn lead to a deeper understanding of the ageing mechanisms of Li-ion batteries used in heavy-duty HEVs and PHEVs. Furthermore, it can also facilitate the development of more reliable test methods for accelerated ageing of cells and more accurate *ex situ* characterisation methods.

The underlying questions for the future work are:
- Which are the most important ageing mechanisms for different operating conditions?
- How are the different ageing mechanisms correlated and cross-dependent?
- To what complexity should SOH models be developed to find a good compromise between accuracy and suitability for applied usage?

Chapter 10 References

[1]   L. Gaines, R. Cuenza, *"Costs of lithium-Ion Batteries for Vehicles"*, Report ANL/ESD-42 (2000), Argonne National Laboratory, US.

[2]   L. O. Valøen, M. I. Shoesmith, *"The effect of PHEV and HEV duty cycles on battery and battery pack performance"*, Plug-in Hybrid Electric Vehicle 2007 Conference.

[3]   A.G. Ritchie, *"Recent developments and likely advances in lithium rechargeable batteries"*, Journal of Power Sources 136 (2004) 285–289.

[4]   A.G. Ritchie, W. Howard, *"Recent developments and likely advances in lithium-ion batteries"*, Journal of Power Sources 162 (2006) 809–812.

[5]   W.F. Howard, R. Spotnitz, *"Theoretical evaluation of high-energy lithium metal phosphate cathode materials in Li-ion batteries"*, Journal of Power Sources 165 (2007) 887–891.

[6]   K. Amine, C.H. Chen, J. Liu, M. Hammond, A. Jansen, D. Dees, I. Bloom, D. Vissers, G. Henriksen*, "Factors responsible for impedance rise in high power lithium ion batteries"*, Journal of Power Sources 97-98 (2001) 684-687.

[7]   I. Bloom, B.W. Cole, J.J Sohn, S.A. Jones, E.G. Polzin, V.S. Battaglia, G.L. Henriksen, C. Motlach, R. Richardson, T. Unkelhaeuser, D. Ingersoll, H.L. Case, *"An accelerated calendar and cycle life study of Li-ion cells"*, Journal of Power Sources 101 (2001) 238-247.

[8]   M. Broussely, Ph. Biensan, F. Bonhomme, Ph. Blanchard, S. Herreyre, K. Nechev, R.J. Staniewicz, *"Main aging mechanisms in Li ion batteries"*, Journal of Power Sources 146 (2005) 90–96.

[9]   J. Vetter, P. Novák, M.R. Wagner, C. Veit, K-C. Möller, J.O. Besenhard, M. Winter, M. Wohlfahrt-Mehrens, C. Vogler, A. Hammouche, *"Ageing mechanisms in lithium-ion batteries"*, Journal of Power Sources 147 (2005) 269–281.

[10]   D.P. Abraham, E.M. Reynolds, E. Sammann, A.N. Jansen, D.W. Dees, *"Aging characteristics of high-power lithium-ion cells with $LiNi_{0.8}Co_{0.15}Al_{0.05}O_2$ and $Li_{4/3}Ti_{5/3}O_4$ electrodes"*, Electrochimica Acta 51 (2005) 502–510.

[11]   D.P. Abraham, S.D. Poppen, A.N. Jansen, J. Liu, D.W. Dees, *"Application of a lithium–tin reference electrode to determine electrode contributions to impedance rise in high-power lithium-ion cells"*, Electrochimica Acta 49 (2004) 4763–4775.

[12]   J. Li, E. Murphy, J. Winnick, P.A. Kohl, *"Studies on the cycle life of commercial lithium ion batteries during rapid charge–discharge cycling"*, Journal of Power Sources 102 (2001) 294–301 .

[13]   F. Savoye, P. Venet, M. Millet, J. Groot, *"Impact of periodic current pulses on Li-ion battery performance"*, IEEE (2011).

[14]   B. Markovsky, A. Rodkin, Y.S. Cohen, O. Palchik, E. Levi, D. Aurbach, H-J. Kim, M. Schmidt, *"The study of capacity fading processes of Li-ion batteries: major factors that play a role",* Journal of Power Sources 119–121 (2003) 504–510.

[15]   M. Dubarry, B.Y. Liaw, M-S. Chen, S-S. Chyan, K-C. Han, W-T. Sie, S-H. Wu, *"Identifying battery aging mechanisms in large format Liion cells"*, Journal of Power Sources 196 (2011) 3420-3425.

[16]   Y. Zhang, C-Y. Wang, X. Tang, *"Cycling degradation of an automotive LiFePO$_4$ lithium-ion battery",* Journal of Power Sources 196 (2011) 1513–1520.

[17]   K.A. Striebel, J. Shim, *"Cycling performance of low-cost lithium ion batteries with natural graphite and LiFePO$_4$",* Journal of Power Sources 119-121 (2003), 955-958.

[18]   M. Dubarry, V. Svoboda, R. Hwu, B.Y. Liaw, *"Capacity and power fading mechanism identification from a commercial cell evaluation"*, Journal of Power Sources 165 (2007) 566–572.

[19]   M. Dubarry, V. Svoboda, R. Hwu, B.Y. Liaw, *"Capacity loss in rechargeable lithium cells during cycle life testing: The importance of determining state-of-charge"*, Journal of Power Sources 174 (2007) 1121–1125.

[20]   S.C. Nagpure, B. Bhushan, S. Babu, G. Rizzoni, *"Scanning spreading resistance characterization of aged Li-ion batteries using atomic force microscopy"*, Scripta Materialia 60 (2009) 933–936.

[21]   J.R. Belt, C.D. Ho, T.J. Miller, M.A. Habib, T.Q. Duong, *"The effect of temperature on capacity and power in cycled lithium ion batteries"*, Journal of Power Sources 142 (2005) 354–360.

[22]   D.P. Abraham, J. Liu, C.H. Chen, Y.E. Hyung, M. Stoll, N. Elsen, S. MacLaren, R. Twesten, R. Haasch, E. Sammann, I. Petrov, K. Amine, G. Henriksen, *"Diagnosis of power fade mechanisms in high-power lithium-ion cells"*, Journal of Power Sources 119–121 (2003) 511–516.

[23]   M. Kerlau, M. Marcinek, V. Srinivasan, R.M. Kostecki, *Reprint of "Studies of local degradation phenomena in composite cathodes for lithium-ion batteries",* Electrochimica Acta 53 (2007) 1385–1392.

[24]   P. Liu, J. Wang, J. Hicks-Garner, E. Sherman, S. Soukiazian, M. Verbrugge, H. Tataria, J. Musser, P. Finamore, *"Ageing Mechanisms of LiFePO$_4$ Batteries Deduced by Electrochemical and Structural Analyses"*, Journal of The Electrochemical Society 157 (4) (2010), A499-A507.

[25]   K. A. Striebel, J. Shim, E.J. Cairns, R. Kostecki, Y.J. Lee, J. Reimer, T.J. Richardson, P.N. Ross, X. Song, G.V. Zhuang, *"Diagnostic Analysis of Electrodes from High-Power lithium-Ion Cells Cycled under Different Conditions"*, Journal of The Electrochemical Society 151 (6) (2004), A857-A866.

[26]   V. A. Sethuraman, L.J. Hardwick, V. Srinivasan, R. Kostecki, "*Surface structural disordering in graphite upon lithium intercalation/deintercalation*", Journal of Power Sources 195 (2010) 3655–3660.

[27]   G. Sarre, Ph. Blanchard, M. Broussely, *"Aging of lithium-ion batteries"*, Journal of Power Sources 127 (2004) 65–71.

[28]   M. Shikano, H. Kobayashi, S. Koike, H. Sakaebe, E. Ikenaga, K. Kobayashi, K. Tatsumi, "*Investigation of positive electrodes after cycle testing of high-power Li-ion battery cells II. An approach to the power fading mechanism using hard X-ray photoemission spectroscopy*", Journal of Power Sources 174 (2007) 795–799.

[29]   J.R. Belt, C.D. Ho, C.G. Motloch, T.J. Miller, T. Q. Duong, *"A capacity and power fade study of Li-ion cells during life cycle testing",* Journal of Power Sources 123 (2003) 241–246.

[30]   A. du Pasquier, A. Blyr, A. Cressent, C. Lenain, G. Amatucci, *"An update on the high temperature ageing mechanism in LiMn$_2$O$_4$-based Li-ion cells"*, Journal of Power Sources 81–82 (1999) 54–59.

[31]   K. Zaghib, M. Dontigny, P. Charest, J.F. Labrecque, A. Guerfi, M. Kopec, A. Mauger, F. Gendron, C.M. Julien, *"Aging of LiFePO$_4$ upon exposure to H$_2$O"*, Journal of Power Sources 185 (2008) 698–710.

[32]   M. Broussely, S. Herreyre, P. Biensan, P. Kasztejna, K. Nechev, R.J. Staniewicz, *"Aging mechanism in Li ion cells and calendar life predictions"*, Journal of Power Sources 97-98 (2001) 13-21.

[33]   X. Zhang, B. Winget, M. Doeff, J.W. Evans, T.M. Devine, *"Corrosion of Aluminum Collectos in lithium-Ion Batteries with Electrolytes Containing LiPF₆"*, Journal of The Electrochemical Society 152(11) (2005) B448-B454.

[34]   K. Amine, J. Liu, I. Belharouak, *"High-temperature storage and cycling of C-LiFePO₄/graphite Li-ion cells"*, Electrochemistry Communications 7 (2005) 669–673 .

[35]   S.H. Mohammadian, D. Aït-Kadi, F. Routhier, *"Quantitative accelerated degradation testing: Practical approaches"*, Reliability Engineering and System Safety (2009), doi:10.1016/j.ress.2009.09.009.

[36]   E.V. Thomas, I. Bloom, J.P. Christophersen, V.S. Battaglia, *"Statistical methodology for predicting the life of lithium-ion cells via accelerated degradation testing"*, Journal of Power Sources 184 (2008) 312–317.

[37]   R.G. Jungst, G. Nagasubramanian, H.L. Case, B.Y. Liaw, A. Urbina, T.L. Paez, D.H. Doughty, *"Accelerated calendar and pulse life analysis of lithium-ion cells"*, Journal of Power Sources 119–121 (2003) 870–873.

[38]   E.V. Thomas, H.L. Case, D.H. Doughty, R.G. Jungst, G. Nagasubramanian, E.P. Roth, *"Accelerated power degradation of Li-ion cells"*, Journal of Power Sources 124 (2003) 254–260.

[39]   K. Takei, K. Kumai, Y. Kobayashi, H. Miyashiro, N. Terada, T. Iwahori, T. Tanaka, *"Cycle life estimation of lithium secondary battery by extrapolation method and accelerated aging test"*, Journal of Power Sources 97-98 (2001) 697-701.

[40]   D. Aurbach, *"A review on new solutions, new measurements procedures and new materials for rechargeable Li batteries"*, Journal of Power Sources 146 (2005) 71–78.

[41]   J. Shim, R. Kostecki, T. Richardson, X. Song, K.A. Striebel, *"Electrochemical analysis for cycle performance and capacity fading of a lithium-ion battery cycled at elevated temperature"*, Journal of Power Sources 112 (2002) 222–230.

[42]   R.P. Ramasamy, R.E. White, B.N. Popov, *"Calendar life performance of pouch lithium-ion cells"*, Journal of Power Sources 141 (2005) 298–306.

[43]   D.P. Abraham, J.L. Knuth, D.W. Dees, I. Bloom, J.P. Christophersen, *"Performance degradation of high-power lithium-ion cells—Electrochemistry of harvested electrodes"*, Journal of Power Sources 170 (2007) 465–475.

[44]   D.P. Abraham et.al, *"Diagnostic Examination of Generation 2 lithium-Ion Cells and Assessment of Performance Degradation Mechanisms"*, Report ANL/-05-21 (2005), Argonne National Laboratory, US.

[45]   K. L. Gering, S.V. Sazhin, D. K. Jamison, C. J. Michelbacher, B. Y. Liaw, M. Dubarry, M. Cugnet, *"Investigation of path dependence in commercial lithium-ion cells chosen for plug-in hybrid vehicle duty cycle protocol"*, Journal of Power Sources 196 (2011) 3395-3403.

[46]   EUCAR Traction Battery Working Group, *"Specification of Test Procedures for High Voltage HEV Traction Batteries"* (2005).

[47]   FreedomCar, *"FreedomCAR Battery Test Manual For Power-Assist Hybrid Electric Vehicles"*, DOE/ID-11069 (2003).

[48]   IEC, *"Secondary batteries for the propulsion of electric road vehicles, part 2-3"*, IEC 61982-2, IEC 61982-3 (2002).

[49]   R.B. Wright, J.P. Christophersen, C.G. Motloch, J.R. Belt, C.D. Ho, V.S. Battaglia, J.A. Barnes, T.Q. Duong, R.A. Sutula, *"Power fade and capacity fade resulting from cycle-life testing of Advanced Technology Development Program lithium-ion batteries"*, Journal of Power Sources 119–121 (2003) 865–869.

[50]   A.J. Salkind, C. Fennie, P. Singh, T. Atwater, D.E. Reisner, *"Determination of state-of-charge and state-of-health of batteries by fuzzy logic methodology"*, Journal of Power Sources 80 (1999) 293–300.

[51]   P. Singh, R. Vinjamuri, X. Wang, D. Reisner, *"Fuzzy logic modeling of EIS measurements on lithium-ion batteries"*, Electrochimica Acta 51 (2006) 1673–1679.

[52]   P. Singh, R. Vinjamuri, X. Wang, D. Reisner, *"Design and implementation of a fuzzy logic-based state-of-charge meter for Li-ion batteries used in portable defibrillators"*, Journal of Power Sources 162 (2006) 829–836.

[53]   R. Spotnitz, *"Simulation of capacity fade in lithium ion batteries"*, Journal of Power Sources 113 (2003) 72-80.

[54]   P. Ramadass, B. Haran, R.White, B.N. Popov, *"Mathematical modeling of the capacity fade of Li-ion cells"*, Journal of Power Sources 123 (2003) 230–240.

[55]   U. Tröltzsch, O. Kanoun, H-R. Tränkler, *"Characterizing aging effects of lithium ion batteries by impedance spectroscopy"*, Electrochimica Acta 51 (2006) 1664–1672.

[56]   B.Y. Liaw, R.G. Jungst, G. Nagasubramanian, H.L. Case, D.H. Doughty, *"Modeling capacity fade in lithium-ion cells"*, Journal of Power Sources 140 (2005) 157–161.

[57]   V. Pop, H.J. Bergveld, P.H.L. Notten, J.H.G. Op het Veld, P.P.L. Regtien, *"Accuracy analysis of the State-of-Charge and remaining run-time determination for lithium-ion batteries"*, Measurement 42 (2009) 1131–1138.

[58]   A.T. Stamps, C.E. Holland, R.E. White, E.P. Gatzke, *"Analysis of capacity fade in a lithium ion battery"*, Journal of Power Sources 150 (2005) 229–239.

[59]   M. Safari, M. Morcrette, A. Teyssot, C. Delacourt, *"Multimodal Physics-Based Aging Model for Life Prediction of Li-Ion Batteries"*, Journal of The Electrochemical Society 156 (3) (2009) A145-A153.

[60]   J-W. Lee, Y.K. Anguchamy, B.N. Popov, "*Simulation of charge–discharge cycling of lithium-ion batteries under low-earth-orbit conditions"*, Journal of Power Sources 162 (2006) 1395–1400.

[61]   G. Ning, R.E. White, B.N. Popov,*"A generalized cycle life model of rechargeable Li-ion batteries"*, Electrochimica Acta 51 (2006) 2012–2022.

[62]   G. Ning, B.N. Popov, "*Cycle Life Modeling of lithium-Ion Batteries",* Journal of the Electrochemical Society 151 (10) (2004) A1584-A1591.

[63]   K.A. Smith, C. D. Rahn, C-Y. Wang, *"Control oriented 1D electrochemical model of lithium ion battery"*, Energy Conversion and Management 48 (2007) 2565–2578.

[64]   F. La Mantia, J. Vetter, P. Novák, "Impedance spectroscopy on porous materials: A general model and application to graphite electrodes of lithium-ion batteries", Electrochimica Acta 53 (2008) 4109–4121.

[65]   R.P. Ramasamy, J-W. Lee, B.N. Popov, "*Simulation of capacity loss in carbon electrode for lithium-ion cells during storage"*, Journal of Power Sources 166 (2007) 266–272.

[66]   J. Groot, *"Battery Benchmarking and Cyclelife Test Methods"*, conference: Transport Research Arena (TRA) Europe 2010, Brussels.

[67]   M. Montaru, S. Pelissier, *"Frequency and Temporal Identification of a Li-ion Polymer Battery Model Using Fractional Impedance"*, Advances in Hybrid Powertrains (2008), proceedings .

[68]   Y. Qi, H. Guo, L.G. Hector, Jr., A. Timmons, *"Threefold Increase in the Young's Modulus of Graphite Negative Electrode during lithium Intercalation*", Journal of The Electrochemical Society 157 (5) (2010), A558-A566.

[69]   J. Groot, *"Statistic Method for Extraction of Synthetic Load Cycles for Cycle life Tests of HEV Li-ion Batteries"*, conference: International Battery, Hybrid and Fuel Cell Electric Vehicle Symposium (EVS-24), Stavanger, Norway, 2009.

[70]   W.-K. Ching, M.K. Ng, *"Markov Chains: Models, Algorithms and Applications"*, Springer US, ISBN 978-0-387-29337-0, 2006.

[71]   A. Schell, H. Peng, D. Tran, E. Stamos, C. Lin, M. Joong Kim, *"Modelling and control strategy development for fuel cell electric vehicles",* Annual Reviews in Control 29 (2005) 159–168.

[72]   S.J. Moura, D.S. Callaway, H.K. Fathy, J.L. Stein, *"Impact of Battery Sizing on Stochastic Optimal Power Management in Plug-in Hybrid Electric Vehicles",* Proceedings of the 2008 IEEE International Conference on Vehicular (2008).

[73]   G. Zhang, R. Manduchi, *"Prediction of the Lifetime of a Battery-Operated Video Node Using Offline and Online Measurements",* International Workshop on Advanced Methods for Uncertainty Estimation in Measurement (2007).

[74]   D. Nydahl, M. Rydstedt, *"Generation of stochastic drive cycles"*, Chalmers University of Technology, Report No. EX028/2009 (2009).

[75]   P. Diaconis, *"The Markov Chain Monte Carlo Revolution"*, Bulletin of the American Mathematical Society 46 (2009), 179–205.

[76]   C. Chiasserini, Ramesh R. Rao, *"A Model for Battery Pulsed Discharge with Recovery Effect"*, Proceedings of IEEE WCNC 1999, vol. 2, pp. 636-639.

[77]   P. Rutquist, *"On Infinite-Horizon State-Constrained Optimal Control"*, Technical Report No.R020/2005, Chalmers University of Technology, ISSN 1403-266X.

[78]   *"Series 4000 - Industry Standard Automated Cell and Battery Test System"*, http://www.maccor.com/series4000.php, accessed 2011-12-28.

[79]   *"Reference 3000 Potentiostat » Gamry Instruments"*, http://www.gamry.com/products/potentiostats/reference-3000, accessed 2011-12-28.

[80]   *"Compact 19" Rack Mountable Temperature Chamber"*, http://www.maccor.com/temperaturechamber.php, accessed 2011-12-28.

[81]   M. Dubarry, V. Svoboda, R. Hwu, B.Y. Liaw, *"Incremental Capacity Analysis and Close-to-Equilibrium OCV Measurements to Quantify Capacity Fade in Commercial Rechargeable lithium Batteries"*, Electrochemical and Solid-State Letters 9 (10) (2006) A454-A457.

[82]   I. Bloom, A.N. Jansen, D.P. Abraham, J. Knuth, S.A. Jones, V.S. Battaglia, G.L. Henriksen, *"Differential voltage analyses of high-power, lithium-ion cells 1. Technique and application"*, Journal of Power Sources 139 (2005) 295–303.

[83]   I. Bloom, J. Christophersen, K. Gering, *"Differential voltage analyses of high-power lithium-ion cells 2. Applications"*, Journal of Power Sources 139 (2005) 304–313.

[84]   I. Bloom, J.P. Christophersen, D.P. Abraham, K.L. Gering, "*Differential voltage analyses of high-power lithium-ion cells 3. Another anode phenomenon*", Journal of Power Sources 157 (2006) 537–542.

[85]   I. Bloom, L.K. Walker, J.K. Basco, D.P. Abraham, J.P. Christophersen, C. D. Ho,"*Differential voltage analyses of high-power lithium-ion cells. 4. Cells containing NMC*", Journal of Power Sources 195 (2010) 877–882.

[86]   J.R. Dahn, "*Phase diagram of Li_xC_6*", Physical Review B44(1991), 9170-9177.

[87]   R. Yazami, Y. Reynier, "*Thermodynamics and crystal structure anomalies in lithium-intercalated graphite*", Journal of Power Sources 153 (2006) 312–318.

[88]   M. Dubarry, B.Y. Liaw, *"Identify capacity fading mechanism in a commercial $LiFePO_4$ cell"*, Journal of Power Sources 194 (2009) 541–549.